Summer 2019

Development of a Computational Elbow Joint Model to Analyze the Effects of Synovial Fluid on Articular Cartilage during Joint Motion

Abhishek Yellapragada
San Jose State University

DEVELOPMENT OF A COMPUTATIONAL ELBOW JOINT MODEL TO ANALYZE THE EFFECTS OF SYNOVIAL FLUID ON ARTICULAR CARTILAGE DURING JOINT MOTION

A Thesis

Presented to

The Faculty of the Department of Mechanical Engineering

San José State University

In Partial Fulfillment

of the Requirements for the Degree

Master of Science

by

Abhishek Yellapragada

August 2019

The Designated Thesis Committee Approves the Thesis Titled

DEVELOPMENT OF A COMPUTATIONAL ELBOW JOINT MODEL TO ANALYZE THE EFFECTS OF SYNOVIAL FLUID ON ARTICULAR CARTILAGE DURING JOINT MOTION

by

Abhishek Yellapragada

APPROVED FOR THE DEPARTMENT OF MECHANICAL ENGINEERING

SAN JOSÉ STATE UNIVERSITY

August 2019

Winncy Y. Du, Ph.D., P.E.	Department of Mechanical Engineering
Raymond K. Yee, Ph.D., P.E.	Department of Mechanical Engineering
Meghedi Babakhanian, Ph.D.	Department of Mechanical Engineering

ABSTRACT

DEVELOPMENT OF A COMPUTATIONAL ELBOW JOINT MODEL TO ANALYZE THE EFFECTS OF SYNOVIAL FLUID ON ARTICULAR CARTILAGE DURING JOINT MOTION

by Abhishek Yellapragada

While significant advances have been made in the development of computational elbow joint models, fluid-structure interaction (FSI) in the elbow joint has not yet been explored. The objective of this study is to develop a computational elbow joint model to simulate the effects of synovial fluid on articular cartilage during flexion, extension, pronation, and supination. The model was developed with anatomically accurate 3D bone geometries; articular cartilage geometries that were derived from the 3D bone geometries; ligaments defined as linear springs; muscles embedded as joint non-linear stiffness; and a fluid domain that encompassed the joint articulations with a homogenous, incompressible, Newtonian synovial fluid. Two FSI simulations with varying joint velocities were conducted for elbow flexion, extension, pronation, and supination each. Peak von Mises stress of 0.0073 MPa on proximal ulna articular cartilage and peak von Mises stress of 0.0085 MPa on proximal radius articular cartilage were recorded during flexion-extension and pronation-supination, respectively. Synovial fluid flow was found to be predominantly laminar for the slower joint velocity and turbulent for the faster joint velocity for all elbow joint motions. This model not only establishes a validated approach to developing FSI simulations in the elbow joint, but also presents information on crucial *in vivo* parameters such as articular cartilage stresses and synovial fluid flow patterns during joint motion.

ACKNOWLEDGMENTS

This work would not have been possible without the support of certain key people. I thank my thesis committee chair, Dr. Winncy Du, for her expert guidance starting from the day I approached her with my thesis proposal. I thank my thesis committee members, Dr. Raymond Yee and Dr. Meg Babakhanian for their timely advice on the engineering problems of this research effort. Dr. Raghu Agarwal, ME Department Graduate Coordinator, and Lydie Jones, ME Department Administrative Coordinator, were ever-present to resolve the administrative issues that arose during this study. Also, I would like to thank Heidi Eisips, Resource Coordinator, SJSU Writing Center, for her professional help in reviewing my thesis.

Given that my entire research work is based on computer simulations, I cannot adequately emphasize the impact of the support extended by Lee Andersen, Director at Engineering Computer Systems (ECS), Davidson College of Engineering, and Scott Pham, Systems Analyst, ECS, Davidson College of Engineering. In the same stead, Bob Gladys, University Program Account Manager, ANSYS was instrumental in providing me access to ANSYS High Performance Computing, thereby giving my FSI simulations the much-needed speed boost.

Without the timely support of these people on numerous occasions, progress of my research work would have been greatly impacted.

Lastly, I'll be remiss not to mention the unwavering support and encouragement provided by my parents and sister not just during this thesis study but throughout my life. Everything I am is because of them.

TABLE OF CONTENTS

LIST OF TABLES

LIST OF FIGURES

LIST OF ABBREVIATIONS

AL – Annular Ligament
ALCL – Accessory Lateral Collateral Ligament
CAD – Computer-Aided Design
CT – Computed Topography
DOF – Degree of Freedom
EMG – Electromyography
FSI – Fluid-Structure Interaction
HA – Hyaluronic Acid
LMIC – Low and Middle-Income Countries
LUCL – Lateral Ulnar Collateral Ligament
MCL – Medial Collateral Ligament
MRI – Magnetic Resonance Imaging
RA – Rheumatoid Arthritis
RCL – Radial Collateral Ligament
RMS – Root Mean Square
ROM – Range of Motion
TEA – Total Elbow Arthroplasty
UCL – Ulnar Collateral Ligament

1 INTRODUCTION

1.1 Background

The need for total or partial replacement of the elbow joint may arise due to autoimmune diseases such as rheumatoid arthritis (RA), chronic injuries such as tennis elbow or golfer's elbow, or traumatic injuries such as accidents. In the realm of available treatment methods ranging from physical therapy, non-surgical methods such as steroid-based medication or ayurvedic medication, to minor surgical techniques such as tendon repair, total joint replacement is the last-resort method to restore the health of diseased joints.

One of the most prevalent reasons for degeneration of joints is RA. While the prevalence of RA, which has affected about 1.28-1.36 million people in US in 2014, is widely known [1], little is known about the extent to which this disease impairs the lives of millions in low and middle-income countries (LMIC) [2]. A 2015 study estimated that about 3.16 million males and 14.87 million females were affected by RA in LMIC in the year 2010 [2]. Although there is limited data on the number of elbow joint replacement surgeries worldwide, about 3,146 total elbow arthroplasty (TEA) surgeries were conducted in the US from 2007 to 2011 [3]. While elbow replacement is not as common as hip or knee replacement, given the significance of the elbow joint in the functioning of the upper extremity, the need for easier access to total elbow replacement surgeries, especially in LMIC, is obvious.

TEA is a surgical technique employed for total joint replacement in cases of RA or trauma. This surgery replaces the diseased elbow joint with artificial elbow joint

implants. In the past, these implants were based on fixed hinged models of the elbow joint. Contemporary practice involves the development of surgical implants based on linked hinged and unlinked TEAs. The linked hinged TEA is a semi-constrained elbow joint model with a mechanical connection between the humeral and ulnar components. The unlinked TEA has no physical contact between the humerus and the ulna and relies only on soft-tissue integrity for elbow stability [4].

While neither of these types of implants has clear superiority over the other, there is scope for improvement in implant designs overall. A 2016 study concludes that while there have been significant advancements in TEA, contemporary implant designers lack insight in elbow kinematics and dynamics [4]. The bottom line is that current surgical implants have a reasonably high success rate of restoring functionality of diseased joints, but complete functionality of the elbow joint is not achieved not only due to the lack of affordability, but also due to the lack of a clear understanding of elbow joint kinematics and dynamics.

In order to assist surgeons and implant designers in the development of highly anthropomorphic elbow joint replacements, an anatomically accurate computational model of the human elbow joint with a thorough understanding of the effects of biomechanics on joint dynamics is required.

1.2 Literature Review: Current Status of Elbow Joint Studies

Several researchers have developed mathematical and computational models to study the elbow joint. This section will cover the most relevant elbow joint studies, their contributions, and limitations.

In 2009, Fisk and Wayne developed and validated their "Computational Musculoskeletal Model of the Elbow and Forearm" to understand the dynamic behavior of the elbow joint when joint motion was governed by articular contact of 3D bone geometries, ligamentous constraints, muscle forces, and external disturbances [5]. They used 3D bone geometries derived from computed topography (CT) scans of anatomical specimens to develop joint articulations. Bones were assumed to be rigid bodies with six degrees of freedom that were constrained by ligaments and muscles. Ligaments were modeled as linear springs. Triceps brachii, biceps brachii, and brachialis were modeled as equal and opposite reaction forces defined by the function

$$F = kg^e + \left(\frac{dg}{dt}\right) f(c, d) \tag{1}$$

where k was stiffness, g was penetration depth, e was a constant equal to 2, c was penetration velocity, and d was damping coefficient.

Fisk and Wayne used COSMOS-Motion to simulate the rigid body dynamics of the elbow joint model [5]. The model was validated by simulating the moment of an average forearm and hand on the elbow, which was estimated to be 1.79 Nm. The joint angles resulting from this moment were compared to published elbow range of motion (ROM) data. Elbow flexion-extension ROM prediction of 160.5º was within one standard deviation of the results from published literature. However, the study concluded that the

larger prediction of flexion-extension ROM may be due to variable tension of the muscles crossing the elbow joint or omission of the joint capsule. This study not only predicted elbow ROM quite accurately, but also successfully computed ligament forces, joint contact forces, and 3D bone kinematics. But the study had limitations such as the omission of natural wrapping of ligament and muscles around articular structures and the exclusion of articular cartilage, joint capsule, and synovial fluid.

An improvement to the model developed by Fisk and Wayne was reported by M Rahman et al. in 2018 [6]. They presented a computational model of a subject-specific anatomically correct musculoskeletal elbow joint with consideration of the biomechanical influences of muscles, bones and ligaments, and evaluated their model based on experimental kinematics and muscle electromyography (EMG) measurements. Their model also included 3D bone geometry-influenced joint articulations. However, they constrained the joint with multiple ligament bundles naturally wrapped around bony structures and deformable contacts in ADAMS. The model considered three bundles each for the anterior and posterior parts of the medial collateral ligament (MCL), three bundles for the lateral ulnar collateral ligament (LUCL), three bundles for the radial collateral ligament (RCL), and two bundles for the annular ligament (AL). These ligaments were modeled as tension-only nonlinear springs governed by the function in equations 2 and 3

$$f = \begin{cases} 0.25k\,{\varepsilon^2}/{\varepsilon_l} & 0 \le \varepsilon \le 2\varepsilon_l \\ k(\varepsilon - \varepsilon_l) & \varepsilon > 2\varepsilon_l \\ 0 & \varepsilon < 0 \end{cases} \tag{2}$$

$$\varepsilon = \left(\frac{l - l_0}{l_0}\right) \tag{3}$$

where ε_l, spring parameter was fixed at 0.03, l was the length of each bundle, l_0 was the zero-load length of the ligament (determined by a laxity test), and k was the stiffness parameter. Articular cartilage was modeled as a frictionless, deformable contact constraint in ADAMS. M Rahman et al. included three major muscles in their model—triceps brachii, biceps brachii, and brachialis. In the inverse kinematic phase of the simulation, experimental motion data was used to drive the musculoskeletal model with articular and ligamentous constraints, and then the shortening/lengthening pattern of the muscles was recorded. In the forward dynamics phase of the simulation, the muscles actuated the rigid body dynamics of the elbow joint constrained by ligaments and articular contacts.

The model developed by M Rahman et al. was also able to predict important *in vivo* parameters such as ligament force and cartilage contact pressure [6]. More importantly, this model revealed that about 3º to 4º of varus-valgus laxity is possible during elbow flexion. In previous musculoskeletal models [7], [8], elbow joints were modeled as single degree-of-freedom joints compared to the 18 degrees of freedom available in the above-mentioned models [5], [6]. Such a simplification leads to the omission of the varus-valgus laxity among other important biomechanical influences. Neglecting this laxity in implant designs leads to the asceptic loosening of fully constrained elbow replacement implants [9]. M Rahman et al. concluded that some of the variations in their model could be attributed to the exclusion of the joint capsule from the model [6].

In his dissertation on ‘A Computational Musculoskeletal Model of the Human Elbow and Forearm in the Analysis of Ballistic Movements’, R. V. Gonzalez studied the

relationship between muscle excitation, individual muscle forces, and movement kinematics in elbow flexion/extension and forearm pronation/supination [10]. His model included eight musculotendon actuators—biceps brachii, brachialis, brachioradialis, triceps brachii, anconeus, pronator teres, pronator quadratus, and supinator—with the dynamics of the musculotendon actuator based on the Hill-type muscle model. While Gonzalez's model enables us to investigate the impact of muscle activation on the kinematics and kinetics of the elbow joint, it doesn't include any ligamentous or articular constraints and it simplifies the elbow joint into a 3 DOF joint—two active (radiohumeral and ulnohumeral joints) and one passive (radioulnar joint).

Several other studies have been conducted to investigate the correlation of muscle simulation to joint kinematics in elbow joint implants [11], [12]. These models either approach the elbow joint problem solely from a rigid body dynamics point-of-view or simplify the elbow joint into a purely mechanical single degree-of-freedom hinge joint. This facilitates faster computation as well as experimental validation of predicted muscle forces and joint kinematics. J Kusins et al. developed a computational elbow joint model that was driven by simulated active muscle forces instead of static muscle forces [11]. This ensured physiologically relevancy of the model and allowed them to validate the computational model with an established experimental elbow motion simulator that featured an Ulnohumeral and Radial Head Implant. They were successfully able to validate the muscle forces and joint kinematics of the elbow model with the data from the elbow motion simulator. However, this model did not include collateral ligaments and other secondary stabilizers such as articular contacts, joint capsule, and synovial fluid.

Similarly, Lemay and Crago developed dynamic model of the upper extremity to simulate forearm and wrist movements [12]. They modeled muscle activation based on the classic Hill-type muscle model and included passive moments derived from experimental data to simulate motion.

While the above discussed computational and dynamic models employed important parameters, modeling techniques, and validation methods, the intersection of the limitations of these studies is the omission of synovial fluid in computational elbow joint models.

To the best of my knowledge, at the time of this study, synovial fluid has not been included in computational or experimental elbow joint models. However, a team of researchers in Sun Yat-sen University, China studied the computational fluid dynamics of synovial fluid in a healthy temporomandibular joint during jaw opening [13]. They modeled synovial fluid as a homogeneous, incompressible Newtonian fluid with a density of 1010 kg/m^3 and a dynamic viscosity of 0.008 kg/m.s.

1.3 Objective

The objective of this study is to develop a computational model of the left human elbow joint to simulate FSI in the elbow joint i.e. simulate the effects of synovial fluid on articular cartilage during different joint velocity conditions of flexion, extension, pronation, and supination. Using this model, important *in vivo* parameters such as joint moments, ligament loads, articular cartilage stresses, and synovial fluid flow patterns will be predicted and analyzed. Joint dynamics in this computational model will be influenced by 3D bone-geometries, articular cartilage geometries, ligaments, muscles, and synovial fluid.

2 THEORY

2.1 Anatomy of the Elbow Joint

The human elbow joint is a compound joint comprising three articulations: radiohumeral joint, ulnohumeral joint, and proximal radioulnar joint. It is a highly congruous, trochoginglymus synovial joint that facilitates four major movements of the forearm: extension, flexion, pronation, and supination [14]. The anatomical position of the forearm is when the forearm is relaxed on the sides of the trunk with palms facing forward [15]. From this anatomical position, flexion and pronation of the forearm occur as shown in Fig. 1. To return to the anatomical position from the flexed and pronated states, extension and supination of the forearm occur, respectively, as shown in Fig. 1.

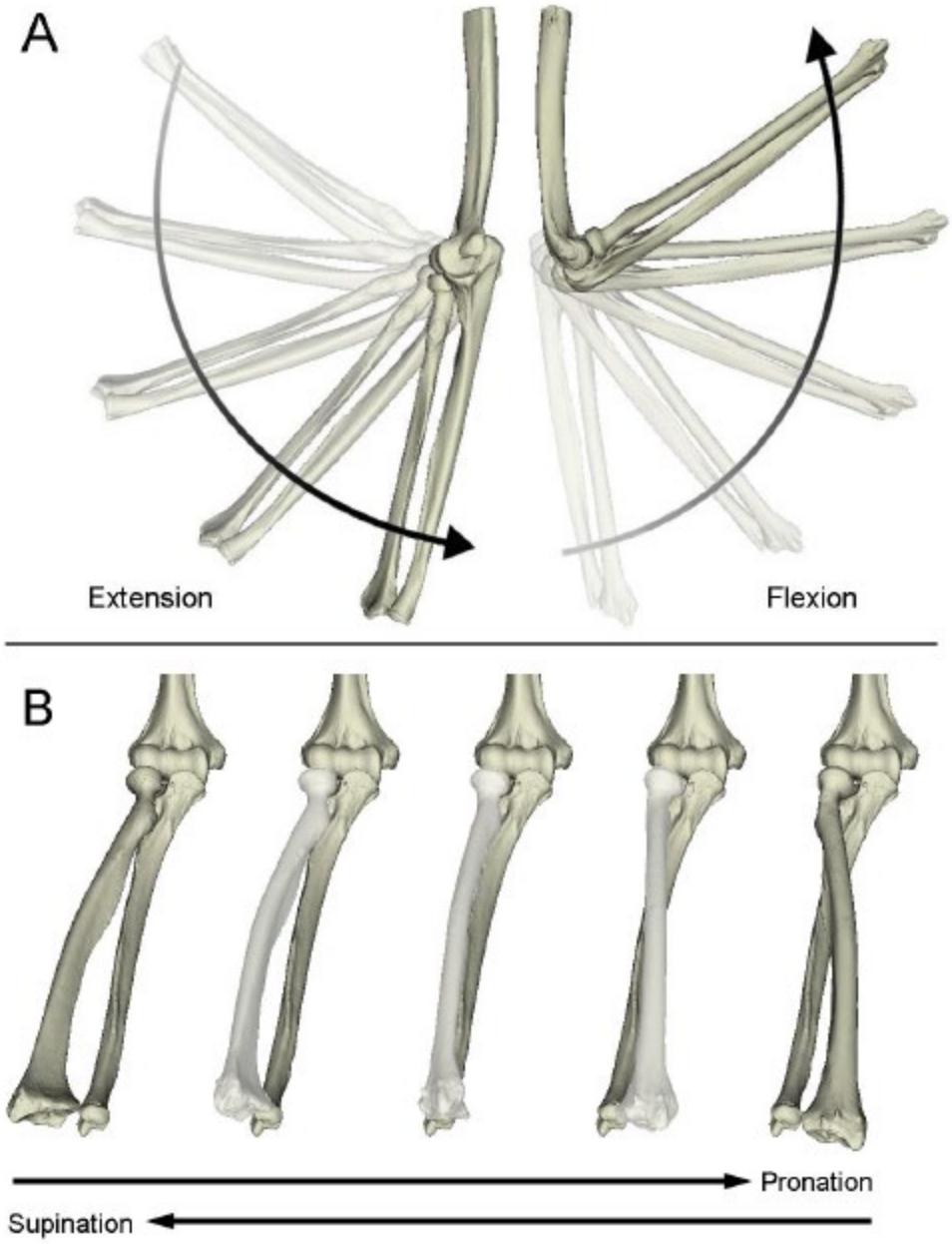

Fig. 1. (a) Forearm flexion-extension. (b) Forearm pronation-supination. [16]

Three bones—humerus, radius, and ulna—are responsible for the articulations of the elbow joint as shown in Fig. 2. The radiohumeral joint is the articulation between the radial head of the proximal radius and the capitulum of the distal humerus. It is a trochoid

(pivot) joint allowing for the pronation and supination of the forearm. And, the proximal radioulnar joint is the articulation between the radial head of the proximal radius and the radial notch of the proximal ulna. This is also a trochoid (pivot) joint allowing for the pronation and supination of the forearm. The ulnohumeral joint is the articulation between the trochlear notch of the proximal ulna and the trochlea of the distal humerus. This is a ginglymus (hinge) joint allowing for the flexion and extension of the forearm [14]. The structures inherent to the elbow joint can be broadly categorized into passive and active stabilizers. Bones and ligaments are classified as passive stabilizers, while muscles and tendons are classified as active stabilizers [14]. The following paragraphs cover the relevant highlights of each of these stabilizing structures.

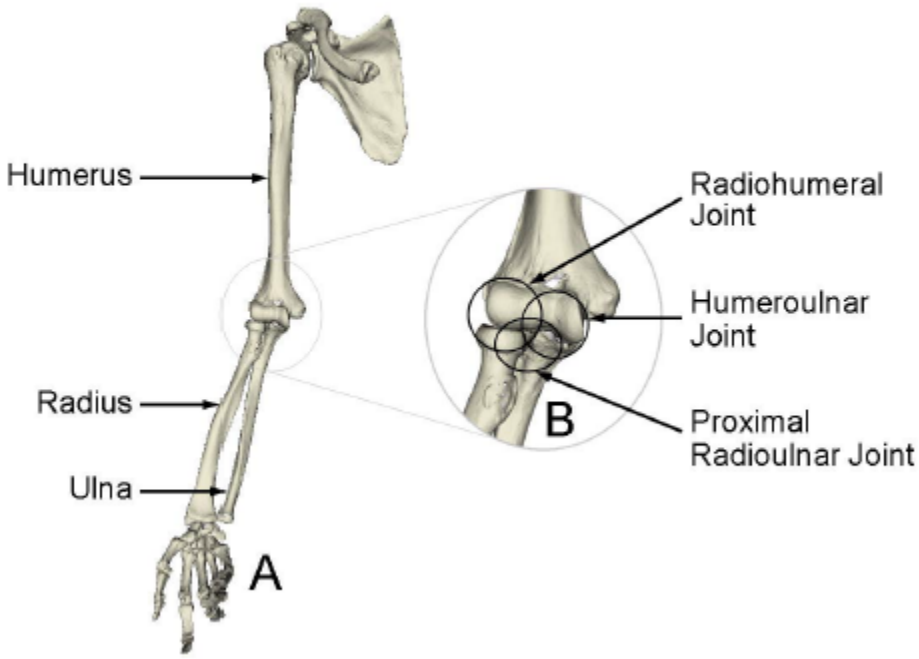

Fig. 2. Articulations of the elbow joint. [16]

The osteological areas of interest of the distal humerus are the condyles—capitulum and trochlea, epicondyles—lateral epicondyle and medial epicondyle, and fossae—radial fossa, coronoid fossa, and olecranon fossa; of the proximal ulna they are the trochlear notch, radial notch, coronoid process, and olecranon process; and of the proximal radius it is the radial head. These osteological areas are shown in Fig. 3 and Fig. 4. RCL and muscles responsible for extension and supination attach at the less prominent lateral epicondyle. However, the ulnar collateral ligament (UCL) and muscles responsible for flexion and pronation attach at the more prominent medial epicondyle. The radial fossa allows for the movement of the radial head of the proximal radius during flexion, the coronoid fossa allows for the movement of the coronoid process of the proximal ulna during flexion, and the olecranon fossa allows for the movement of the olecranon process of the proximal ulna during extension. The ulna of the forearm, in its anatomical position, is at an angle with the longitudinal axis of the humerus, resulting in what is known as the carrying angle of the elbow. In females, this carrying angle is an average valgus angulation of 13º to 16º, while in males, it is 11º to 14º [14].

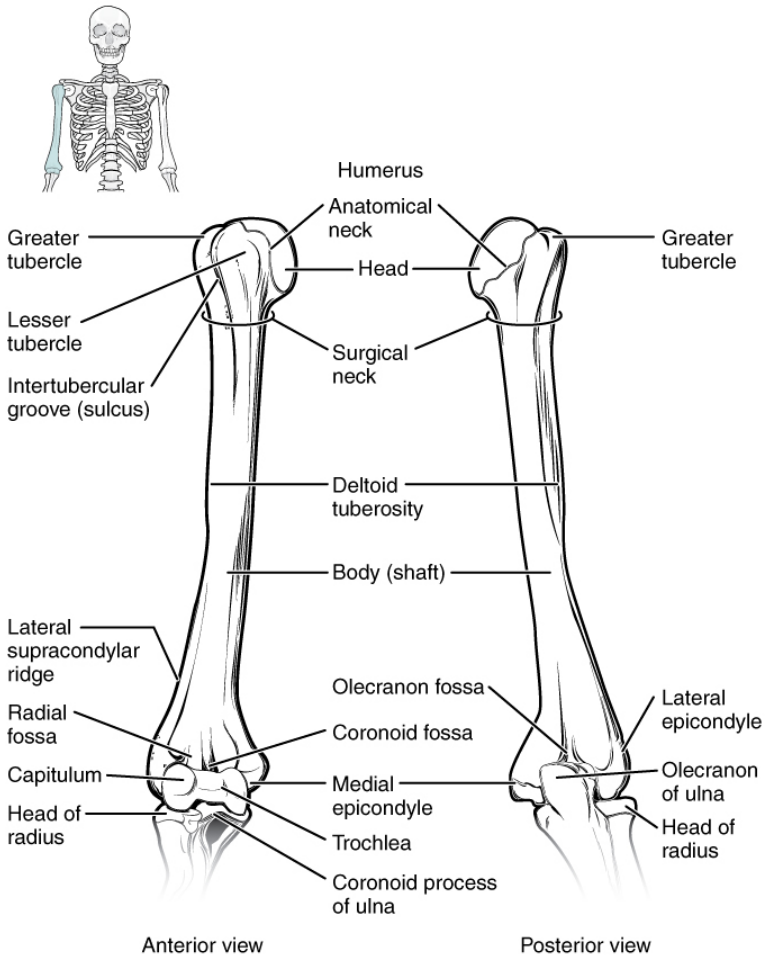

Fig. 3. Osteology of bones articulating the elbow joint (upper arm)—anterior view (left) and posterior view (right). [17]

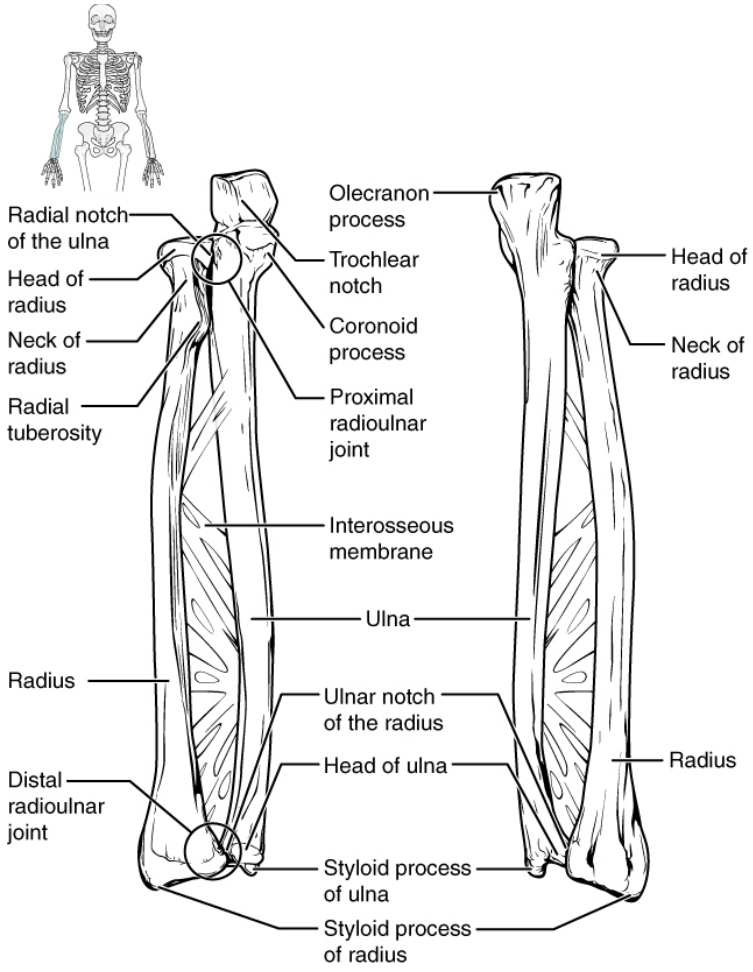

Fig. 4. Osteology of bones articulating the elbow joint (forearm)—anterior view (left) and posterior view (right). [17]

There are five ligaments/ligament complexes in the elbow joint—ulnar (medial) collateral ligament complex, radial (lateral) collateral ligament complex, quadrate ligament, oblique ligament, and interosseous membrane as shown in Fig. 4 and Fig. 5. The ulnar (medial) collateral ligament complex comprises the UCL which can be characterized into three bundles—anterior, posterior, and transverse. It originates from the broad, anteroinferior medial epicondylar surface of the distal humerus and inserts into the medial margins of the trochlear notch and coronoid process of the proximal ulna. The

radial (lateral) collateral ligament complex comprises of the RCL, LUCL, AL, and accessory lateral collateral ligament (ALCL). The origin and insertion points of RCL are at the lateral epicondyle and AL. The origin and insertion points of LUCL are at the lateral epicondyle and proximal ulna. AL ensures that the radial head and the radial notch of the ulna remain in contact at the proximal radioulnar joint. ALCL combines with AL and inserts into the ulna. Quadrate ligament, present between the AL and ulna, is thin and fibrous. Oblique ligament is a small structure of little functional significance between the radius and ulna. Interosseous membrane is a broad, thick fibrous tissue between the radius and ulna [14].

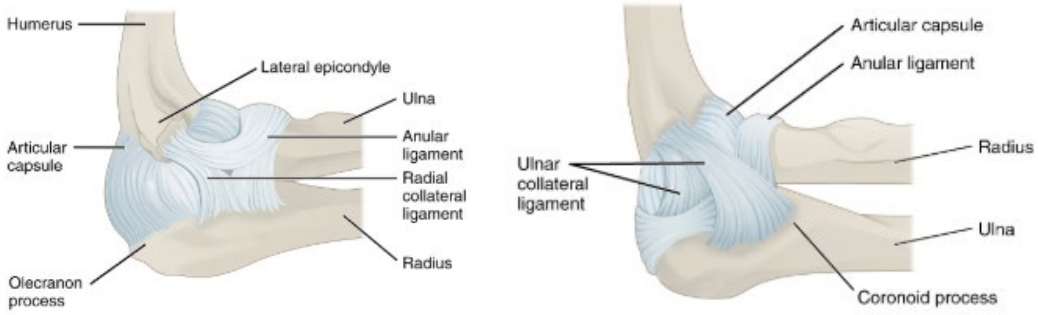

Fig. 5. Ligaments supporting the elbow joint—lateral view (left) and medial view (right). [18]

Ligamentous thickenings form the joint capsule of the elbow joint. Enclosed within the joint capsule is the synovium or synovial cavity. In a synovial joint, a thin layer of hyaline cartilage (articular cartilage) covers the ends of the bones that form joint articulations. The synovium consists of synovial fluid, a non-Newtonian fluid that lubricates the articular cartilage and along with the articular cartilage, acts as a shock absorber of the elbow joint [19]. Fig. 6 shows the section view of a synovial joint highlighting the presence of synovial fluid between the articular cartilages of the bones.

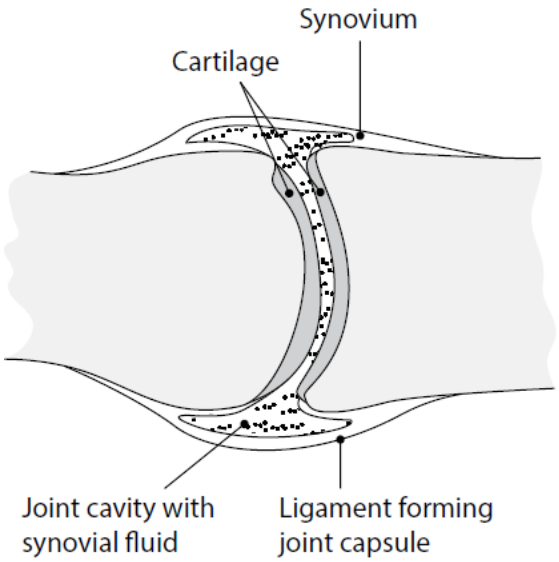

Fig. 6. Section view of a healthy synovial joint. [19]

Out of the 24 muscles that cross the elbow joint, seven musculotendon structures actuate the flexion-extension and pronation-supination movements of the elbow joint. Posteriorly, the triceps brachii and anconeus facilitate elbow extension. Laterally, the brachioradialis facilitates elbow flexion, while the supinator enables forearm supination. Anteriorly, the biceps brachii and brachialis enable elbow flexion, while the pronator teres influences forearm pronation [14].

2.2 Synovial Fluid Models

Synovial fluid is a non-Newtonian, viscoelastic fluid that not only reduces friction between articular cartilages during movement, but also acts a shock absorber in the elbow joint. From a biological standpoint, synovial fluid provides oxygen and nutrients to the articular cartilage and transports carbon dioxide and other metabolic wastes away from the articular cartilage [20]. Synovial fluid is an ultrafiltrate of blood plasma that is composed of hyaluronic acid (HA) at a concentration of 3-4 mg/ml, and a polymer of disaccharides consisting of D-glucuronic acid and D-N-acetylglucosamine. It is located inside the synovium which is a thin (approximately 50 μm) membranous lining [19], [20]. HA in synovial fluid is responsible for its non-Newtonian behavior [21]. The viscoelastic nature of synovial fluid can be characterized as shear thinning and thixotropic [22], [23]; i.e. the viscosity of synovial fluid is dependent on the shear rate that the fluid is subjected to by the surrounding cartilage as well as the time during which this shear loading acts. At low shear rates, synovial fluid has very high viscosity and as the shear rate increases, synovial fluid viscosity decreases progressively [22].

Furthermore, there is a clear downward trend of synovial fluid viscosities as age increases. In general, an increase in age is associated with an increase in body weight and a decrease in joint movement velocity. When such physiological changes are coupled with a decrease in synovial fluid viscosity, the functional efficiency of the joint is drastically affected, leading to osteoarthritic joint diseases [23]. Based on the work performed by Jebens and Monk-Jones, Table 1 shows that the viscosities of pathological synovial fluids are lower than the viscosities of normal synovial fluids [23].

Table 1
Synovial Fluid Viscosities for
Normal and Pathological Fluids

Synovial Fluid Viscosities of Normal and Pathological Fluids		
Fluid Type	Intrinsic Viscosity	
	Sundblad	Bollet
Normal	39.3	69.3±4.2
Traumatic	39.1±1.1	32.5±1.7
Lesions of the cartilage	30.1±1.8	
Osteoarthritic	29.8±1.4	49.8±5.8

Jebens and Monk-Jones presented a correlation between the viscosity of normal synovial fluid and age as shown in equation 4

$$\eta = 12.6 - 0.11A \tag{4}$$

where η is the viscosity in poise, and A is the age in years [23]. This curve is shown in Fig. 7 [23].

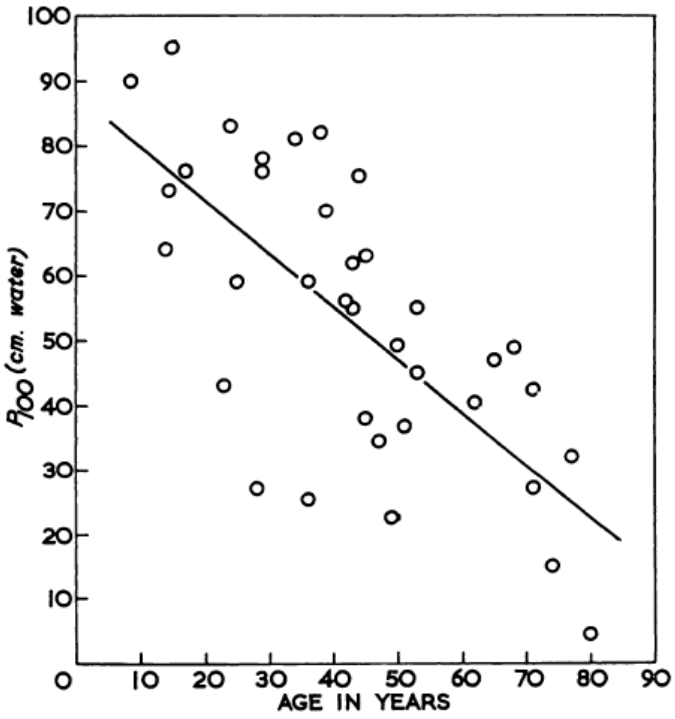

Fig. 7. Decrease in synovial fluid viscosities with age. [23]

Hron et al. modeled synovial fluid as a power-law type fluid with the power-law viscosity exponent dependent on the concentration of HA in synovial fluid as shown in equations 5 and 6

$$\mu = \mu_0(\beta + \gamma|D|^2)^{n(c)} \tag{5}$$

$$n(c) = \omega(\frac{1}{\alpha c^2+1} - 1) \tag{6}$$

where the parameters α, β, γ, ω are equal to 31.0, 1.3e-8, 8.5e-8, and 0.44, respectively [25].

3 METHODOLOGY

3.1 Computational Model Overview

ANSYS 19.1 was used to develop a computational model of the left human elbow joint to simulate FSI between synovial fluid and articular cartilage in the elbow joint. All references to the elbow joint hereafter imply the human elbow joint of the left upper extremity.

The project schematic in ANSYS Workbench involved three main simulation components: Transient Structural, Fluid Flow (Fluent), and System Coupling. Fig. 8 shows a snapshot of the project schematic in ANSYS Workbench. Solidworks 2018 was used to develop the various geometrical components of the elbow joint, while ANSYS Spaceclaim was used to assemble these components for the FSI simulations. ANSYS Transient Structural was used to model the structural mechanics of the elbow joint, while ANSYS Fluent was used to model the fluid mechanics of the elbow joint. ANSYS System Coupling was used to synchronize the structural and fluid simulations, thereby simulating the FSI of synovial fluid and articular cartilage in the elbow joint during joint motion.

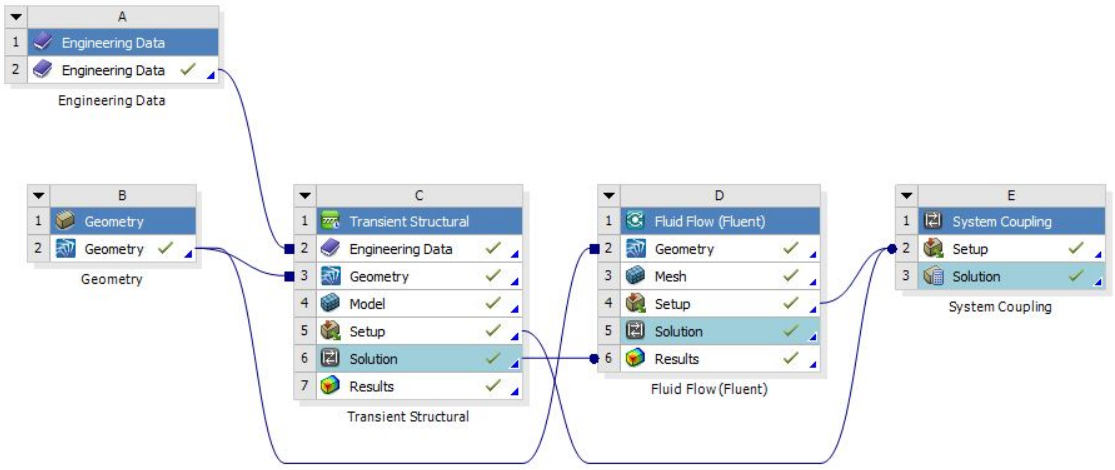

Fig. 8. Simulation workflow for the computational elbow joint model—a snapshot from ANSYS 19.1

In this study, FSI in the elbow joint was simulated for eight different elbow joint motion conditions. These conditions are:

1. Flexion at 20º/s
2. Flexion at 120º/s
3. Extension at 20º/s
4. Extension at 120º/s
5. Pronation at 40º/s
6. Pronation at 120º/s
7. Supination at 40º/s
8. Supination at 120º/s

3.2 Model Development

This section outlines the details of the various anatomical components that comprise the computational model of the left elbow joint.

3.2.1 Bones

In this left elbow joint model, 3D geometries of humerus, radius, and ulna were used to model joint articulations for flexion-extension, and pronation-supination. These 3D bone geometries were acquired from Zygote Media Group which develops anatomically accurate Computer-Aided Design (CAD) models of human musculoskeletal systems. Zygote Media Group develops CAD models of the human musculoskeletal systems based on CT and Magnetic Resonance Imaging (MRI) scans of a 50^{th} percentile human male [26]. Fig. 9, Fig. 10, Fig. 11 show the 3D geometries of humerus, radius, and ulna procured from Zygote Media Group. The mechanical properties used to define bones in this elbow joint model are shown in Table 2 [6], [27].

Fig. 9. 3D bone geometry of humerus—left upper arm.

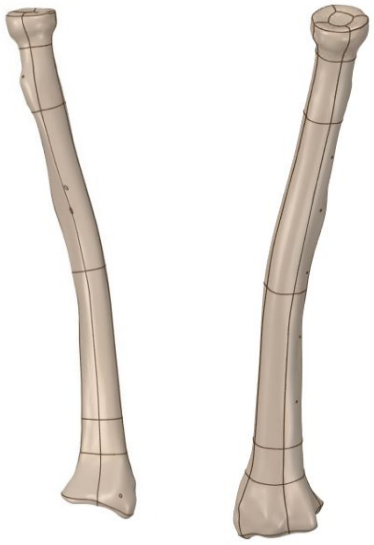

Fig. 10. 3D bone geometry of radius—left forearm.

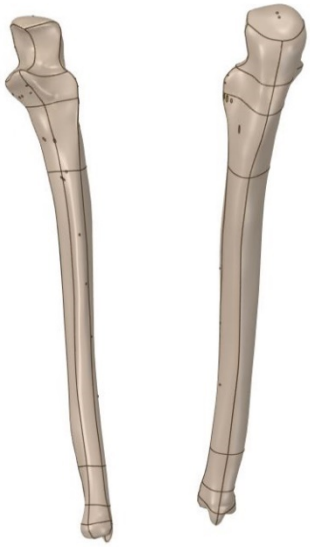

Fig. 11. 3D bone geometry of ulna—left forearm.

Table 2
Material Properties of Bone

Material Properties of Bone		
Parameter	Value	Units
Density	1600	kg/m^3
Young's Modulus - X	7	GPa
Young's Modulus - Y	7	GPa
Young's Modulus - Z	11.5	GPa
Poisson's Ratio	0.4	
Shear Modulus - XY	2.6	GPa
Shear Modulus - YZ	3.5	GPa
Shear Modulus - XZ	3.5	GPa

3.2.2 Articular Cartilage

Due to the lack of the articular cartilage geometries derived from humans, articular cartilage geometries used in this elbow joint model were developed by manipulating the 3D bone-geometries of humerus, radius, and ulna. Specifically, articular cartilage geometries were created by applying the 'surface offset' and 'thicken' tools in Solidworks on relevant faces of the 3D bone geometries. Therefore, 3D geometries of humerus, radius, and ulna were used to develop the 3D geometries of distal humerus articular cartilage, proximal radius articular cartilage, and proximal ulna articular cartilage, respectively.

A uniform thickness of 0.4 mm was applied to the articular cartilage geometries based on literature [28]. Fig. 12, Fig. 13, Fig. 14 show the isometric views of the 3D geometries of distal humerus articular cartilage, proximal radius articular cartilage, and proximal ulna articular cartilage. The mechanical properties used to define articular cartilage in this elbow joint model are shown in Table 3 [6], [27].

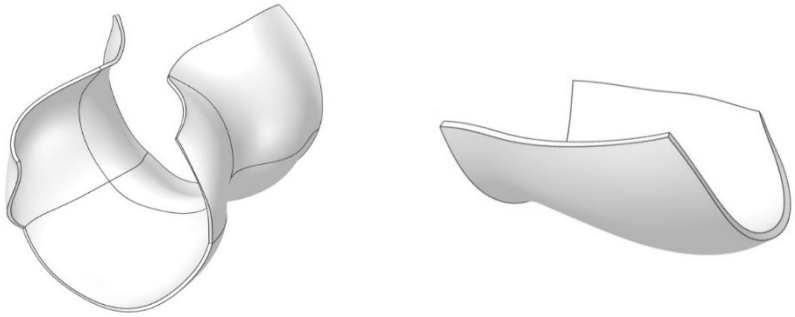

Fig. 12. 3D geometry of distal humerus articular cartilage—flexion-extension model (left) and pronation-supination model (right).

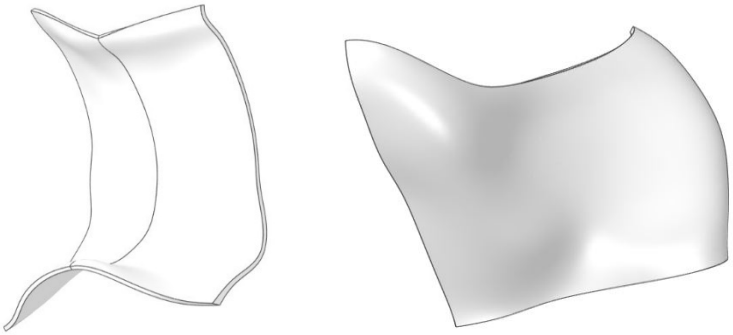

Fig. 13. 3D geometry of proximal ulna articular cartilage—flexion-extension model (left) and pronation-supination model (right).

Fig. 14. 3D geometry of proximal radius articular cartilage—pronation-supination model

Table 3
Material Properties of Articular Cartilage

Material Properties of Articular Cartilage		
Parameter	Value	Units
Density	1000	kg/m^3
Young's Modulus	0.012	GPa
Poisson's Ratio	0.35	
Bulk Modulus	0.0133	GPa
Shear Modulus	0.0044	GPa

3.2.3 Ligaments

Ligaments were modeled using the longitudinal spring contact pair available in ANSYS Transient Structural. These springs were inserted directly between the ligament attachment sites which were derived from published literature [24]. To isolate the ligament attachment sites on the 3D bone geometries, the 'imprint face' tool available in ANSYS Spaceclaim was used. These imprinted faces, analogous to the anatomical ligament attachment sites, were used to insert the longitudinal springs in ANSYS Transient Structural. The stiffness parameters for the ligaments were derived from a study published by Fisk and Wayne in 2009 [5]. The parameters used to define ligaments in this elbow joint model are shown in Table 4 [5].

Table 4
Properties of Ligaments

Properties of Ligaments				
Description	Effective Stiffness (N/m)	Number of Springs	Reference Contact	Mobile Contact
Annular	28,500	2	Deformable	Deformable
Interosseous Membrane	41,950	5	Deformable	Deformable
Lateral Ulnar Collateral	57,000	1	Deformable	Deformable
Medial Collateral - Anterior	72,300	1	Deformable	Deformable
Medial Collateral - Posterior	52,200	1	Deformable	Deformable
Radial Collateral	15,500	1	Deformable	Deformable

3.2.4 Muscles

In 2005, Katherine Holzbaur, Wendy Murray, and Scott Delp published the moment generated at the elbow joint by elbow flexors, extensors, pronators, and supinators versus elbow flexion, extension, pronation, and supination angles, respectively [29]. Fig. 15 shows the data that was published in their study, which has been reprinted here with permission. The bold, black curve outlines the data published by Holzbaur et al.

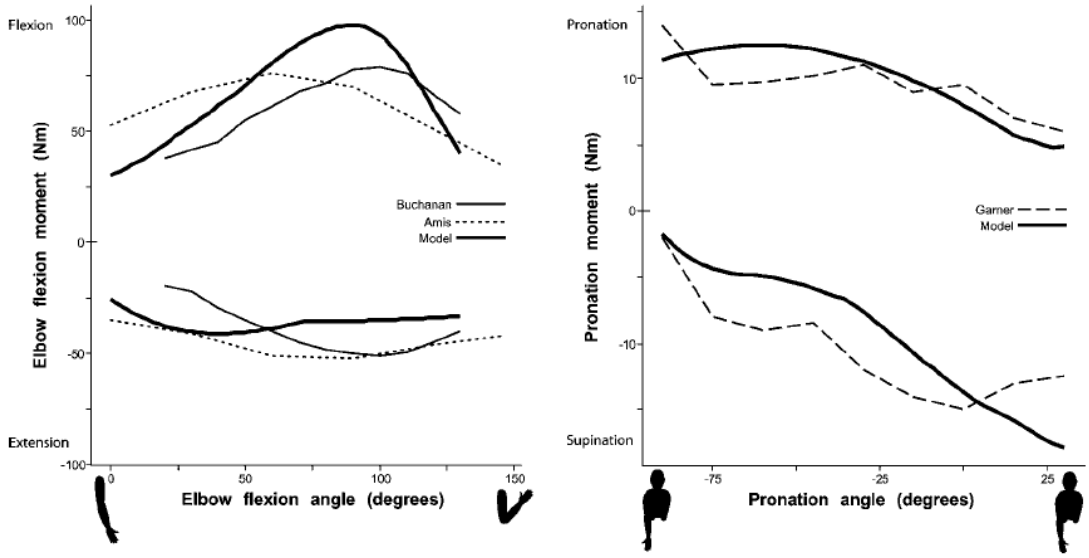

Fig. 15. Elbow moment versus rotation angle data—flexion-extension (left) and pronation-supination (right). Reprinted by permission from Springer Nature: Springer *Annals of Biomedical Engineering* [29] © Biomedical Engineering Society 2005.

To simulate the stiffness characteristics of muscles in this elbow joint model, joints for flexion, extension, pronation. and supination were defined with non-linear stiffness characteristics that correlated the joint moment with relative rotation based on published data [29]. For each type of joint motion, i.e., flexion, extension, pronation, and supination, distinct joints with non-linear stiffness characteristics were defined in ANSYS Transient Structural. Table 5, Table 6, Table 7, and Table 8 and Fig. 16, Fig. 17, Fig. 18, and Fig. 19 show the non-linear stiffness characteristics of the joints for flexion, extension, pronation, and supination [29].

Table 5
Non-linear Joint Stiffness for Flexion
due to Elbow Flexors

Non-linear Joint Stiffness for Flexion due to Elbow Flexors	
Relative Rotation - Z Axis (º)	Moment - Z Axis (N.m)
0	31.25
25	50.00
50	68.75
75	87.50
100	103.00
125	45.00

Table 6
Non-linear Joint Stiffness for Extension
due to Elbow Extensors

Non-linear Joint Stiffness for Extension due to Elbow Extensors	
Relative Rotation - Z Axis (º)	Moment - Z Axis (N.m)
0	25.00
25	40.00
50	43.00
75	33.00
100	31.25
125	30.00

Table 7
Non-linear Joint Stiffness for Pronation
due to Elbow Pronators

Non-linear Joint Stiffness for Pronation due to Elbow Pronators	
Relative Rotation - Z Axis (º)	Moment - Z Axis (N.m)
0	11.25
25	12.50
50	12.00
75	11.25
100	7.50
125	5.00

Table 8
Non-linear Joint Stiffness for Supination
due to Elbow Supinators

Non-linear Joint Stiffness for Supination due to Elbow Supinators	
Relative Rotation - Z Axis (º)	Moment - Z Axis (N.m)
0	2.50
25	3.75
50	5.00
75	8.75
100	13.50
125	18.00

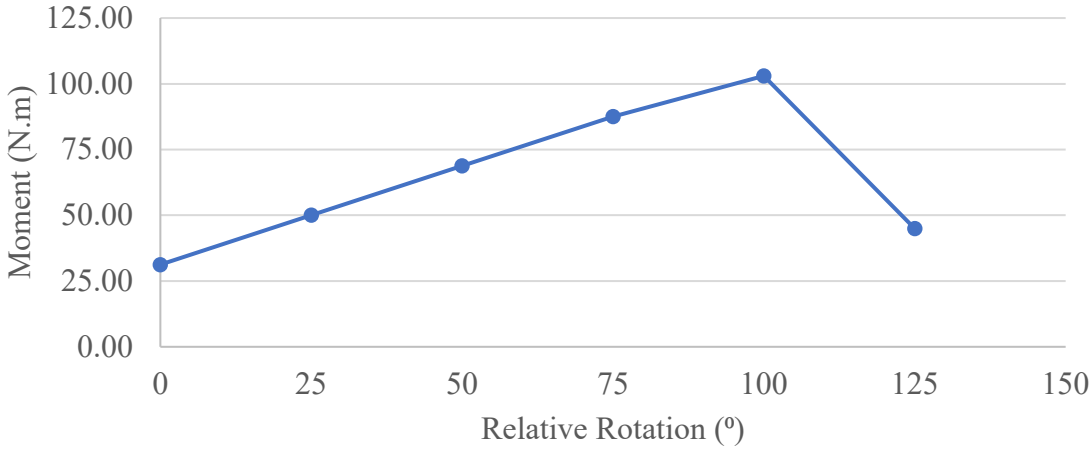

Fig. 16. Non-linear joint stiffness curve for flexion due to elbow flexors.

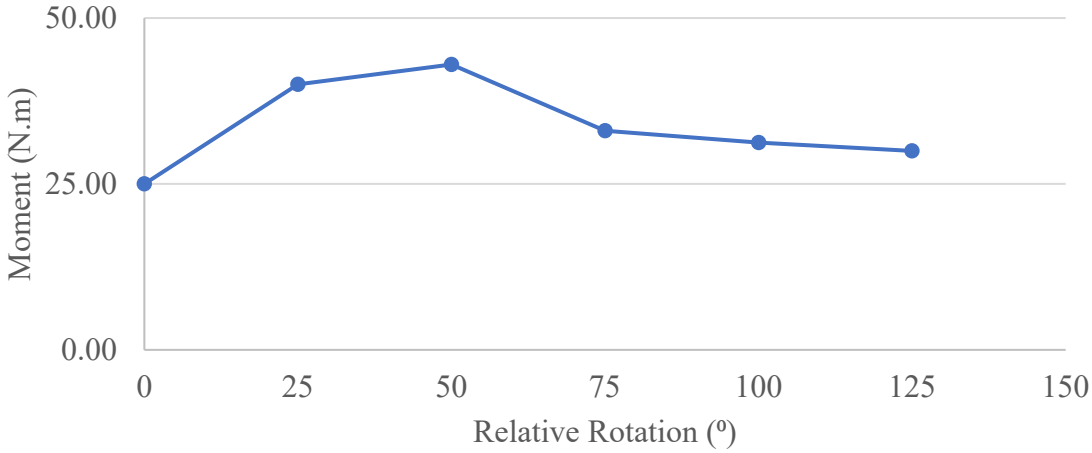

Fig. 17. Non-linear joint stiffness curve for extension due to elbow extensors.

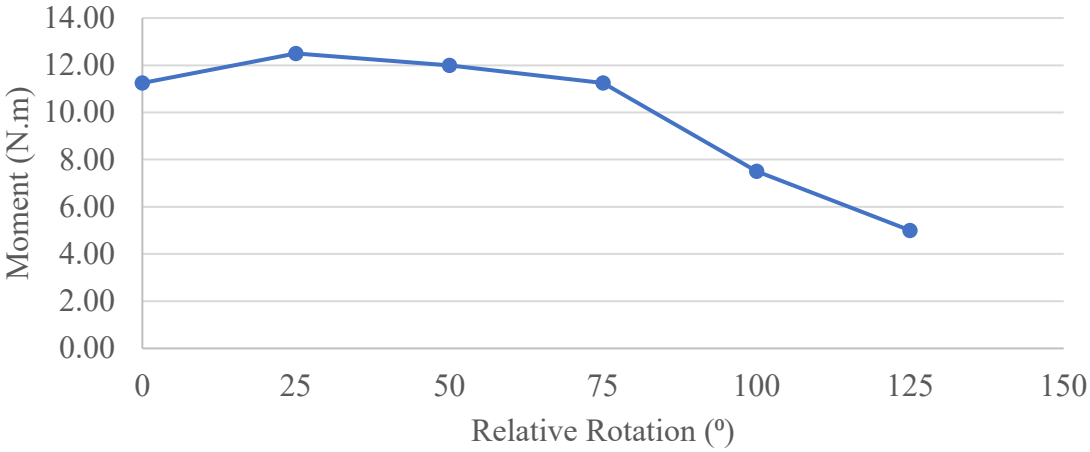

Fig. 18. Non-linear joint stiffness curve for pronation due to elbow pronators.

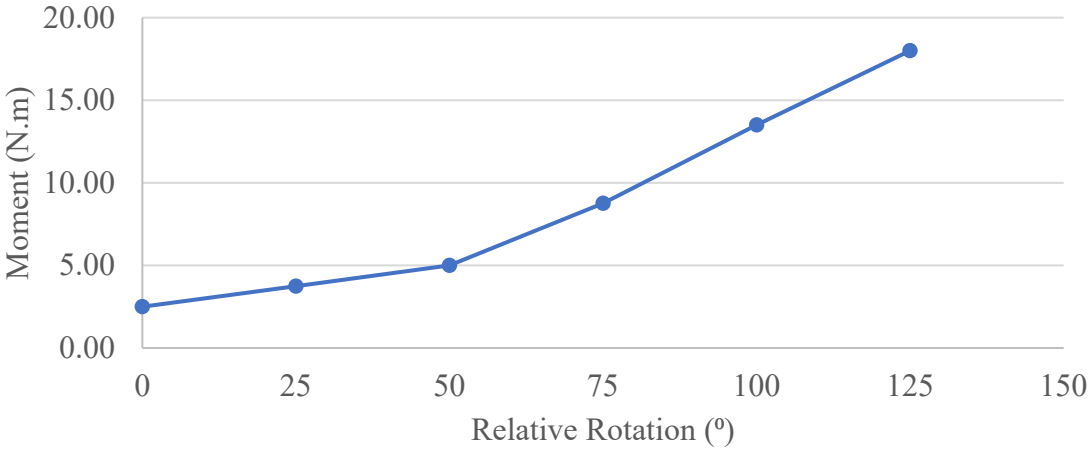

Fig. 19. Non-linear joint stiffness curve for supination due to elbow supinators.

3.2.5 Synovial Fluid

Although there has been significant progress in modeling the non-Newtonian characteristics of synovial fluid as outlined in Section 2.2, there was no information that defined synovial fluid based on the non-Newtonian fluid models supported by ANSYS Fluent. Therefore, synovial fluid was modeled as a homogeneous, incompressible, Newtonian fluid [13] with an intra-articular pressure of 557.5 mm Hg or 74,327 Pa [30]. Table 9 shows the parameters used to define synovial fluid in this elbow joint model [13], [30].

Table 9
Properties of Synovial Fluid

Properties of Synovial Fluid		
Parameter	Value	Units
Density	1010	kg/m^3
Dynamic Viscosity	0.008	kg/(m.s.)
Intra-Articular Pressure	74327	Pa
Inlet Velocity	0.01	m/s

3.2.6 Synovial Cavity as an Enclosure

The fluid mechanics of the elbow joint was modeled in ANSYS Fluent using an approximated synovial cavity. Due to the technical difficulties associated with procuring 3D geometries of the synovial cavity in the elbow joint from human specimens, a novel approach was implemented to simulate the presence of synovial fluid in the elbow joint. Using ANSYS Spaceclaim, an enclosure was created around the proximal ulna articular cartilage and the proximal radius articular cartilage for the flexion-extension and pronation-supination models, respectively. Thus, the articular cartilage geometries were

modeled as a cavity inside the enclosure. These enclosures were then initialized as fluid domains in ANSYS Fluent, thereby surrounding the proximal ulna articular cartilage and the proximal radius articular cartilage with synovial fluid in the flexion-extension and pronation-supination models, respectively. However, this approach results in the presence of excess synovial fluid in areas outside the anatomical synovial cavity. The effects of excess synovial fluid on FSI in the elbow joint model were mitigated by defining appropriate boundary conditions that accurately simulate the mechanical characteristics of synovial fluid in the elbow joint.

3.3 Flexion-Extension Model

This section outlines the specific geometries and parameters that were used to model flexion and extension of the elbow joint in ANSYS Transient Structural, ANSYS Fluent, and ANSYS System Coupling.

3.3.1 Flexion-Extension: Transient Structural

3D geometries of humerus, radius, ulna, distal humerus articular cartilage, and proximal ulna articular cartilage were used to model the structural mechanics of flexion and extension of the elbow joint in ANSYS Transient Structural.

3.3.1.1 Flexion-extension: Transient Structural: joint axis: The flexion-extension joint was modeled as a single DOF ulnohumeral joint with the joint axis passing between the inferior medial epicondyle and center of the lateral epicondyle [14]. Specifically, the flexion-extension joint was defined as a general ‘body-body’ joint between distal humerus and proximal ulna. Since ANSYS does not allow the user to define non-linear stiffness characteristics for revolute joints, a general joint was used with all degrees of freedom except rotation in z-axis constrained. The ability to define the joint with non-linear stiffness characteristics was important to establish the constraint moment generated by elbow flexors and extensors during flexion and extension, respectively.

3.3.1.2 Flexion-extension: Transient Structural: bones: Humerus was constrained to the ground using a fixed ‘body-ground’ joint with rigid contacts enabled as shown in Fig. 20. Radius was constrained to ulna using a fixed ‘body-body’ joint with rigid contacts enabled as shown in Fig. 20. As discussed in Section 3.3.1.1, ulna was constrained to humerus using a general ‘body-body’ joint with rigid contacts enabled and rotation in z-axis as the only active DOF as shown in Fig. 21.

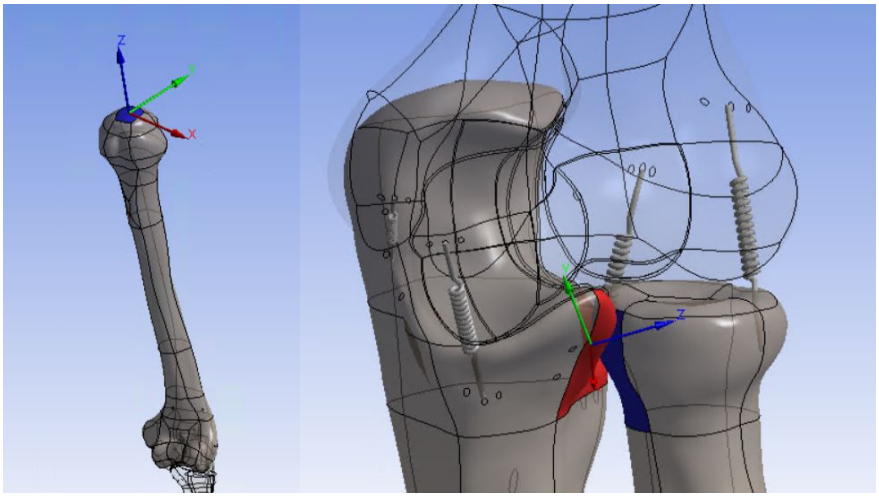

Fig. 20. Bone joints in the flexion-extension model—distal humerus constrained to ground with a fixed joint (left) and proximal radius constrained to proximal ulna with a fixed joint (right).

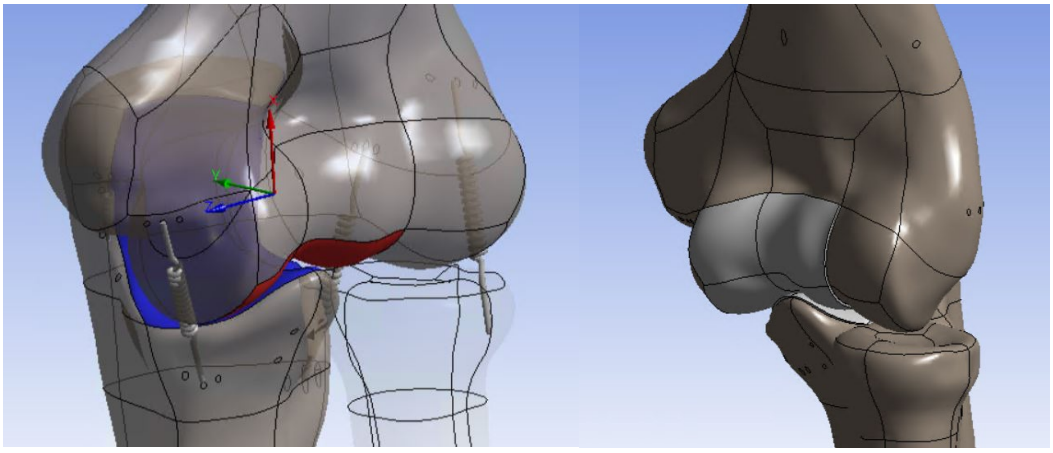

Fig. 21. Flexion-Extension joint in the flexion-extension model—proximal ulna constrained to distal humerus with a general joint (rotation in z-axis is the only active DOF) (left) and isometric view of the elbow joint articulation for the flexion-extension joint model (right).

3.3.1.3 Flexion-extension: Transient Structural: articular cartilage: Articular cartilage geometries were attached to the bones using fixed 'body-body' joints with rigid contacts enabled as shown in Fig. 22.

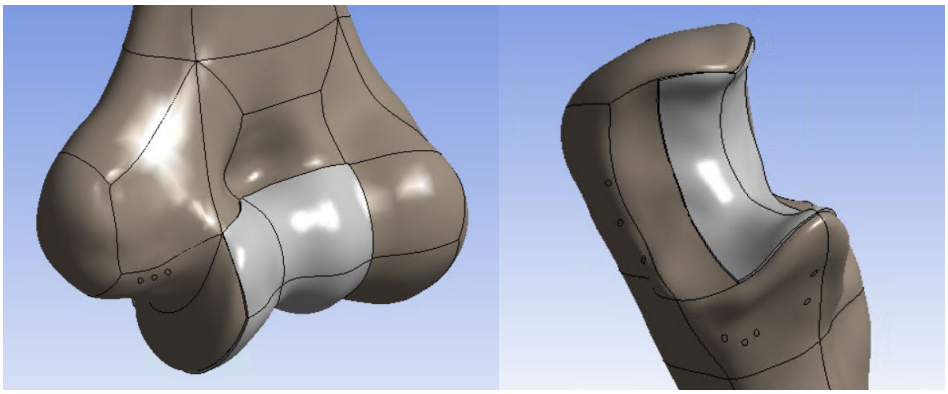

Fig. 22. Articular Cartilage joints in the flexion-extension model—distal humerus articular cartilage constrained to distal humerus (left) and proximal ulna articular cartilage constrained to proximal ulna (right).

To minimize the computational load of the FSI simulations, only moving cartilage bodies were considered for fluid-structure interfaces. Therefore, humerus, radius, ulna, and distal humerus articular cartilage were defined as rigid bodies while proximal ulna articular cartilage was defined as a flexible body in ANSYS Transient Structural. Thus, a fluid-solid interface boundary condition was applied to all the faces of the proximal ulna articular cartilage.

For the purposes of meshing in ANSYS Transient Structural, all the rigid bodies were dimensionally reduced. The only flexible body, proximal ulna articular cartilage geometry was meshed using the 'Patch Conforming Method' with tetrahedral elements of size 0.8 mm as shown in Fig. 23. Adaptive mesh sizing and mesh defeaturing with fine resolution settings were enabled. Fig. 23 shows the mesh element quality of proximal ulna articular cartilage geometry.

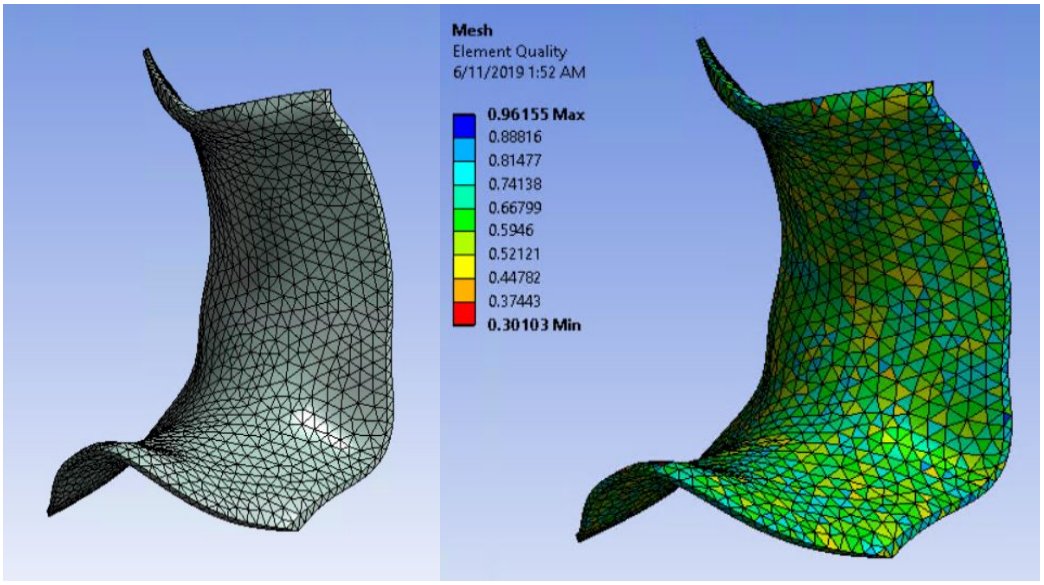

Fig. 23. Articular Cartilage mesh in the flexion-extension model—tetrahedral mesh of proximal ulna articular cartilage (left) and mesh element quality of proximal ulna articular cartilage (right).

3.3.1.4 Flexion-extension: Transient Structural: ligaments: LUCL, RCL, MCL-Anterior, and MCL-Posterior were modeled as longitudinal springs inserted between anatomical ligament attachment sites [24] as shown in Fig. 24, Fig. 25. All relevant parameters for these tension-compression springs were defined as discussed in Section 3.2.3.

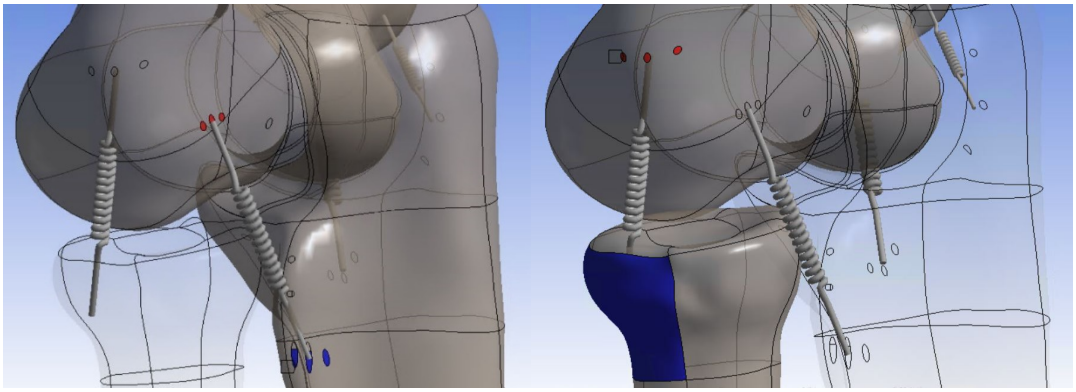

Fig. 24. Ligaments in the flexion-extension model—LUCL (left) and RCL (right).

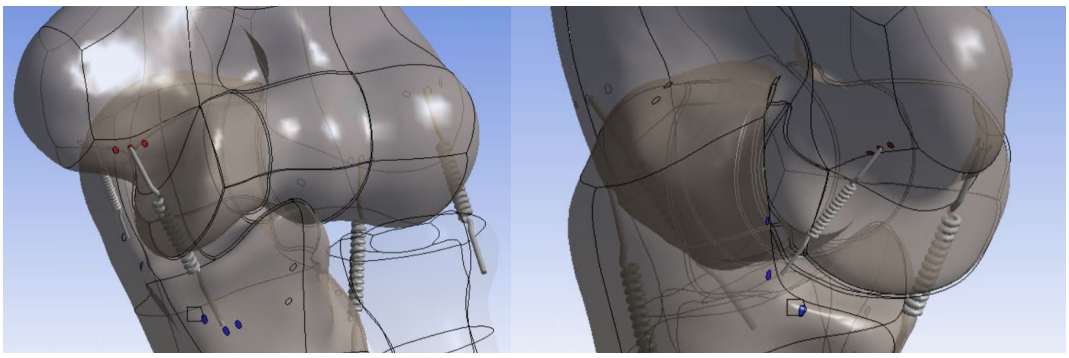

Fig. 25. Ligaments in the flexion-extension model—MCL-Anterior (left) and MCL-Posterior (right).

3.3.1.5 Flexion-extension: Transient Structural: muscles: Non-linear stiffness characteristics were applied to the flexion-extension joint to simulate the stiffness of elbow flexors and extensors for elbow flexion and extension, respectively as discussed in Section 3.2.4.

3.3.1.6 Flexion-extension: Transient Structural: joint loads: Standard earth gravity of 9.8066 m/s^2 was enabled and a rotation joint load was applied to the flexion-extension joint to simulate joint motion. Since none of the parameters used in the simulation were time-dependent, the simulations were conducted with transient effects disabled.

Four different FSI simulations were conducted based on the flexion-extension model. All parameters except joint loading conditions and non-linear stiffness parameters of the flexion-extension joint were consistent for all the FSI simulations. The details of joint loading conditions and non-linear stiffness parameters of the flexion-extension joint for each FSI simulation are shown in Table 10. The graphs for these joint loading conditions are shown in Fig. 26, Fig. 27, Fig. 28, Fig. 29. To simulate elbow extension, a full flexion-extension simulation was conducted with non-linear stiffness parameters pertaining to elbow extensors.

Table 10
Joint Loading Conditions for
Flexion-Extension FSI Simulations

Joint Loading Conditions for Flexion-Extension FSI Simulations		
FSI Simulation Description	Joint Loading Description	Joint Non-Linear Stiffness Conditions
Flexion at 20º/s	See Fig. 26	Elbow Flexors - See Fig. 16
Flexion at 120º/s	See Fig. 27	Elbow Flexors - See Fig. 16
Extension at 20º/s	See Fig. 28	Elbow Extensors - See Fig. 17
Extension at 120º/s	See Fig. 29	Elbow Extensors - See Fig. 17

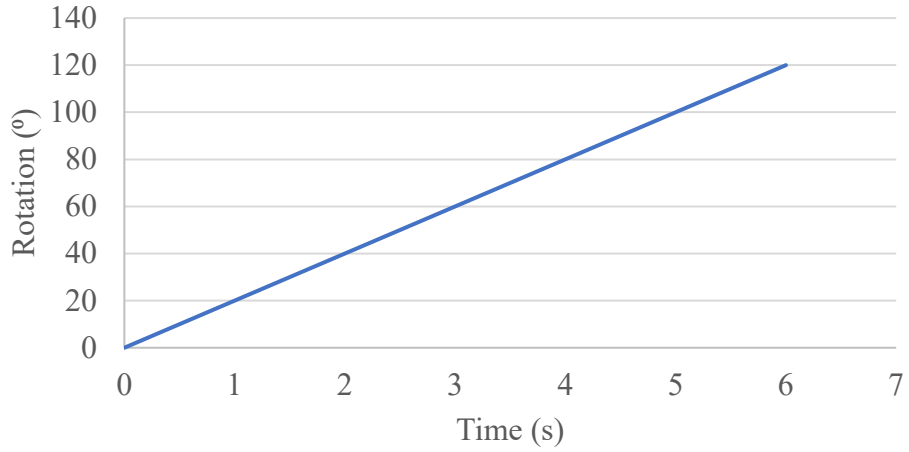

Fig. 26. Joint rotation load for flexion at 20º/s.

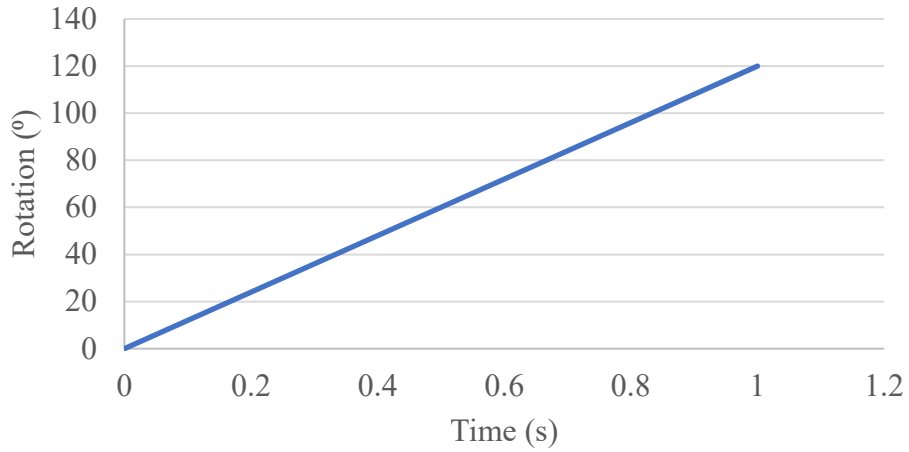

Fig. 27. Joint rotation load for flexion at 120º/s.

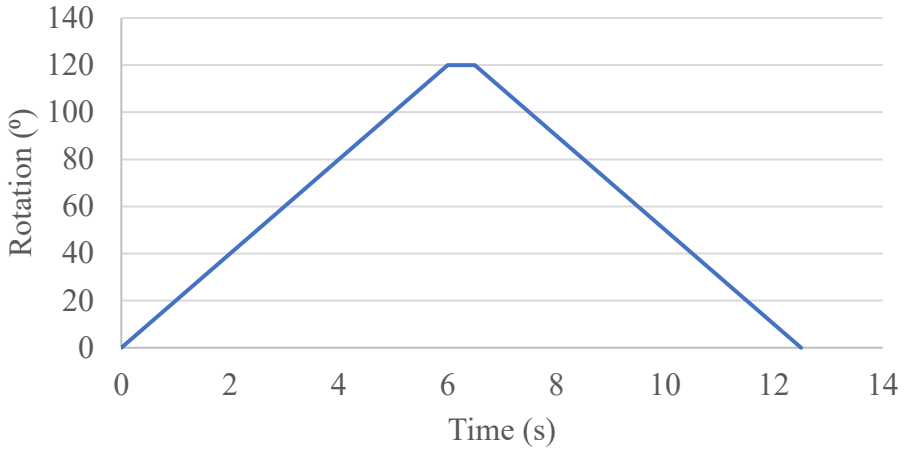

Fig. 28. Joint rotation load for extension at 20º/s.

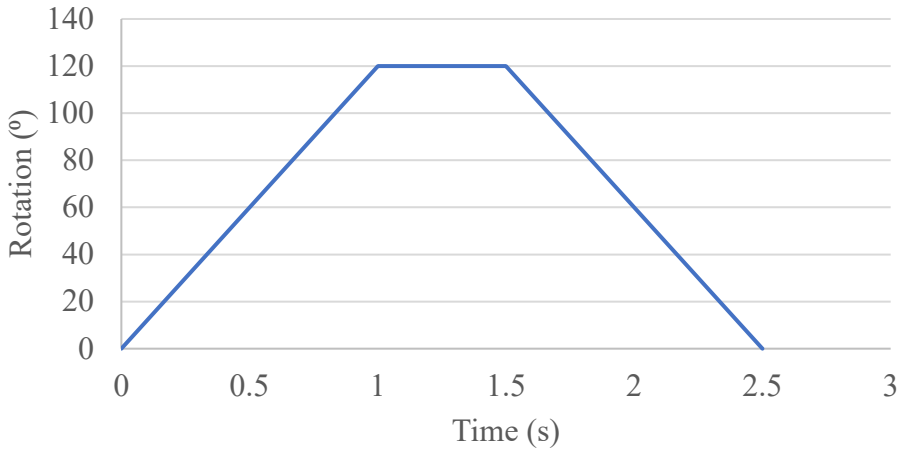

Fig. 29. Joint rotation load for extension at 120º/s.

3.3.2 Flexion-Extension: Fluent

3.3.2.1 Flexion-extension: Fluent: synovial fluid enclosure: As discussed in Section 3.2.6, a synovial fluid enclosure was created around the proximal ulna articular cartilage, thereby rendering the proximal ulna articular cartilage as a cavity inside the fluid domain. Fig. 30 shows the synovial fluid enclosure with the faces of proximal ulna articular cartilage geometry highlighted in red.

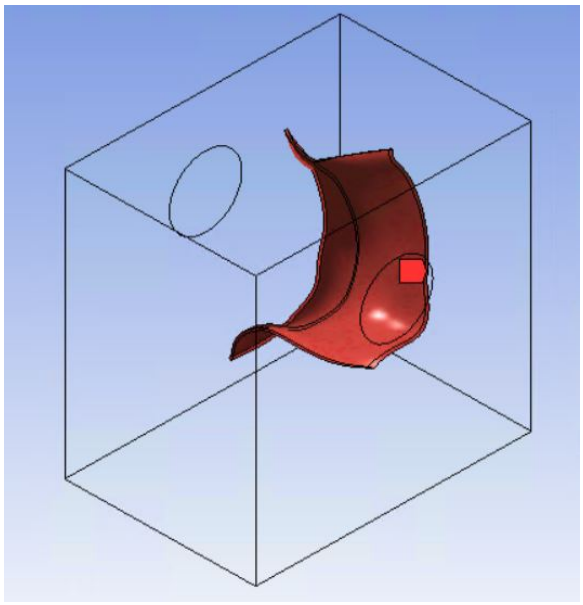

Fig. 30. Proximal ulna articular cartilage in the fluid domain (faces highlighted in red).

3.3.2.2 Flexion-extension: Fluent: mesh: The synovial fluid domain for flexion-extension was meshed using the ‘Patching Conforming Method’ with tetrahedral elements of size 0.01 m as shown in Fig. 31. Fig. 31 shows a section view of the fluid domain mesh. The mesh elements that were near the proximal ulna articular cartilage cavity were controlled with an element size of 0.001 m. Fig. 32 shows the mesh element quality of the fluid domain geometry.

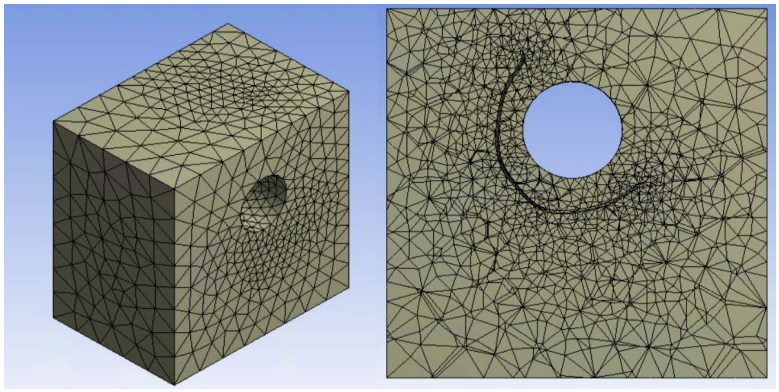

Fig. 31. Fluid domain mesh in the flexion-extension model—fluid domain mesh (left) and section-view of fluid domain mesh (right).

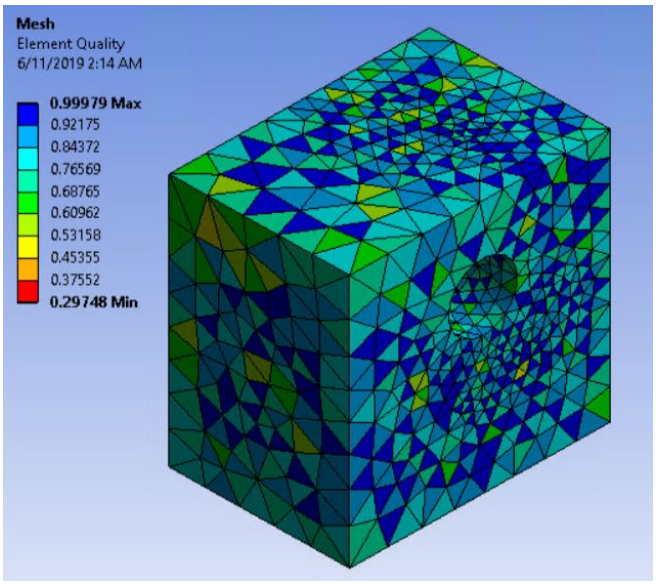

Fig. 32. Fluid domain mesh in the flexion-extension model—element quality.

3.3.2.3 Flexion-extension: Fluent: viscous model: In ANSYS Fluent, the turbulence viscous realizable *k*-*ε* model was chosen to simulate the fluid dynamics of synovial fluid in the elbow joint for flexion-extension. Default values of 1.9 for C2-epsilon, 1 for TKE Prandtl Number, and 1.2 for TDR Prandtl Number were used for the turbulence viscous realizable *k*-*ε* model.

3.3.2.4 Flexion-extension: Fluent: boundary conditions: A velocity inlet boundary condition with an inlet velocity of 0.01 m/s was applied to two faces as shown in Fig. 33 to simulate the secretion of synovial fluid by the synovial membrane. A pressure outlet boundary condition with a gauge pressure of 74,327 Pa was applied to four faces as shown in Fig. 33 to ensure that the operating pressure of the fluid domain was equal to the pressure of synovial fluid in the elbow joint [30]. A wall boundary condition was applied to the cylindrical face as shown in Fig. 34 to simulate the presence of distal humerus articular cartilage.

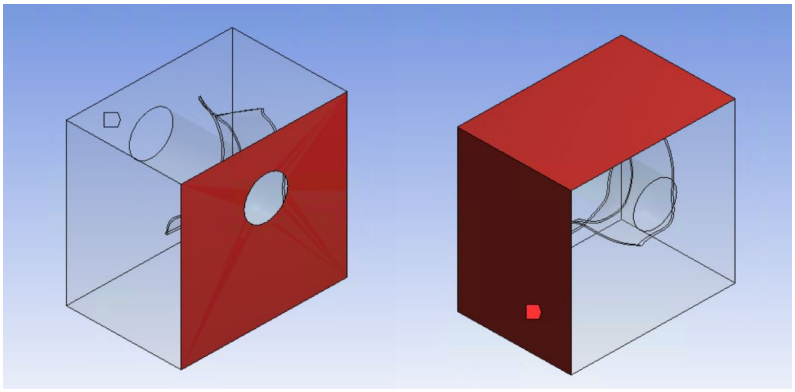

Fig. 33. Boundary conditions in the flexion-extension model—velocity inlet boundary condition was applied to the face highlighted in red as well as the face opposite to the highlighted face (left) and pressure outlet boundary condition was applied to the faces highlighted in red as well as the faces opposite to the highlighted faces (right).

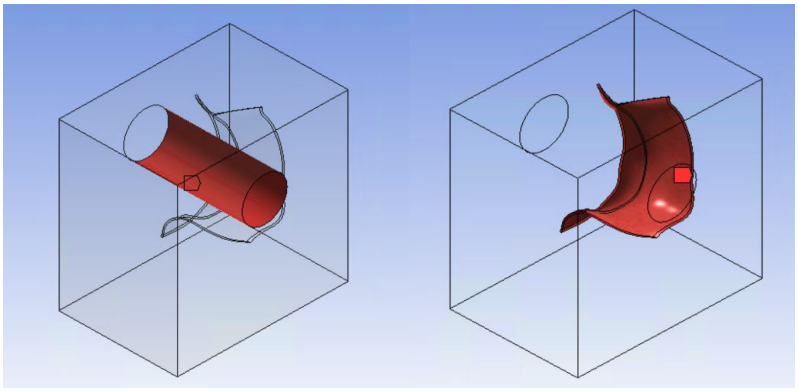

Fig. 34. Boundary conditions in the flexion-extension model—wall (left) and system coupling (right).

3.3.2.5 Flexion-extension: Fluent: dynamic mesh parameters: For any FSI simulation, dynamic mesh parameters are crucial parameters that govern the motion of the fluid domain mesh in coherence with the motion of the structural mesh. In ANSYS Fluent, dynamic mesh settings were applied to the various faces of the fluid domain based on their boundary conditions. Therefore, the faces of the fluid domain pertaining to velocity inlet, pressure outlet, and wall boundary conditions were set to 'stationary,' and the interior of the fluid domain i.e. all the mesh elements inside the synovial fluid enclosure was set to 'deforming'. As shown in Fig. 34, the faces of the proximal ulna articular cartilage cavity inside the synovial fluid domain were set to 'system coupling'. Furthermore, two dynamic mesh update methods—smoothing and remeshing were enabled. The relevant dynamic mesh parameters are shown in Table 11 and Table 12.

Table 11
Flexion-Extension: Dynamic Mesh Properties:
Spring Smoothing Method

Flexion-Extension: Dynamic Mesh Properties: Spring Smoothing Method	
Description	Value
Spring Constant Factor	1
Convergence Tolerance	0.001
Number of Iterations	20
Elements	All
Laplace Node Relaxation	1

Table 12
Flexion-Extension: Dynamic Mesh Properties:
Remeshing Method

Flexion-Extension: Dynamic Mesh Properties: Remeshing Method	
Description	Value
Method	Local Cell
Minimum Length Scale (m)	0.000509
Maximum Length Scale (m)	0.007284
Maximum Cell Skewness	0.79
Size Remeshing Interval	1

3.3.3 Flexion-Extension: System Coupling

While the structural and fluid mechanics of the elbow joint model are simulated by ANSYS Transient Structural and ANSYS Fluent, respectively, FSI inside the elbow joint is possible only when the structural and fluid simulations are synchronized. Thus, ANSYS System Coupling was used to create a coupled simulation between ANSYS Transient Structural and ANSYS Fluent, thereby simulating the interaction of synovial fluid on articular cartilage during flexion and extension of the elbow joint.

Data transfers and time step size are the two main parameters that are defined in System Coupling for any FSI simulation. For flexion and extension FSI simulations, two sets of data transfers were defined. The first data transfer was defined to enable the transfer of structural displacement data of the proximal ulna articular cartilage from Transient Structural to the proximal ulna articular cartilage cavity inside the synovial fluid enclosure in Fluent. This ensures that the movement of the mesh pertaining to the proximal ulna articular cartilage cavity inside the synovial fluid enclosure in Fluent is in coherence with the movement of the proximal ulna articular cartilage geometry in Transient Structural. As the proximal ulna articular cartilage cavity moves inside the fluid enclosure, synovial fluid exerts forces on the proximal ulna articular cartilage cavity. The second data transfer involves the transfer of this fluid force data from Fluent to Transient Structural. Transient Structural processes these fluid forces as loads acting on the proximal ulna articular cartilage geometry, thereby completing the data transfer loop for the FSI simulation.

The size of each coupling time step for flexion and extension FSI simulations was 0.01 s. Each coupling step was allowed a maximum of three iterations to ensure the convergence of data transfers.

3.4 Pronation-Supination Model

This section outlines the specific geometries and parameters that were used to model pronation and supination of the elbow joint in ANSYS Transient Structural, ANSYS Fluent, and ANSYS System Coupling.

3.4.1 Pronation-Supination: Transient Structural

3D geometries of humerus, radius, ulna, distal humerus articular cartilage, proximal ulna articular cartilage, and proximal radius articular cartilage were used to model the structural mechanics of pronation and supination of the elbow joint in ANSYS Transient Structural.

3.4.1.1 Pronation-supination: Transient Structural: joint axis: The pronation-supination joint was modeled as a single DOF proximal radioulnar joint with the joint axis passing between the proximal radial head and the convex articular surface of the ulna at the distal radioulnar joint [14]. Specifically, the pronation-supination was defined as a general ‘body-body’ joint between proximal radius and proximal ulna. Akin to the flexion-extension model, a general joint was used with all degrees of freedom except rotation in z-axis constrained as ANSYS does not allow the user to define non-linear stiffness characteristics for revolute joints. The ability to define the joint with non-linear stiffness characteristics was important to establish the constraint moment generated by elbow pronators and supinators during pronation and supination, respectively.

3.4.1.2 Pronation-supination: Transient Structural: bones: Humerus was constrained to the ground using a fixed ‘body-ground’ joint with rigid contacts enabled as shown in Fig. 35. Ulna was constrained to humerus using a fixed ‘body-body’ joint with rigid contacts enabled as shown in Fig. 35. As discussed in Section 3.4.1.1, radius was constrained to ulna using a general ‘body-body’ joint with rigid contacts enabled and rotation in z-axis as the only active DOF as shown in Fig. 36.

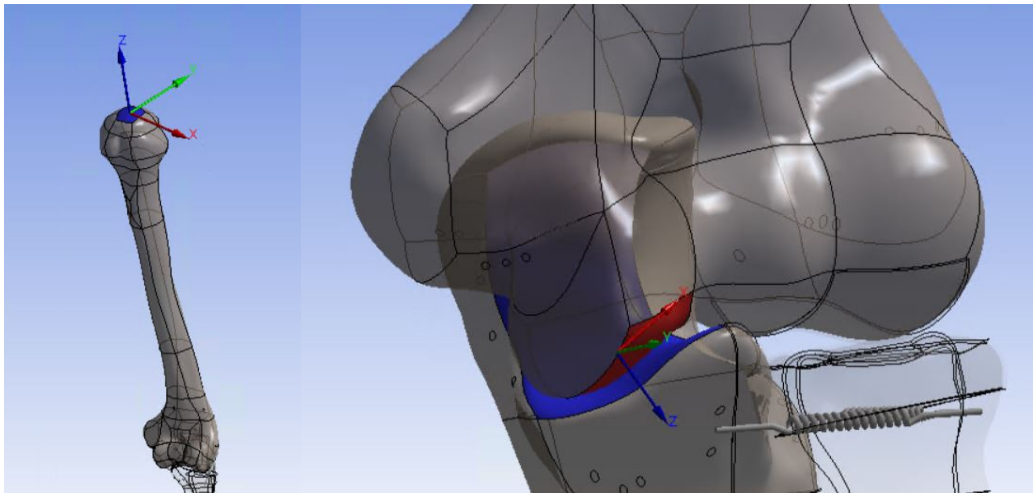

Fig. 35. Bones in the pronation-supination model—distal humerus constrained to ground with a fixed joint (left) and proximal ulna constrained to distal humerus with a fixed joint (right).

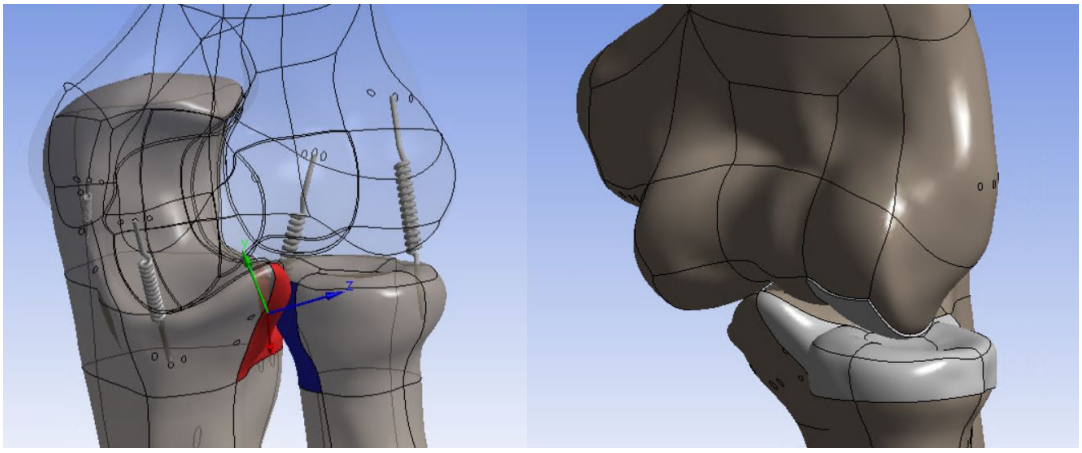

Fig. 36. Pronation-Supination joint in the pronation-supination model—proximal radius constrained to proximal ulna with a general joint (rotation in z-axis is the only active DOF) (left) and isometric view of the elbow joint articulation for the pronation-supination joint model (right).

3.4.1.3 Pronation-supination: Transient Structural: articular cartilage: Articular cartilage geometries were attached to the bones using fixed 'body-body' joints with rigid contacts enabled as shown in Fig. 37 and Fig. 38.

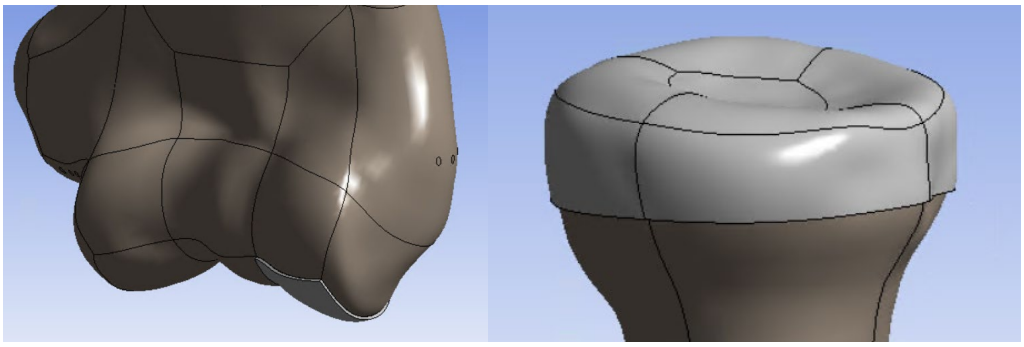

Fig. 37. Articular Cartilage joints in the pronation-supination model—distal humerus articular cartilage constrained to distal humerus (left) and proximal radius articular cartilage constrained to proximal radius (right).

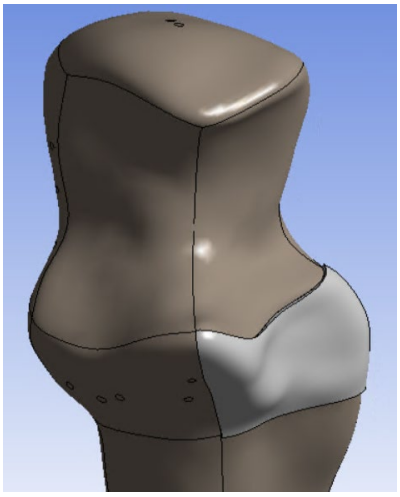

Fig. 38. Articular Caritlage joints in the pronation-supination model—proximal ulna articular cartilage constrained to proximal ulna.

To minimize the computational load of the FSI simulations, only moving cartilage bodies were considered for fluid-structure interfaces. Therefore, humerus, radius, ulna, distal humerus articular cartilage, and proximal ulna articular cartilage were defined as rigid bodies while proximal radius articular cartilage was defined as a flexible body. Thus, the fluid-solid interface boundary condition was applied to all the faces of the proximal radius articular cartilage.

Similar to the flexion-extension model, all the rigid bodies were dimensionally reduced for the purposes of meshing in ANSYS Transient Structural. The only flexible body, proximal radius articular cartilage geometry was meshed in ANSYS using the 'Patch Conforming Method' with tetrahedral elements of size 0.8 mm as shown in Fig. 39. Adaptive mesh sizing and mesh defeaturing with fine resolution settings were enabled. Fig. 39 shows the mesh element quality of proximal radius articular cartilage geometry.

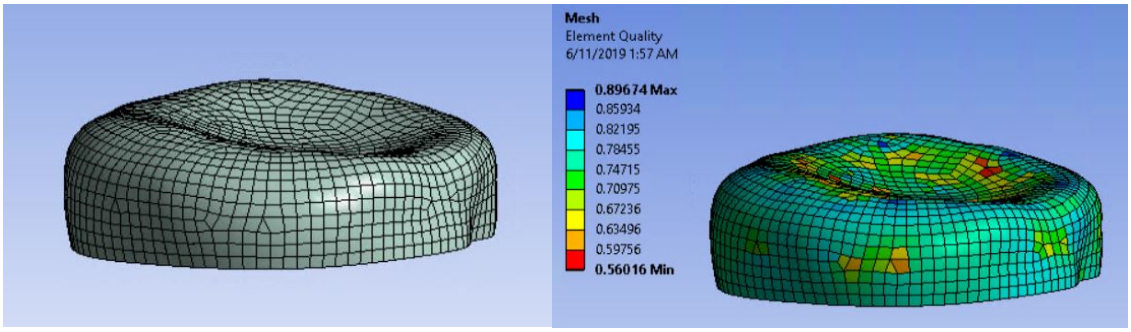

Fig. 39. Articular Cartilage mesh in the pronation-supination model—tetrahedral mesh of proximal radius articular cartilage (left) and mesh element quality of proximal radius articular cartilage (right).

3.4.1.4 Pronation-supination: Transient Structural: ligaments: AL and interosseous membrane were modeled as longitudinal springs inserted between anatomical ligament attachment sites [24] as shown in Fig. 40 and Fig. 41. All relevant parameters for these tension-compression springs were defined as discussed in Section 3.2.3.

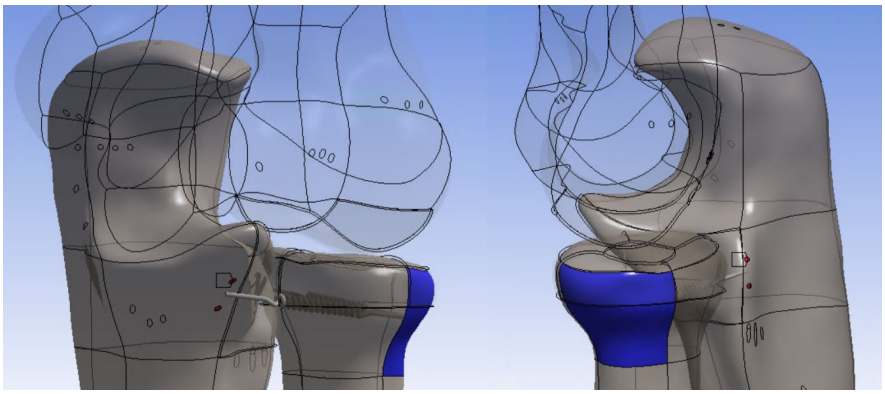

Fig. 40. Ligaments in the pronation-supination model—AL-1 (left) and AL-2 (right).

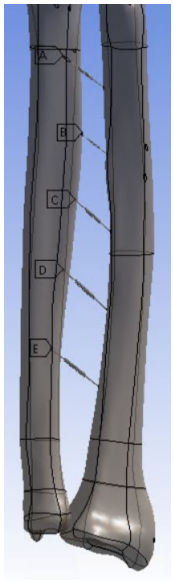

Fig. 41. Ligaments in the pronation-supination model—interosseous membrane.

3.4.1.5 Pronation-supination: Transient Structural: muscles: Non-linear stiffness characteristics were applied to the pronation-supination joint to simulate the stiffness of elbow pronators and supinators for elbow pronation and supination, respectively as discussed in Section 3.2.4.

3.4.1.6 Pronation-supination: Transient Structural: joint loads: Standard earth gravity of 9.8066 m/s^2 was enabled and a rotation joint load was applied to the pronation-supination joint to simulate joint motion. Like the flexion-extension model, simulations were conducted with transient effects disabled since none of the parameters used in the simulation were time-dependent.

Four different FSI simulations were conducted based on the pronation-supination model. All parameters except joint loading conditions and non-linear stiffness parameters of the pronation-supination joint were consistent for all the FSI simulations. The details of joint loading conditions and non-linear stiffness parameters of the pronation-supination

joint for each FSI simulation are shown in Table 13. The graphs for these joint loading conditions are shown in Fig. 42, Fig. 43, Fig. 44, Fig. 45. To simulate elbow supination, a full pronation-supination simulation was conducted with non-linear stiffness parameters pertaining to elbow supinators.

Table 13
Joint Loading Conditions for
Pronation-Supination FSI Simulations

Joint Loading Conditions for Pronation-Supination FSI Simulations		
FSI Simulation Description	Joint Loading Description	Joint Non-Linear Stiffness Conditions
Pronation at 40º/s	See Fig. 42	Elbow Pronators - See Fig. 18
Pronation at 120º/s	See Fig. 43	Elbow Pronators - See Fig. 18
Supination at 40º/s	See Fig. 44	Elbow Supinators - See Fig. 19
Supination at 120º/s	See Fig. 45	Elbow Supinators - See Fig. 19

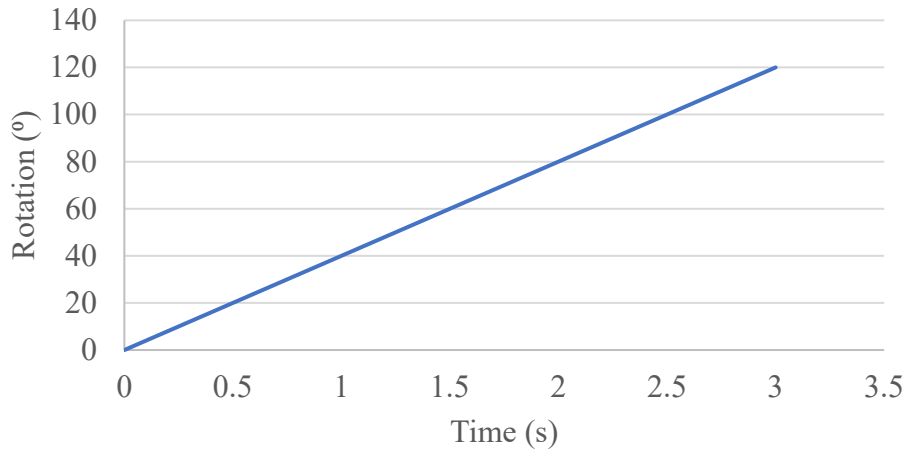

Fig. 42. Joint rotation load for pronation at 40º/s.

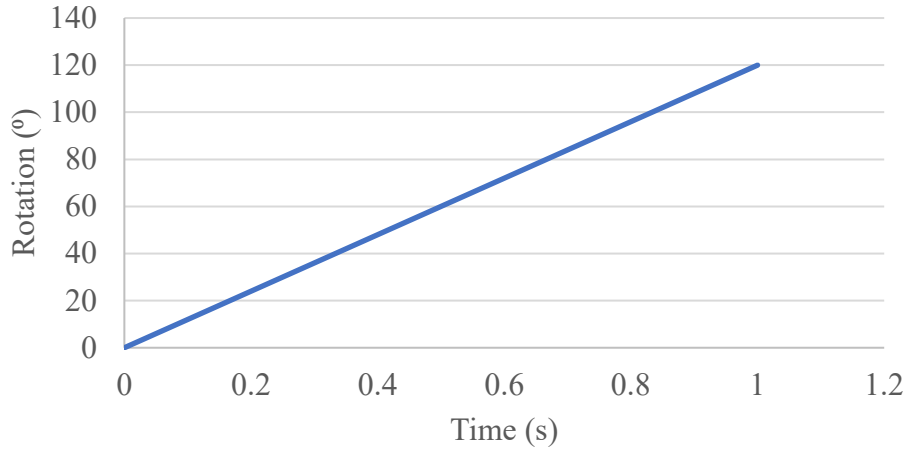

Fig. 43. Joint rotation load for pronation at 120º/s.

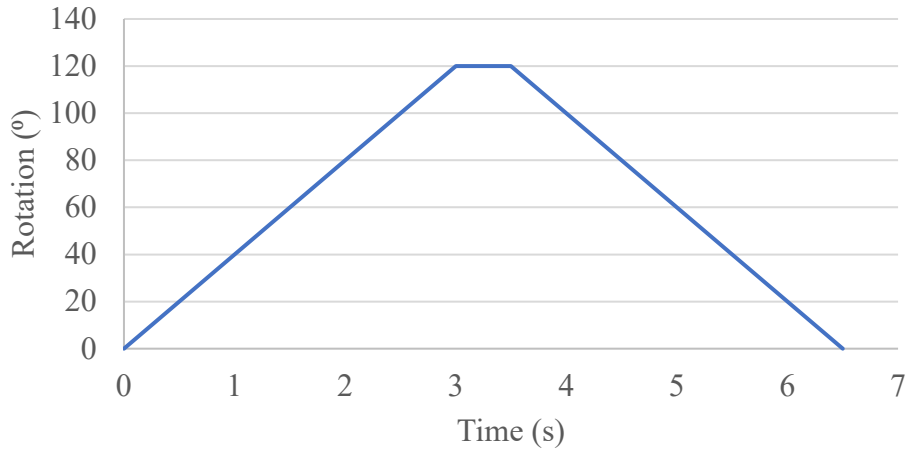

Fig. 44. Joint rotation load for supination at 40º/s.

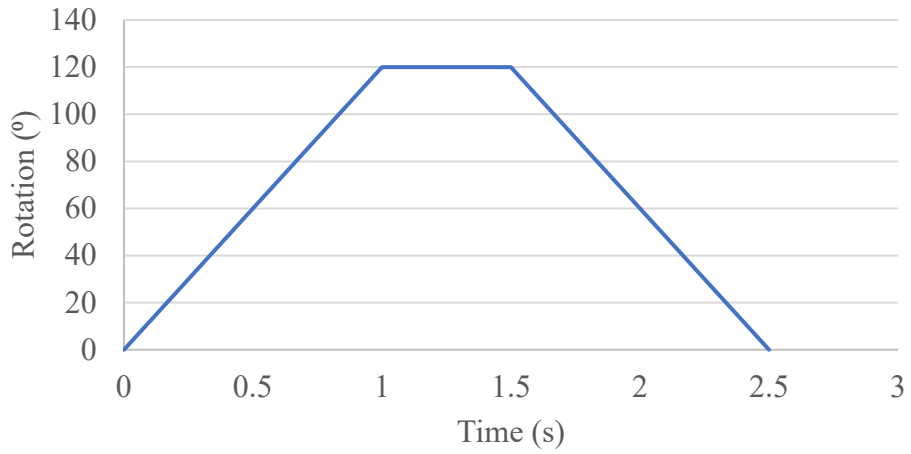

Fig. 45. Joint rotation load for supination at 120º/s.

3.4.2 Pronation-Supination: Fluent

3.4.2.1 Pronation-supination: Fluent: synovial fluid enclosure: As discussed in Section 3.2.6, a synovial fluid enclosure was created around the proximal radius articular cartilage, thereby rendering the proximal radius articular cartilage as a cavity inside the fluid domain. Fig. 46 shows the synovial fluid enclosure with the faces of proximal radius articular cartilage geometry highlighted in red.

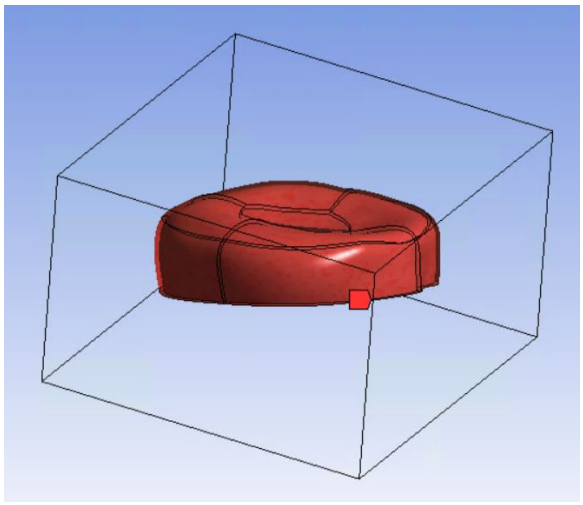

Fig. 46. Proximal radius articular cartilage in the fluid domain (faces highlighted in red).

3.4.2.2 Pronation-supination: Fluent: mesh: The synovial fluid domain for pronation-supination was meshed using the ‘Patching Conforming Method’ with tetrahedral elements of size 0.01 m as shown in Fig. 47. Fig. 47 shows a section view of the fluid domain mesh. The mesh elements that were near the proximal radius articular cartilage cavity were controlled with an element size of 0.001 m. Fig. 48 shows the mesh element quality of the fluid domain geometry.

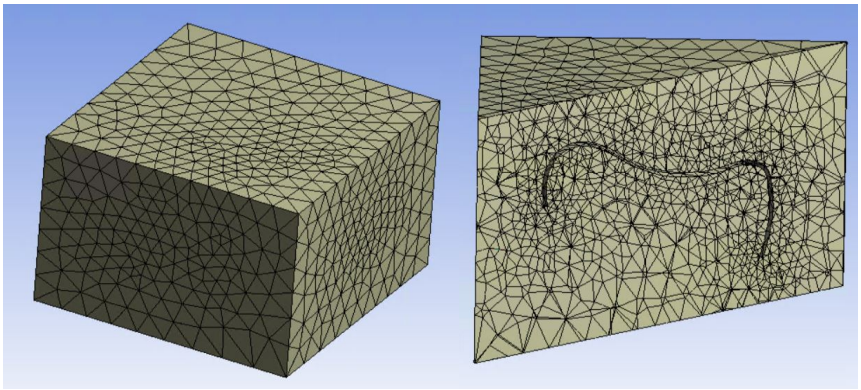

Fig. 47. Fluid domain mesh in the pronation-supination model—fluid domain mesh (left) and section-view of fluid domain mesh (right).

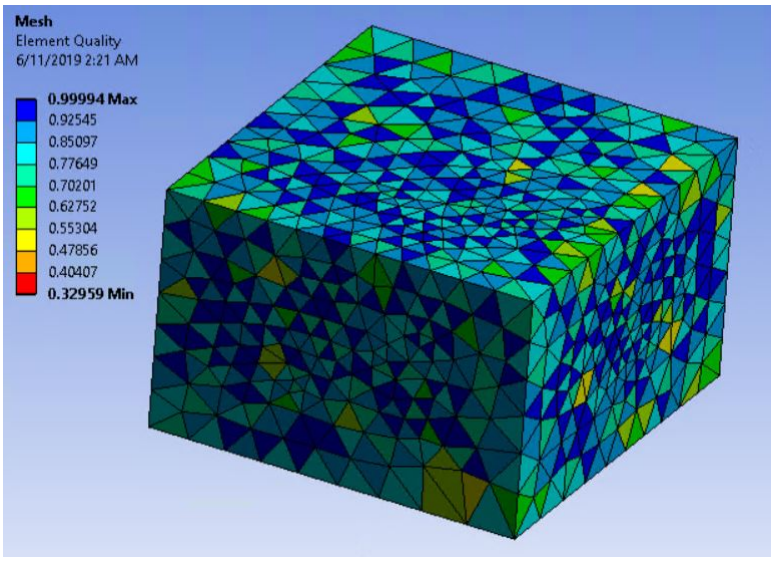

Fig. 48. Fluid domain mesh in the pronation-supination model—element quality.

3.4.2.3 Pronation-supination: Fluent: viscous model: To simulate the fluid dynamics of synovial fluid in the elbow joint for pronation-supination, the turbulence viscous realizable k-ε model was chosen. Similar to the flexion-extension model, default values of 1.9 for C2-epsilon, 1 for TKE Prandtl Number, and 1.2 for TDR Prandtl Number were used for the turbulence viscous realizable k-ε model.

3.4.2.4 Pronation-supination: Fluent: boundary conditions: A velocity inlet boundary condition with an inlet velocity of 0.01 m/s was applied to one face as shown in Fig. 49 to simulate the secretion of synovial fluid by the synovial membrane. A pressure outlet boundary condition with a gauge pressure of 74,327 Pa was applied to one face as shown in Fig. 49 to ensure that the operating pressure of the fluid domain was equal to the pressure of synovial fluid in the elbow joint [30]. A wall boundary condition was applied to four faces as shown in Fig. 50 to simulate the presence of distal humerus articular cartilage and proximal ulna articular cartilage.

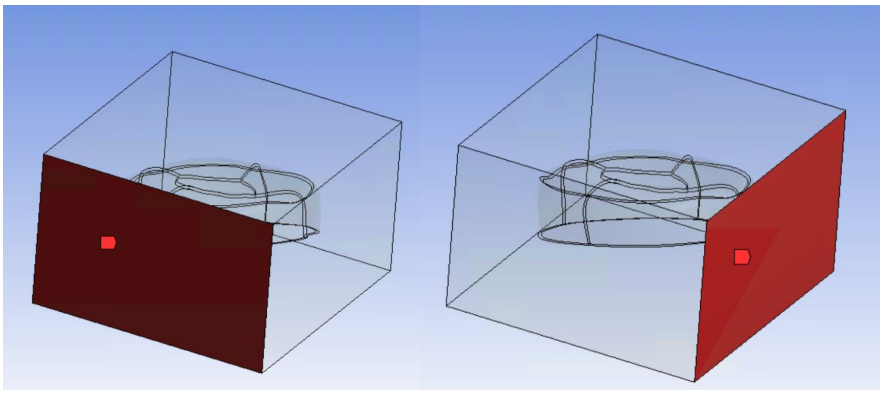

Fig. 49. Boundary conditions in the pronation-supination model—velocity inlet (left) and pressure outlet (right).

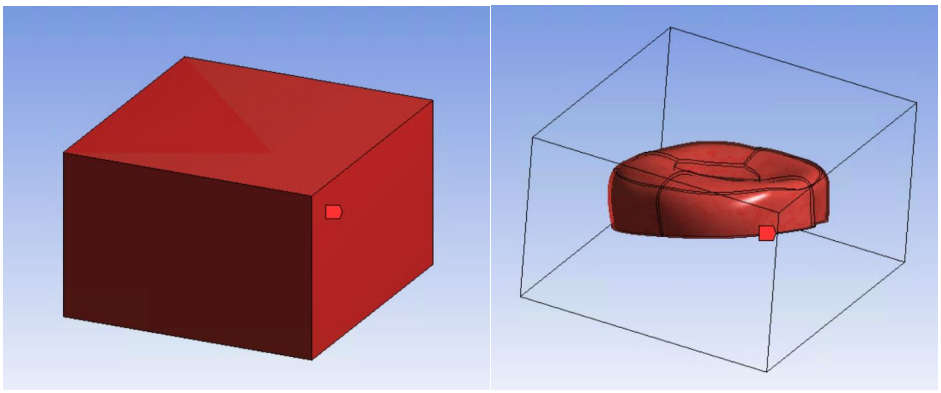

Fig. 50. Boundary conditions in the pronation-supination model—wall boundary condition was applied to the three faces highlighted in red as well as bottom face (not shown in the figure) (left) and system coupling (right).

3.4.2.5 Pronation-supination: Fluent: dynamic mesh parameters: Like the flexion-extension model, dynamic mesh settings were applied to the various faces of the fluid domain based on their boundary conditions. Therefore, the faces of the fluid domain pertaining to velocity inlet, pressure outlet, and wall boundary conditions were set to 'stationary,' and the interior of the fluid domain i.e. all the elements inside the synovial fluid enclosure was set to 'deforming'. As shown in Fig. 50, the faces of the proximal radius articular cartilage cavity inside the fluid domain were set to 'system coupling'. Furthermore, two dynamic mesh update methods – smoothing and remeshing were enabled. The relevant dynamic mesh parameters are shown in Table 14 and Table 15.

Table 14
Pronation-Supination: Dynamic Mesh Properties:
Spring Smoothing Method

Pronation-Supination: Dynamic Mesh Properties: Spring Smoothing Method	
Description	Value
Spring Constant Factor	1
Convergence Tolerance	0.001
Number of Iterations	20
Elements	All
Laplace Node Relaxation	1

Table 15
Pronation-Supination: Dynamic Mesh Properties:
Remeshing Method

Pronation-Supination: Dynamic Mesh Properties: Remeshing Method	
Description	Value
Method	Local Cell
Minimum Length Scale (m)	0.000525
Maximum Length Scale (m)	0.004409
Maximum Cell Skewness	0.79
Size Remeshing Interval	1

3.4.3 Pronation-Supination: System Coupling

Like the flexion-extension model, ANSYS System Coupling was used to create a coupled simulation between ANSYS Transient Structural and ANSYS Fluent to simulate the interaction of synovial fluid on articular cartilage during pronation and supination motion of the elbow joint.

Again, akin to the flexion-extension model, two sets of data transfers were defined. The first data transfer was defined to enable the transfer of structural displacement data of the proximal radius articular cartilage from Transient Structural to the proximal radius articular cartilage cavity inside the synovial fluid enclosure in Fluent. This ensures that the movement of the mesh pertaining to the proximal radius articular cartilage cavity inside the synovial fluid enclosure in Fluent is in coherence with the movement of the proximal radius articular cartilage geometry in Transient Structural. As the proximal radius articular cartilage cavity moves inside the fluid enclosure, synovial fluid exerts forces on the proximal radius articular cartilage cavity. The second data transfer governs the transfer of this fluid force data from Fluent to Transient Structural. Transient Structural processes these fluid forces as loads acting on the proximal radius articular cartilage, thereby completing the data transfer loop for the FSI simulation.

The size of each coupling time step for pronation and supination FSI simulations was 0.01 s. Each coupling step was allowed a maximum of three iterations to ensure the convergence of data transfers.

3.5 Model Validation

To validate the elbow joint model, the simulation-derived relationship between constraint moment, elastic moment and relative joint rotation for flexion, extension, pronation, and supination was compared to the published data pertaining to elbow moment generated by elbow flexors, extensors, supinators, and pronators during flexion, extension, pronation, and supination, respectively [29].

4 RESULTS

This section presents the results of the eight FSI simulations conducted using the computational elbow joint model developed during this thesis study. The computation details of each FSI simulation are shown in Table 16. Fig. 51, Fig. 52, Fig. 53, and Fig. 54 show the various stages of elbow joint motion during flexion, extension, pronation, and supination, respectively.

Table 16
Computation Details of FSI Simulations

Computation Details of FSI Simulations		
FSI Simulation Description	Computation Time	Computing Power Specifications
Flexion at 20º/s	4 h 17 m	16 cores of Intel(R) Xeon(R) CPU E5-2620 v4 in parallel at 2.10 GHz
Flexion at 120º/s	55 m 27 s	
Extension at 20º/s	8 h 24 m	
Extension at 120º/s	2 h 4 m	
Pronation at 40º/s	2 h 13 m	
Pronation at 120º/s	47 m 19 s	
Supination at 40º/s	4 h 2 m	
Supination at 120º/s	1 h 37 m	

Fig. 51. Elbow flexion snapshots from flexion FSI simulations.

Fig. 52. Elbow extension snapshots from extension FSI simulations.

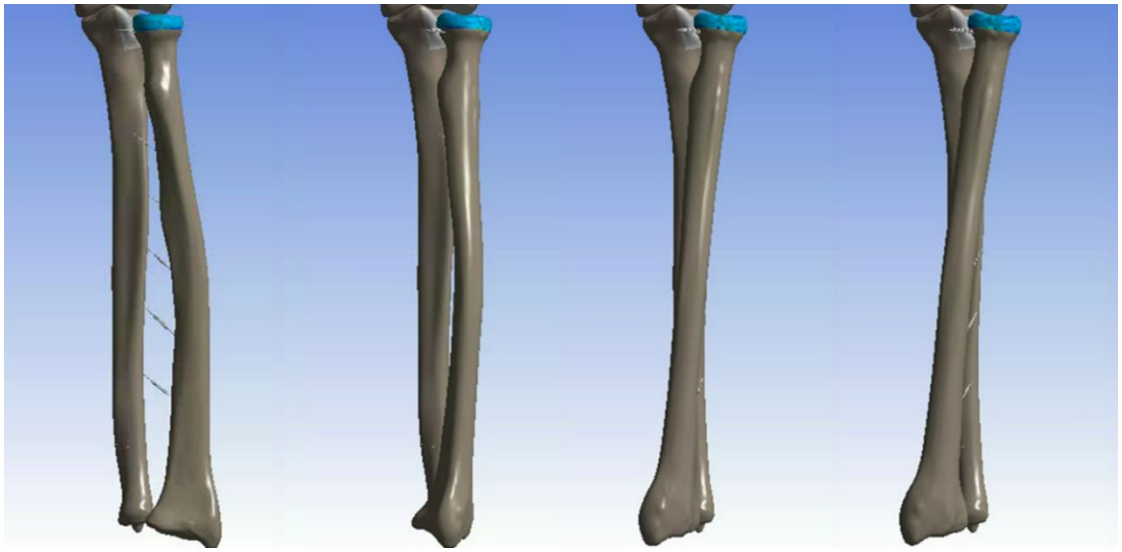

Fig. 53. Elbow pronation snapshots from pronation FSI simulations.

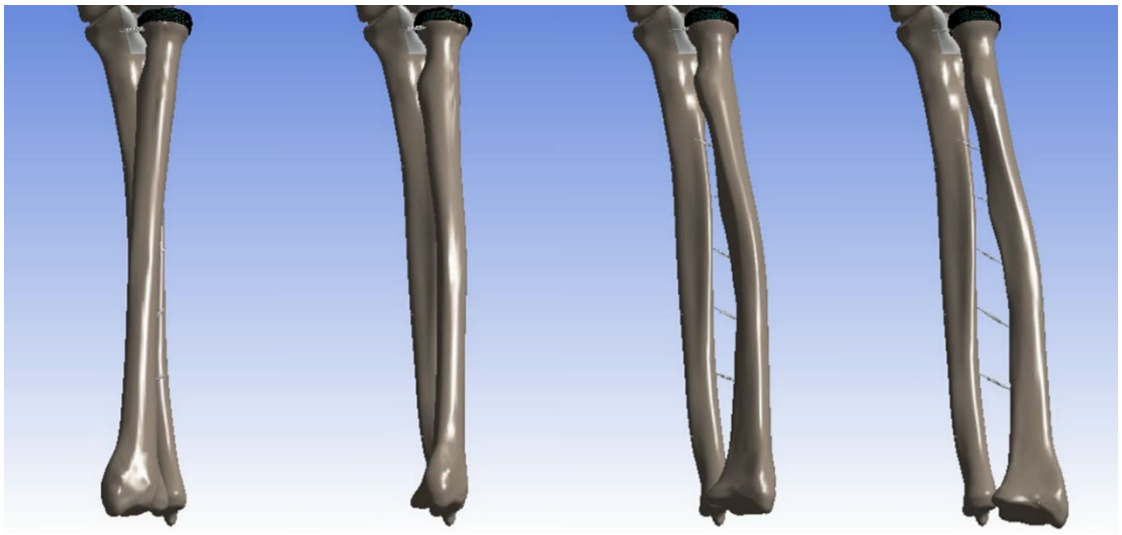

Fig. 54. Elbow supination snapshots from supination FSI simulations.

4.1 Flexion at 20º/s

Fig. 55 shows the relationship between constraint moment generated by elbow flexors and ligaments, elastic moment generated by elbow flexor stiffness, and total moment generated at the elbow joint during elbow flexion from 0º to 120º at a joint velocity of 20º/s. Comparing the constraint moment and elastic moment curves in Fig. 55 with the elbow flexors moment curve (bold, black curve labeled as 'model') in Fig. 15, shows that the elbow joint model developed in this FSI simulation correlates well with the published elbow joint model [29].

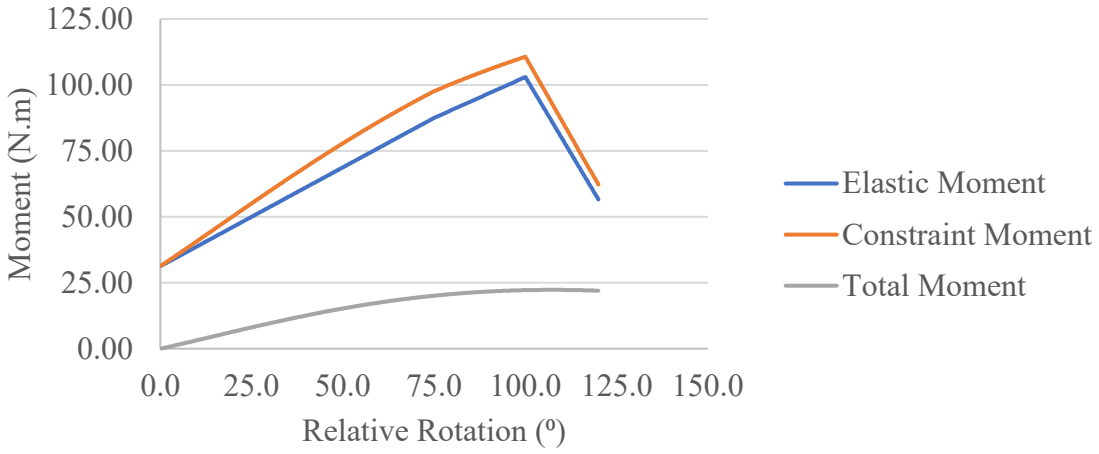

Fig. 55. Joint moment vs. rotation data—elbow flexion at 20º/s.

Fig. 56 provides the ligament load data with respect to elbow flexion angle during elbow flexion from 0º to 120º at a joint velocity of 20º/s. Peak loads of 865.72 N, 115.65 N, 542.15 N, and 527.63 N were observed for LUCL, RCL, MCL-Anterior, and MCL-Posterior, respectively.

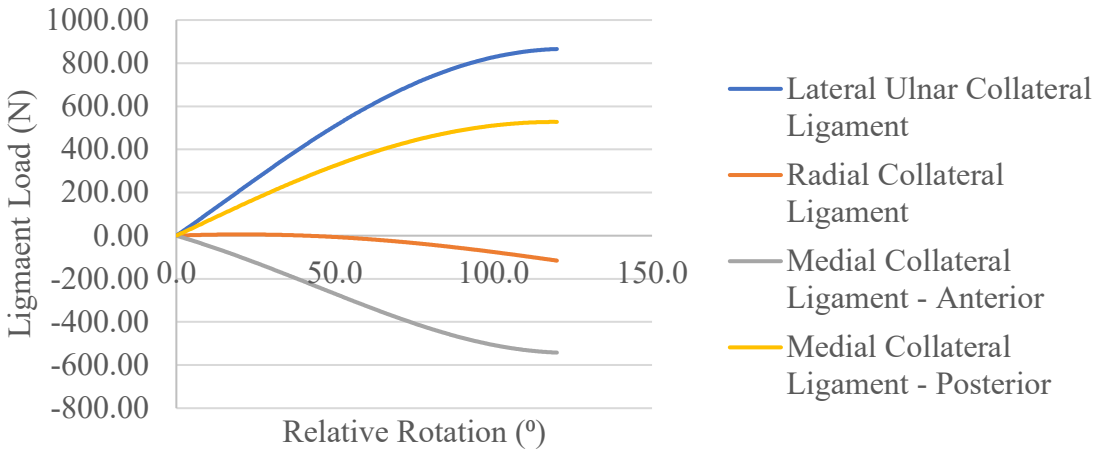

Fig. 56. Ligament load data—elbow flexion at 20º/s.

Fig. 57 and Fig. 58 show the relationship between the peak von Mises stress and peak maximum shear stress acting on the proximal ulna articular cartilage due to the forces exerted by synovial fluid with respect to flexion angle during elbow flexion from 0º to 120º at a joint velocity of 20º/s. Peak von Mises stress of 72,606 Pa or 0.0073 MPa, and peak maximum shear stress of 41,909 Pa or 0.0042 MPa were recorded to be acting on proximal ulna articular cartilage.

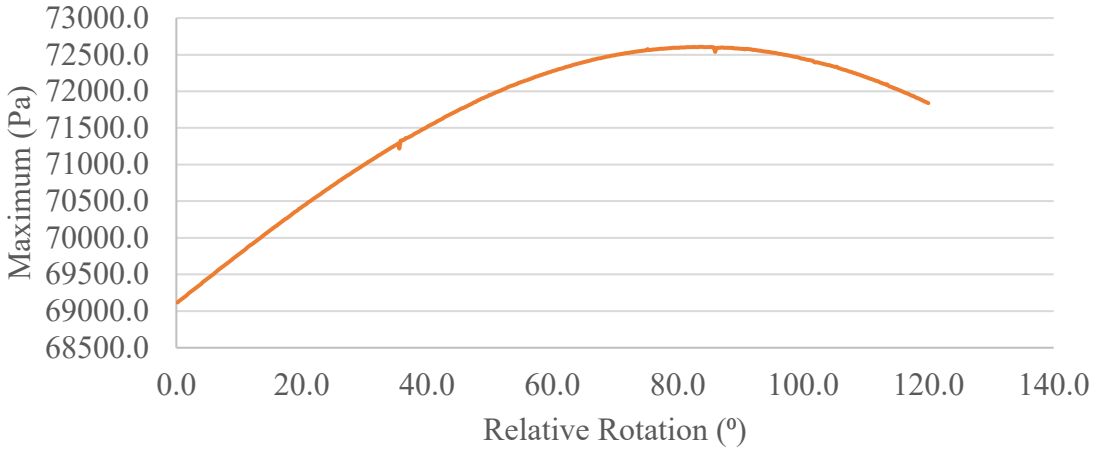

Fig. 57. Peak von Mises stress data on proximal ulna articular cartilage—elbow flexion at 20º/s.

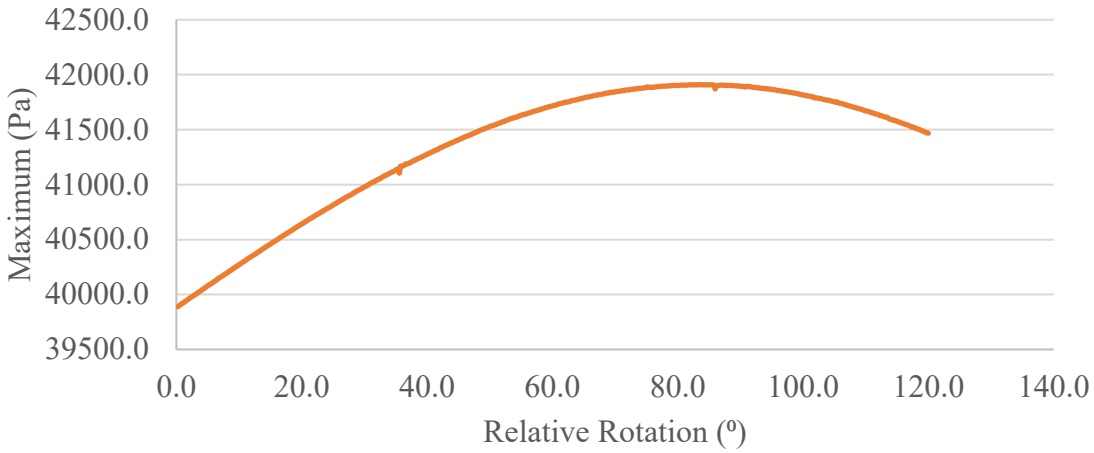

Fig. 58. Peak maximum shear stress data on proximal ulna articular cartilage—elbow flexion at 20º/s.

Fig. 59 and Fig. 60 show the contour plots of von Mises stress and maximum shear stress acting on the proximal ulna articular cartilage due to the forces exerted by synovial fluid during elbow flexion from 0º to 120º at a joint velocity of 20º/s.

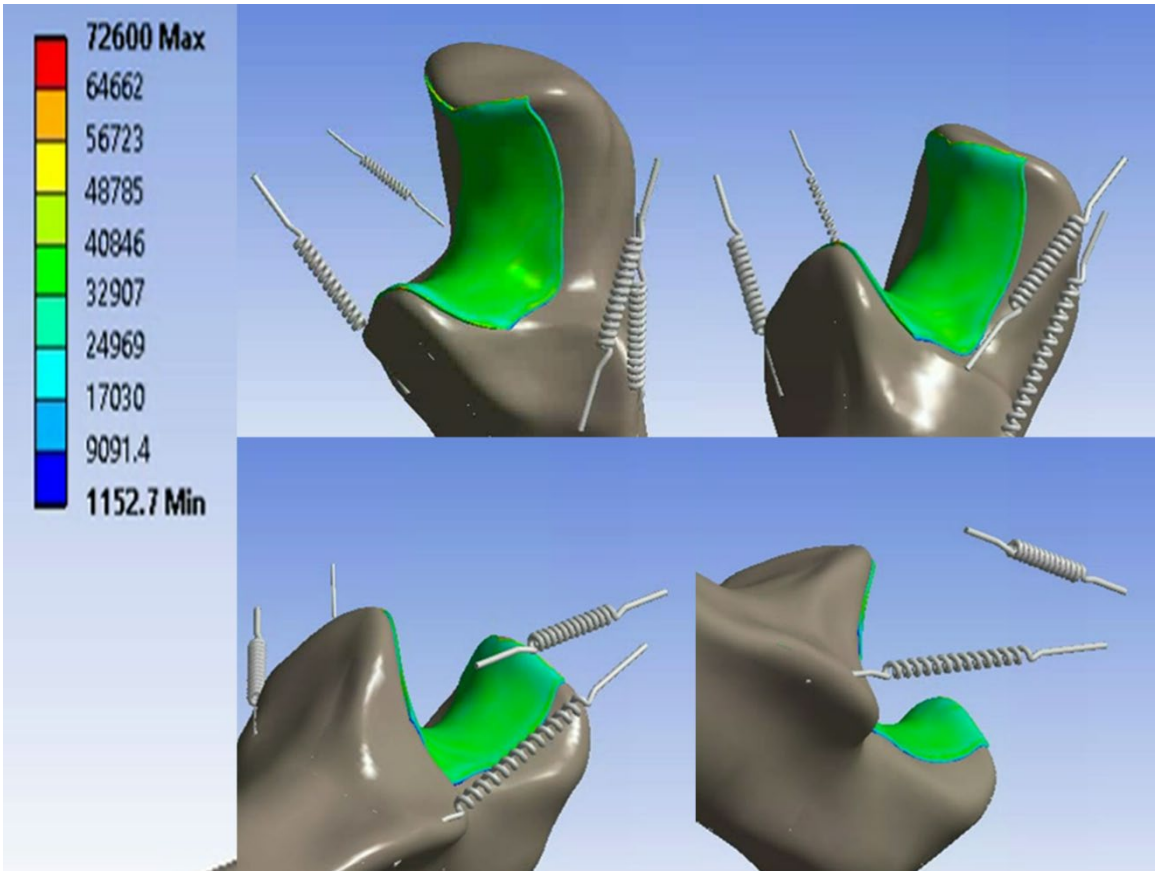

Fig. 59. Contour plot of von Mises stress on proximal ulna articular cartilage—elbow flexion at 20º/s. The scale in the figure is represented in Pascals. The motion is starting from the top-left corner in the clockwise-direction and the snapshots were taken at approximately equidistant time intervals.

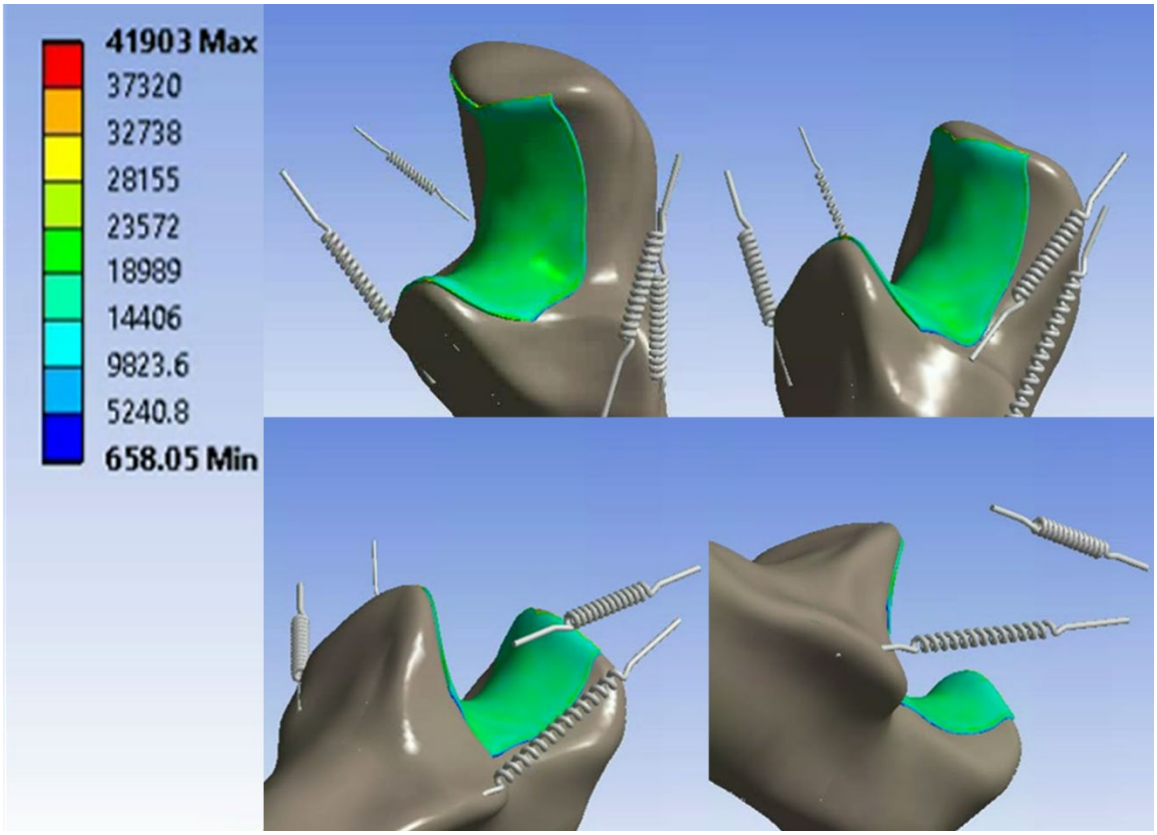

Fig. 60. Contour plot of maximum shear stress on proximal ulna articular cartilage—elbow flexion at 20º/s. The scale in the figure is represented in Pascals. The motion is starting from the top-left corner in the clockwise-direction and the snapshots were taken at approximately equidistant time intervals.

Fig. 61 and Fig. 62 show the velocity streamlines of synovial fluid velocity near proximal ulna articular cartilage during elbow flexion from 0º to 120º at a joint velocity of 20º/s in isometric and side views, respectively. Maximum synovial fluid velocity of 0.002 m/s was recorded.

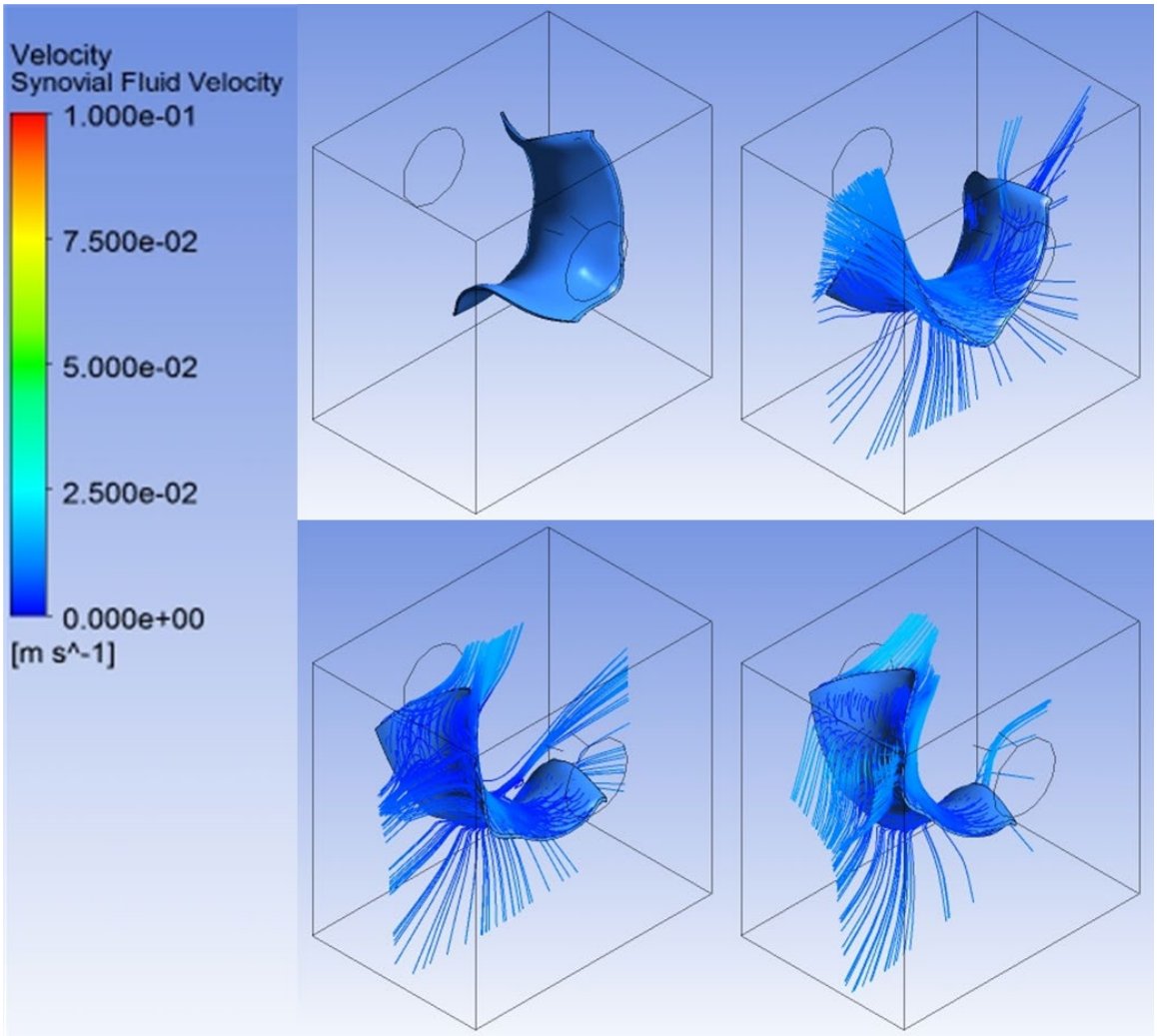

Fig. 61. Velocity streamlines of synovial fluid—elbow flexion at 20º/s (isometric view). The motion is starting from the top-left corner in the clockwise-direction and the snapshots were taken at approximately equidistant time intervals.

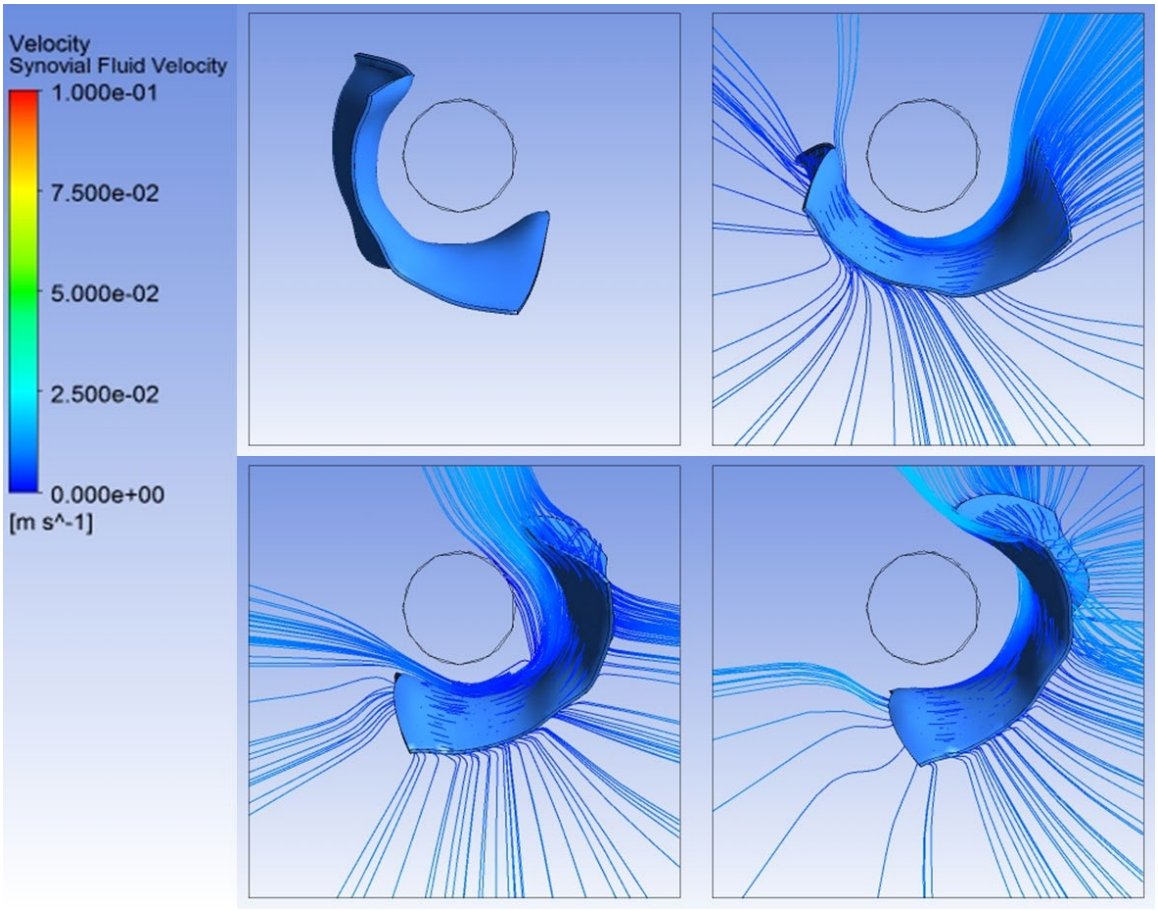

Fig. 62. Velocity streamlines of synovial fluid—elbow flexion at 20º/s (side view). The motion is starting from the top-left corner in the clockwise-direction and the snapshots were taken at approximately equidistant time intervals.

Fig. 63 shows that the mass-flow rate of synovial fluid at velocity inlet and pressure outlet is conserved during the full range of elbow flexion from 0º to 120º at a joint velocity of 20º/s.

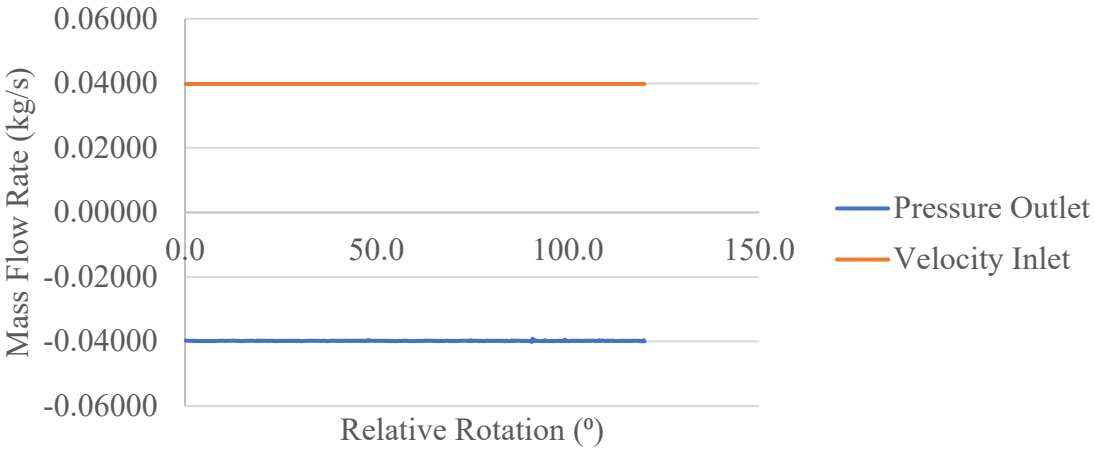

Fig. 63. Synovial fluid mass flow rate data—elbow flexion at 20º/s.

Fig. 64 shows the root mean square (RMS) change of data transfer of the structural displacement of proximal ulna articular cartilage between ANSYS Transient Structural and ANSYS Fluent during the FSI simulation of elbow flexion from 0º to 120º at a joint velocity of 20º/s.

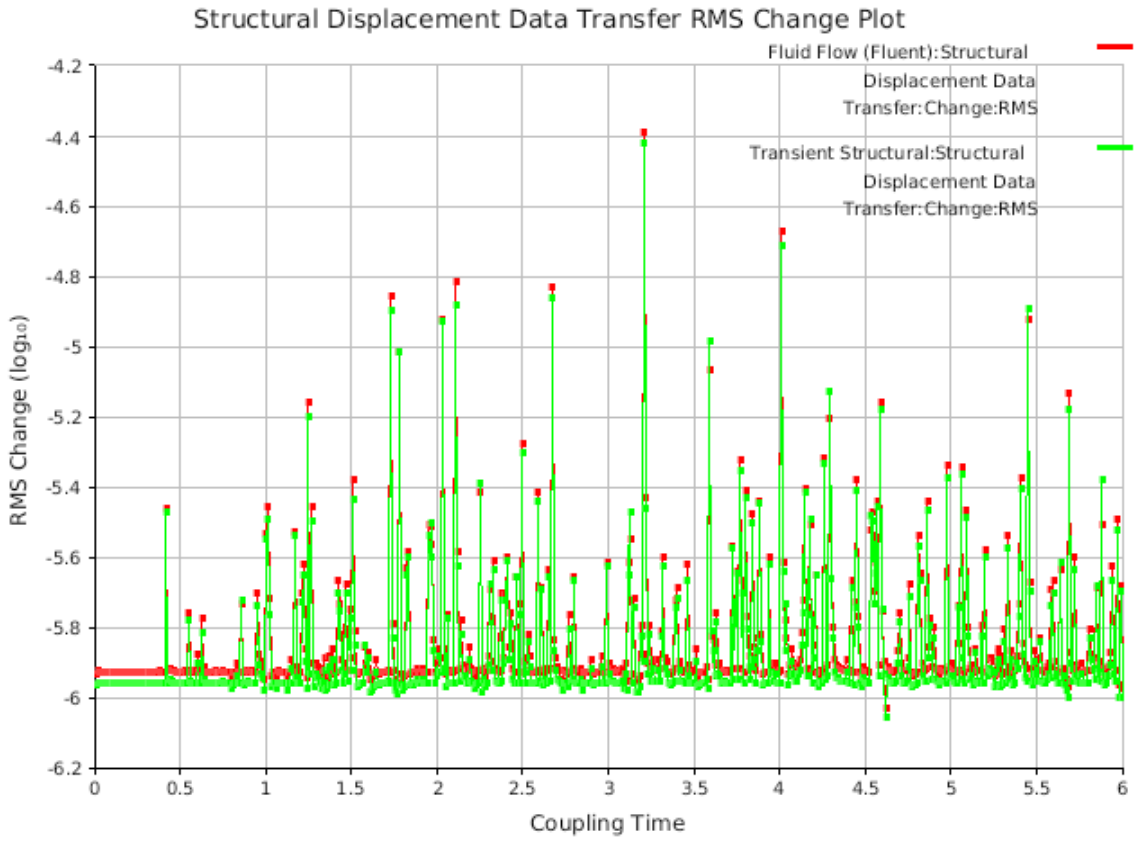

Fig. 64. Structural displacement data transfer RMS change plot—elbow flexion at 20º/s.

Fig. 65 shows the RMS change of data transfer of the synovial fluid forces acting on proximal ulna articular cartilage between ANSYS Transient Structural and ANSYS Fluent during the FSI simulation of elbow flexion from 0º to 120º at a joint velocity of 20º/s.

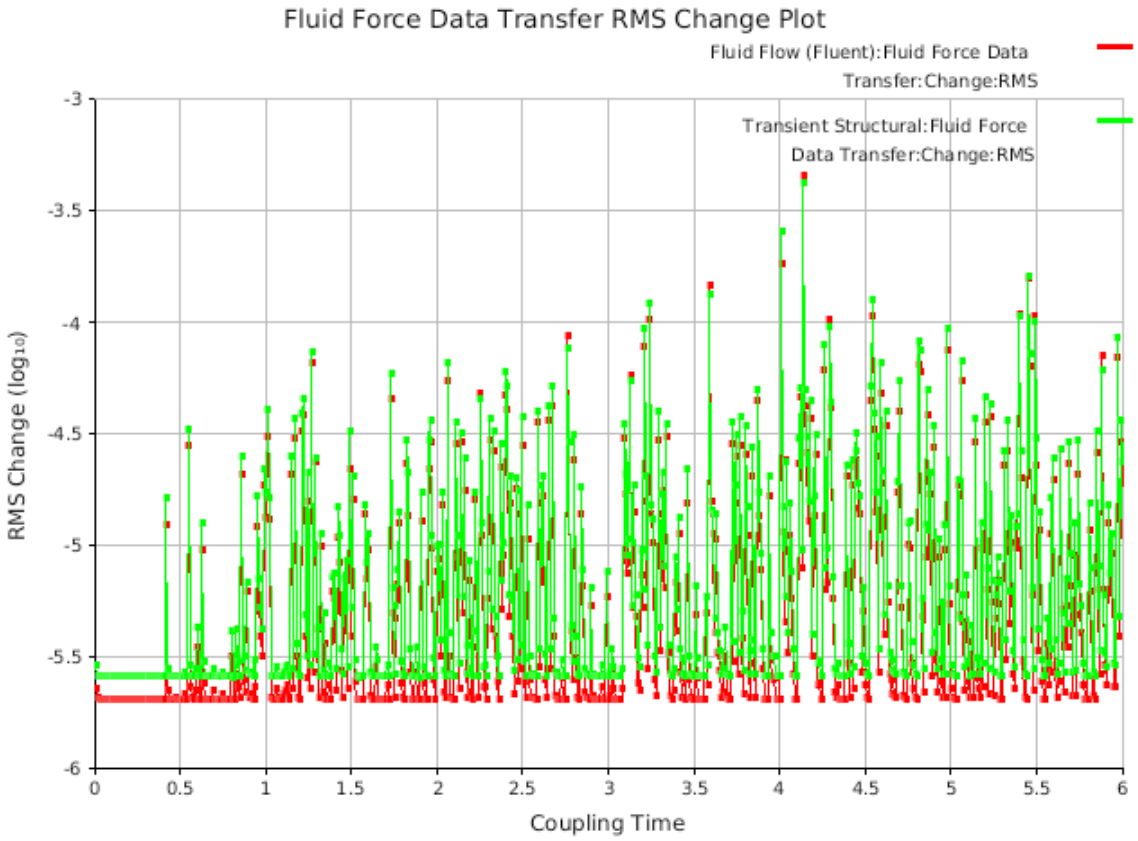

Fig. 65. Fluid force data transfer RMS change plot—elbow flexion at 20º/s.

4.2 Flexion at 120º/s

Fig. 66 shows the relationship between constraint moment generated by elbow flexors and ligaments, elastic moment generated by elbow flexor stiffness, and total moment generated at the elbow joint during elbow flexion from 0º to 120º at a joint velocity of 120º/s. Comparing the constraint moment and elastic moment curves in Fig. 66 with the elbow flexors moment curve (bold, black curve labeled as 'model') in Fig. 15, shows that the elbow joint model developed in this FSI simulation correlates well with the published elbow joint model [29].

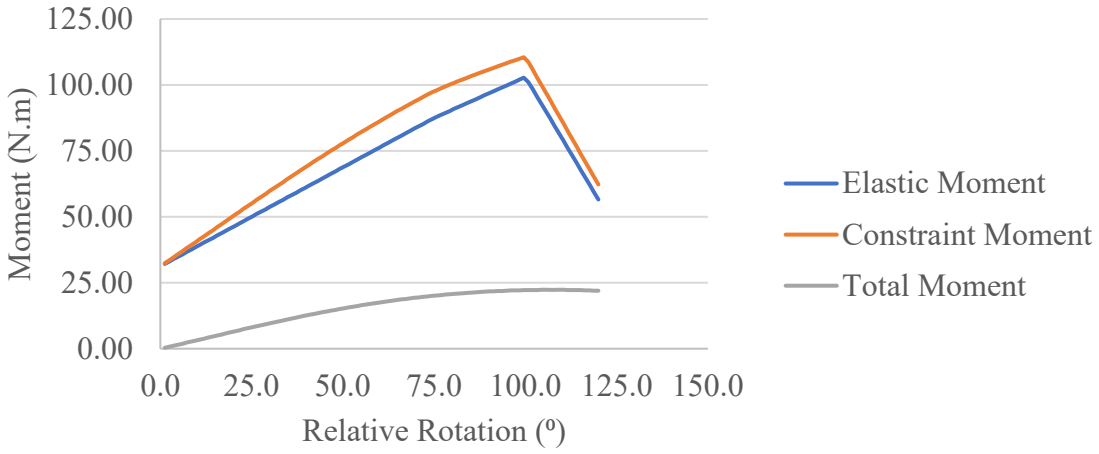

Fig. 66. Joint moment vs. rotation data—elbow flexion at 120º/s.

Fig. 67 provides the ligament load data with respect to elbow flexion angle during elbow flexion from 0º to 120º at a joint velocity of 120º/s. Peak loads of 865.72 N, 115.65 N, 542.15 N, and 527.63 N were observed for LUCL, RCL, MCL-Anterior, and MCL-Posterior, respectively.

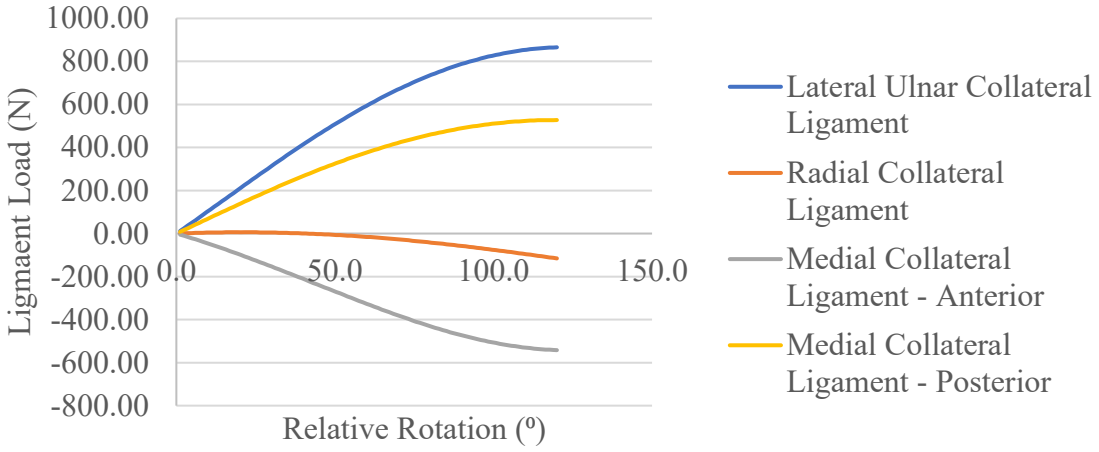

Fig. 67. Ligament load data—elbow flexion at 120º/s.

Fig. 68 and Fig. 69 show the relationship between the peak von Mises stress and peak maximum shear stress acting on the proximal ulna articular cartilage due to the forces exerted by synovial fluid with respect to flexion angle during elbow flexion from 0º to 120º at a joint velocity of 120º/s. Peak von Mises stress of 72,771 Pa or 0.0073 MPa, and peak maximum shear stress of 42,004 Pa or 0.0042 MPa were recorded to be acting on proximal ulna articular cartilage.

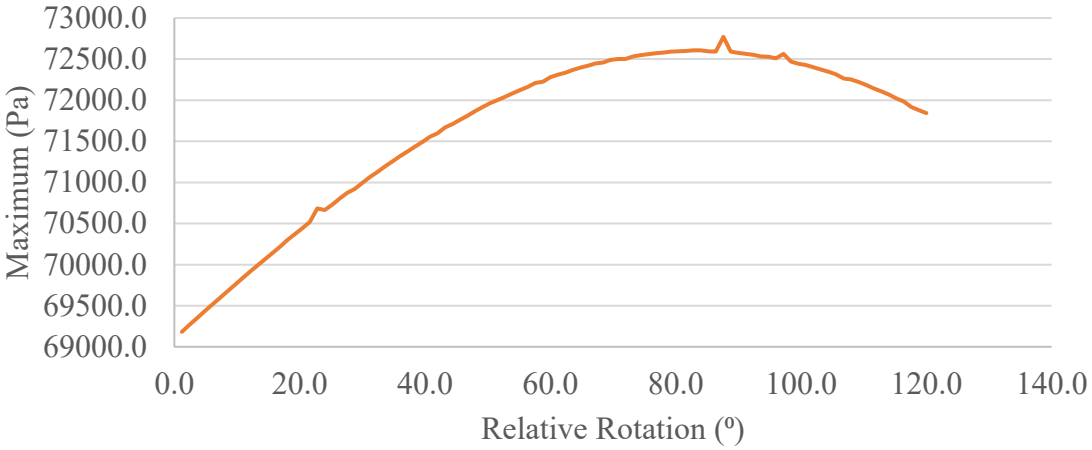

Fig. 68. Peak von Mises stress data on proximal ulna articular cartilage—elbow flexion at 120º/s.

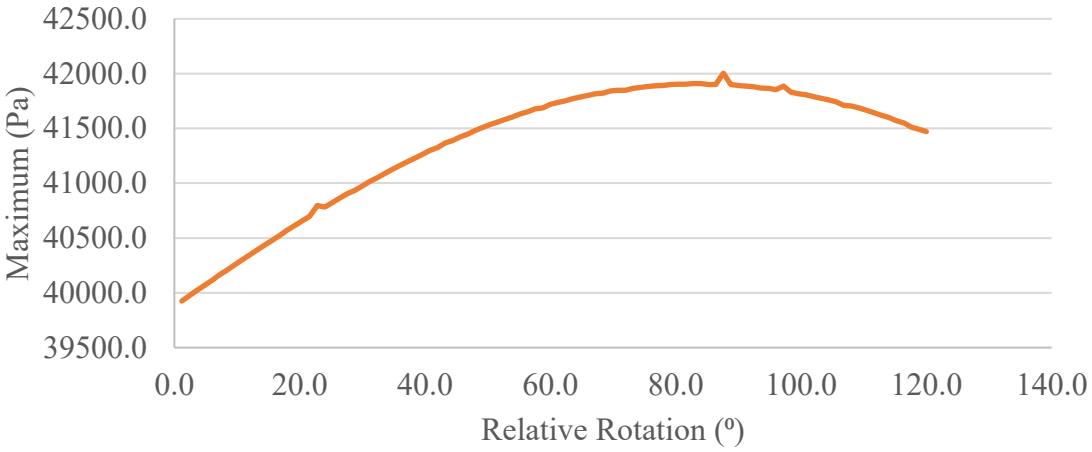

Fig. 69. Peak maximum shear stress data on proximal ulna articular cartilage—elbow flexion at 120º/s.

Fig. 70 and Fig. 71 show the contour plots of von Mises stress and maximum shear stress acting on the proximal ulna articular cartilage due to synovial fluid forces during elbow flexion from 0º to 120º at a joint velocity of 120º/s.

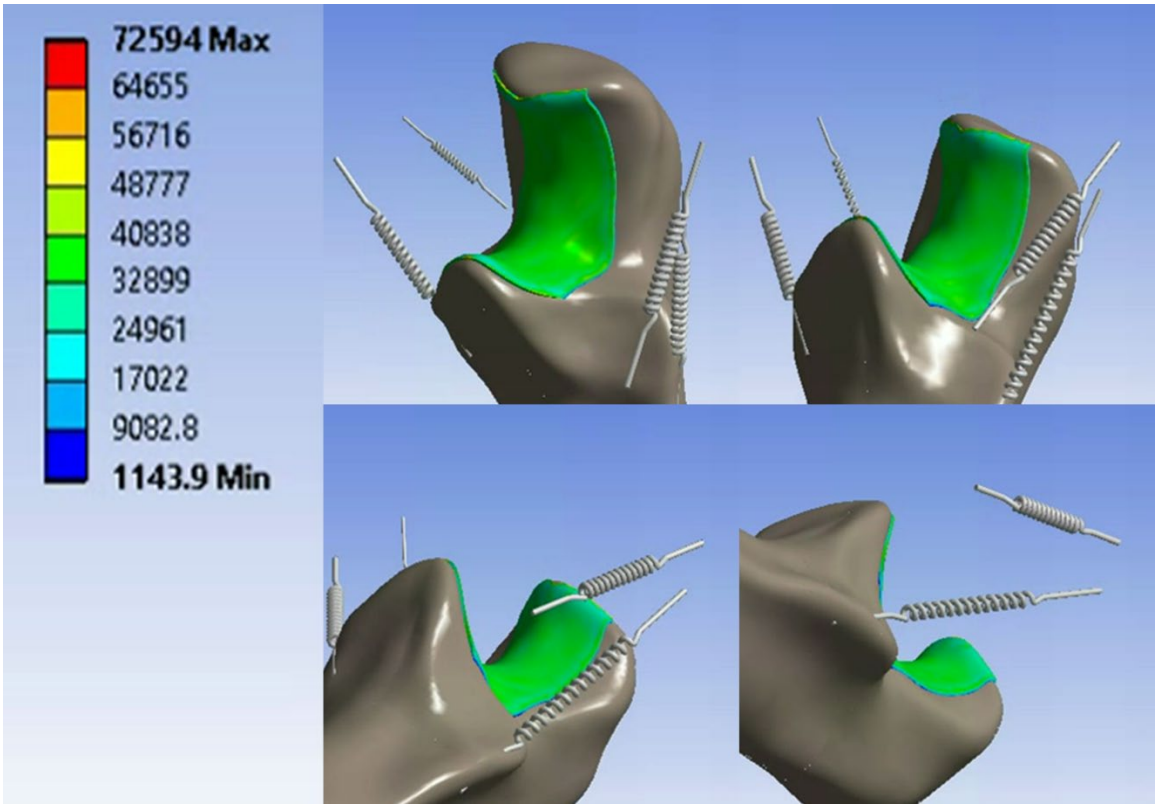

Fig. 70. Contour plot of von Mises stress on proximal ulna articular cartilage—elbow flexion at 120º/s. The scale in the figure is represented in Pascals. The motion is starting from the top-left corner in the clockwise-direction and the snapshots were taken at approximately equidistant time intervals.

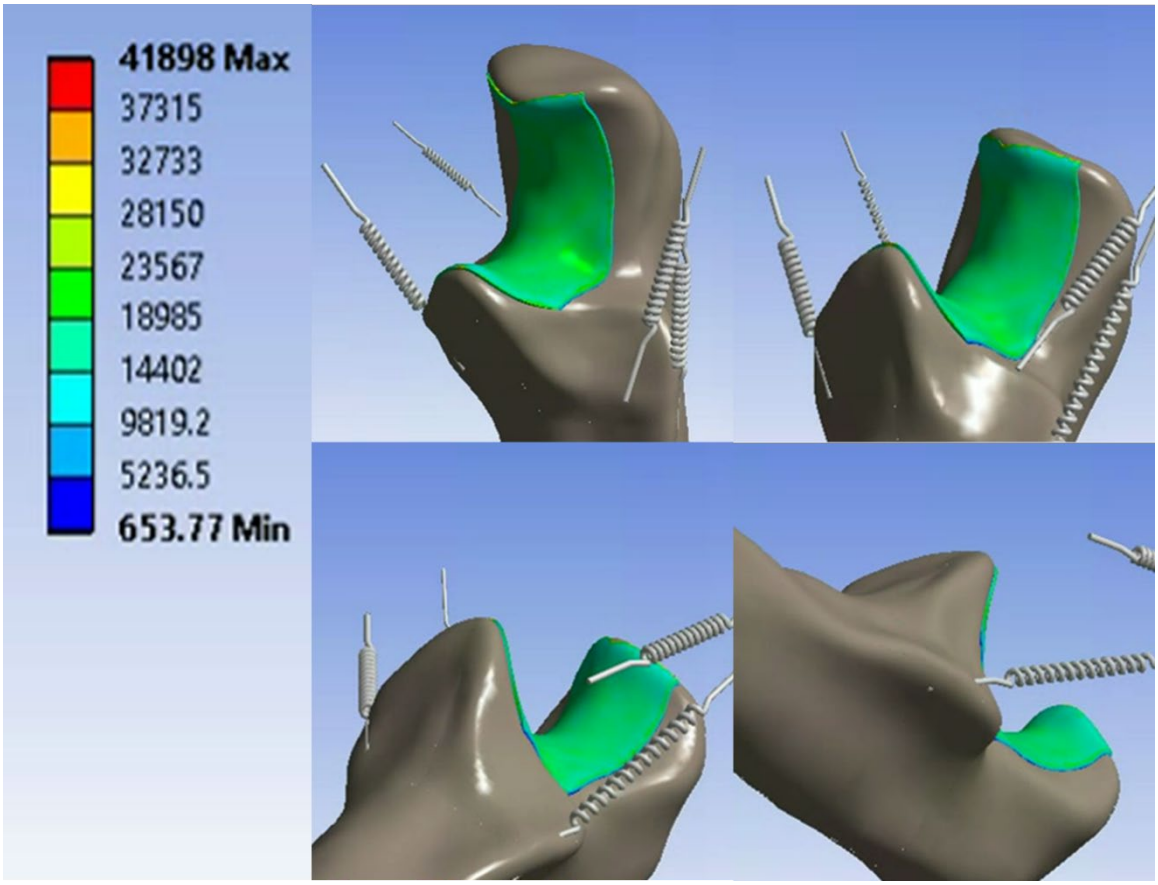

Fig. 71. Contour plot of maximum shear stress on proximal ulna articular cartilage—elbow flexion at 120º/s. The scale in the figure is represented in Pascals. The motion is starting from the top-left corner in the clockwise-direction and the snapshots were taken at approximately equidistant time intervals.

Fig. 72 and Fig. 73 show the velocity streamlines of synovial fluid velocity near proximal ulna articular cartilage during elbow flexion from 0º to 120º at a joint velocity of 120º/s in isometric and side views, respectively. Maximum synovial fluid velocity of 0.01 m/s was recorded.

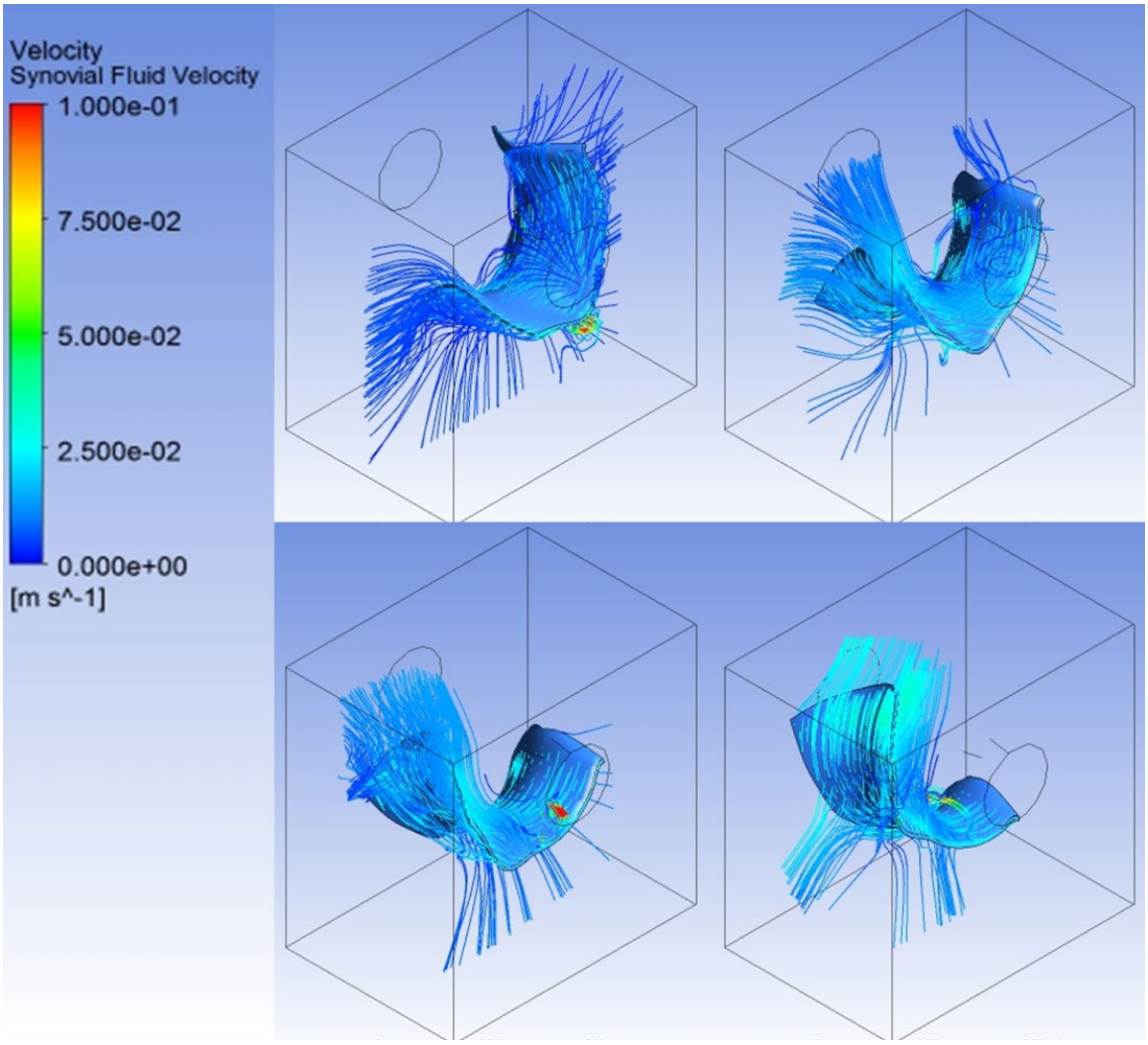

Fig. 72. Velocity streamlines of synovial fluid—elbow flexion at 120º/s (isometric view). The motion is starting from the top-left corner in the clockwise-direction and the snapshots were taken at approximately equidistant time intervals.

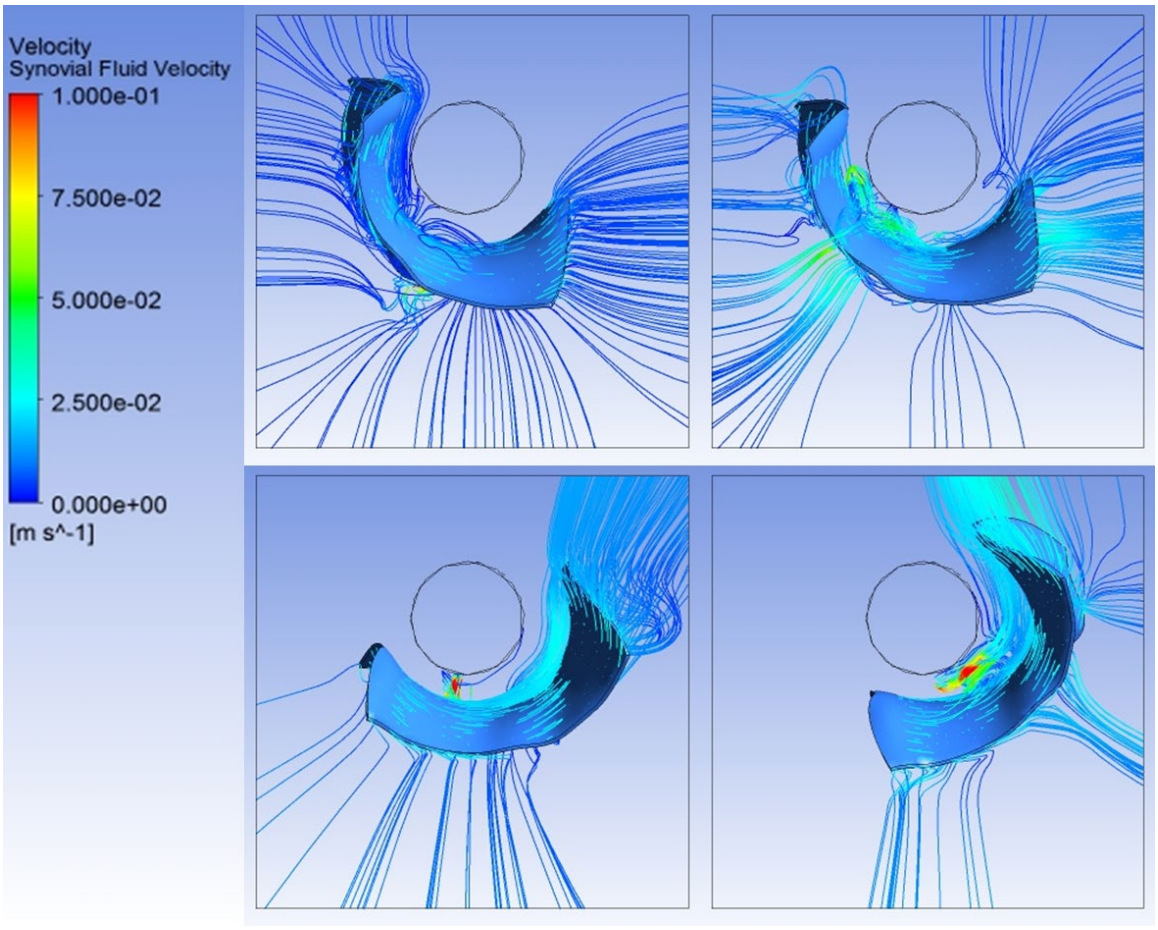

Fig. 73. Velocity streamlines of synovial fluid—elbow flexion at 120º/s (side view). The motion is starting from the top-left corner in the clockwise-direction and the snapshots were taken at approximately equidistant time intervals.

Fig. 74 shows that the mass-flow rate of synovial fluid at velocity inlet and pressure outlet is conserved during the full range of elbow flexion from 0º to 120º at a joint velocity of 120º/s.

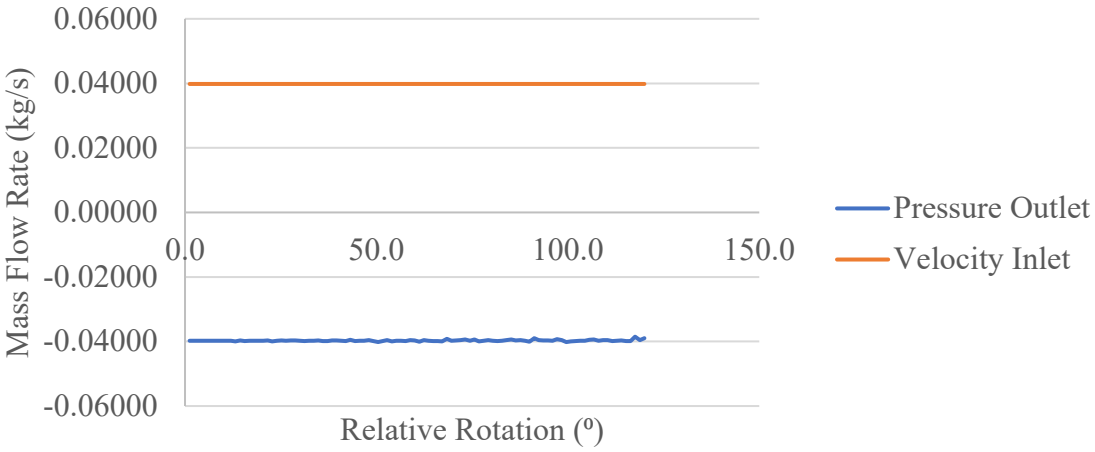

Fig. 74. Synovial fluid mass flow rate data—elbow flexion at 120º/s.

Fig. 75 shows the RMS change of data transfer of the structural displacement of proximal ulna articular cartilage between ANSYS Transient Structural and ANSYS Fluent during the FSI simulation of elbow flexion from 0º to 120º at a joint velocity of 120º/s.

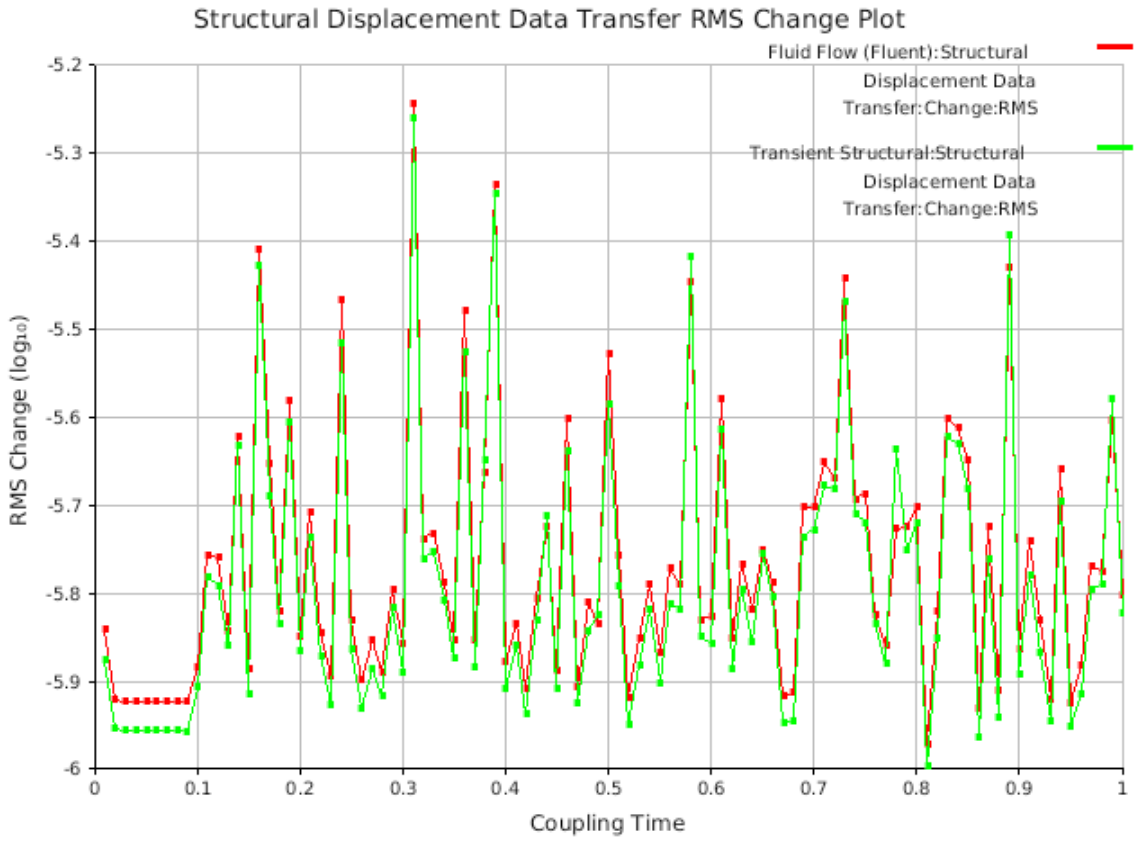

Fig. 75. Structural displacement data transfer RMS change plot—elbow flexion at 120º/s.

Fig. 76 shows the RMS change of data transfer of the synovial fluid forces acting on proximal ulna articular cartilage between ANSYS Transient Structural and ANSYS Fluent during the FSI simulation of elbow flexion from 0º to 120º at a joint velocity of 120º/s.

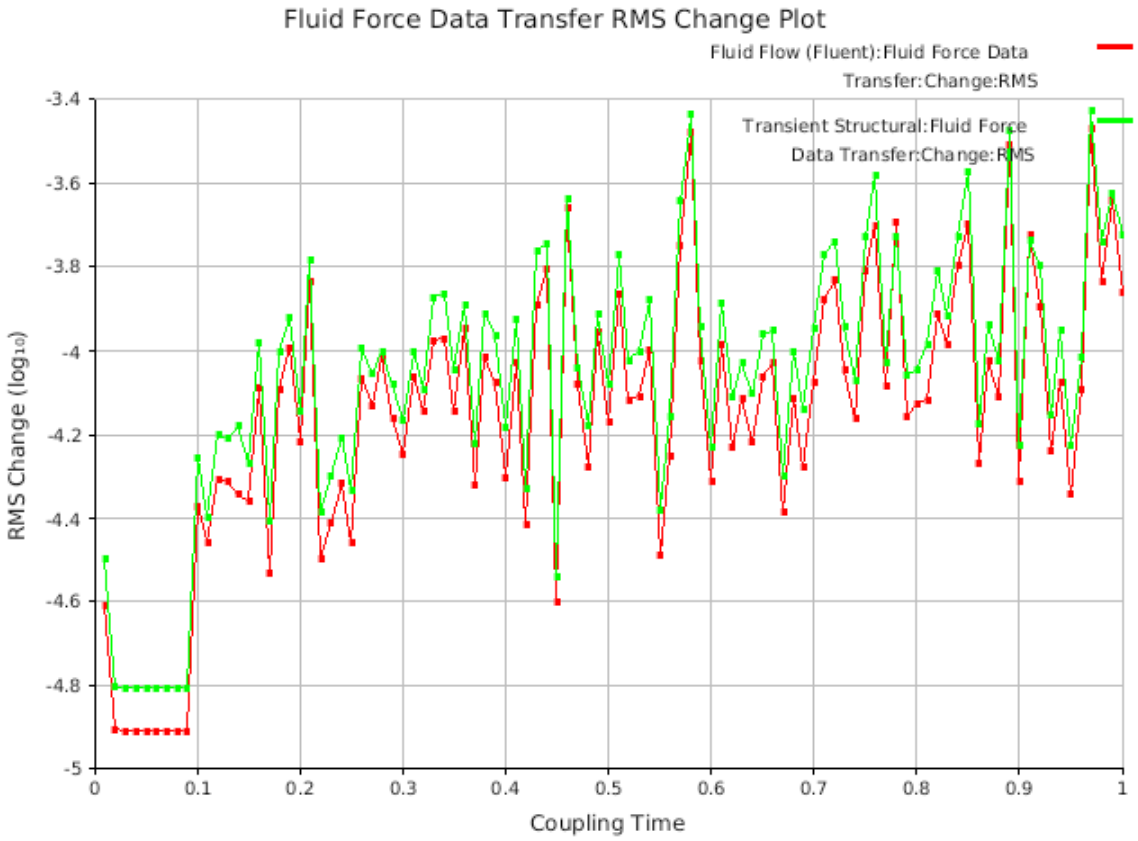

Fig. 76. Fluid force data transfer RMS change plot—elbow flexion at 120º/s.

4.3 Summary of Flexion Data

The computational elbow joint model for elbow flexion correlates well with the published elbow joint model [29] for both 20º/s and 120º/s joint velocity conditions.

For both 20º/s and 120º/s elbow flexion conditions, peak loads of 865.72 N, 115.65 N, 542.15 N, and 527.63 N were determined for LUCL, RCL, MCL-Anterior, and MCL-Posterior, respectively.

The peak von Mises stress and peak maximum shear stress acting on the proximal ulna articular cartilage was determined to be 0.0073 MPa and 0.0042 MPa, respectively for both 20º/s and 120º/s elbow flexion conditions.

During the slower 20º/s elbow flexion, synovial fluid flow was predominantly laminar with a maximum velocity of 0.002 m/s. However, during the faster, 120º/s elbow flexion, synovial fluid flow exhibited turbulence with a maximum velocity of 0.01 m/s which is equal to the inlet velocity of the fluid domain.

4.4 Extension at 20º/s

Fig. 77 shows the relationship between constraint moment generated by elbow extensors and ligaments, elastic moment generated by elbow extensors stiffness, and total moment generated at the elbow joint during elbow extension from 120º to 0º at a joint velocity of 20º/s. Comparing the constraint moment and elastic moment curves in Fig. 77 with the elbow extensors moment curve (bold, black curve labeled as 'model') in Fig. 15, shows that the elbow joint model developed in this FSI simulation correlates well with the published elbow joint model [29].

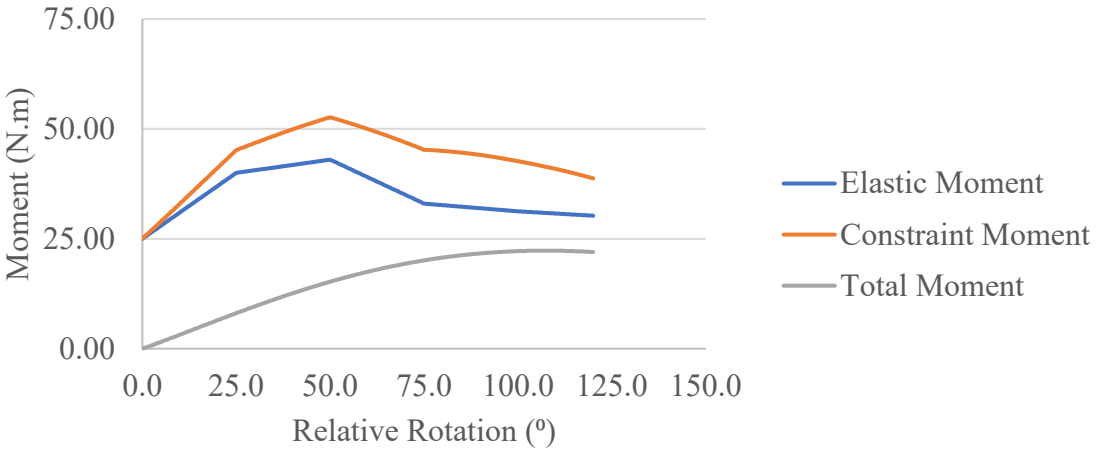

Fig. 77. Joint moment vs. rotation data—elbow extension at 20º/s.

Fig. 78 provides the ligament load data with respect to elbow extension angle during elbow extension from 120º to 0º at a joint velocity of 20º/s. Peak loads of 865.72 N, 115.65 N, 542.15 N, and 527.63 N were observed for LUCL, RCL, MCL-Anterior, and MCL-Posterior, respectively.

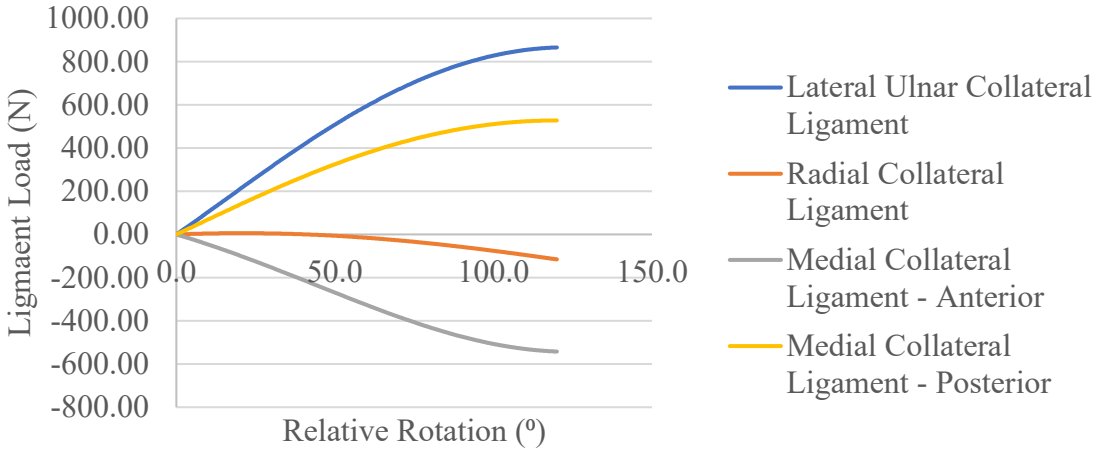

Fig. 78. Ligament load data—elbow extension at 20º/s.

Fig. 79 and Fig. 80 show the relationship between the peak von Mises stress and peak maximum shear stress acting on the proximal ulna articular cartilage due to the forces exerted by synovial fluid with respect to extension angle during elbow extension from 120º to 0º at a joint velocity of 20º/s. Peak von Mises stress of 72,610 Pa or 0.0073 MPa, and peak maximum shear stress of 41,911 Pa or 0.0042 MPa were recorded to be acting on proximal ulna articular cartilage.

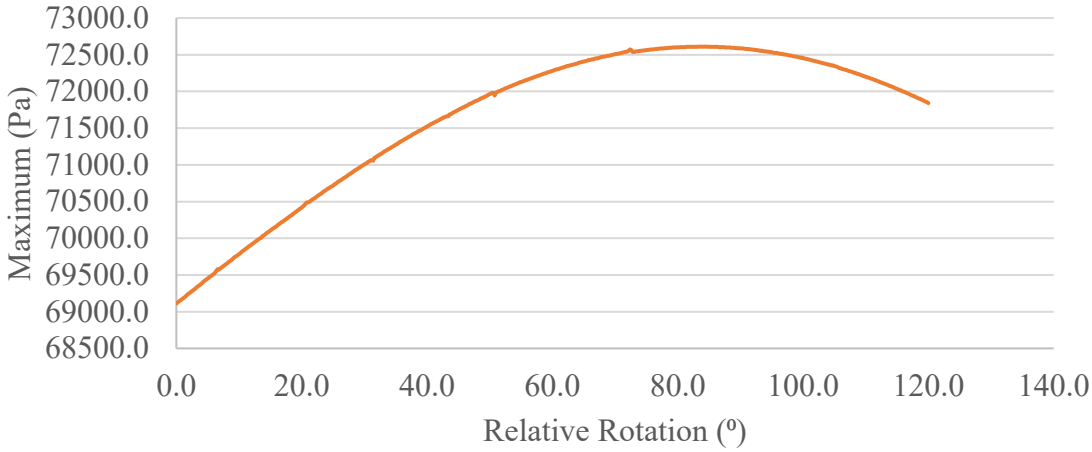

Fig. 79. Peak von Mises stress data on proximal ulna articular cartilage—elbow extension at 20º/s.

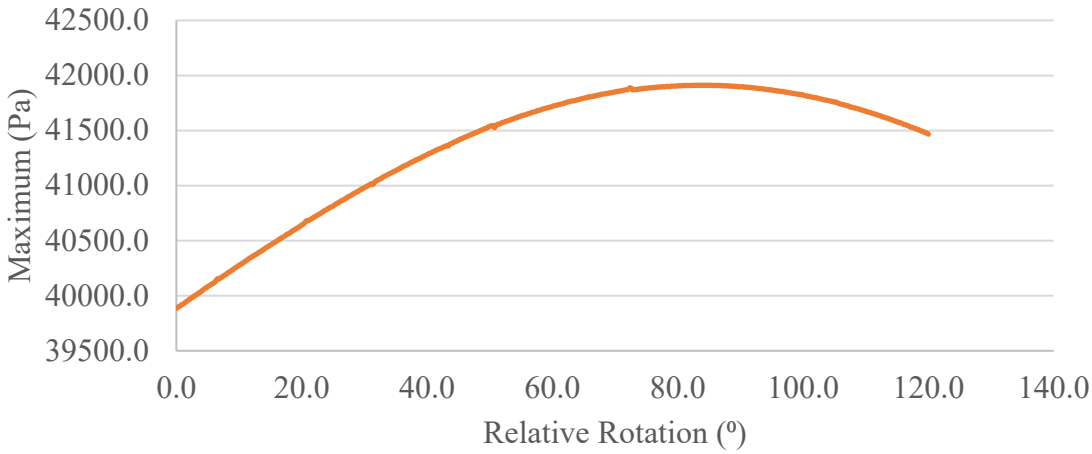

Fig. 80. Peak maximum shear stress data on proximal ulna articular cartilage—elbow extension at 20º/s.

Fig. 81 and Fig. 82 show the contour plots of von Mises stress and maximum shear stress acting on the proximal ulna articular cartilage due to the forces exerted by synovial fluid during elbow extension from 120º to 0º at a joint velocity of 20º/s.

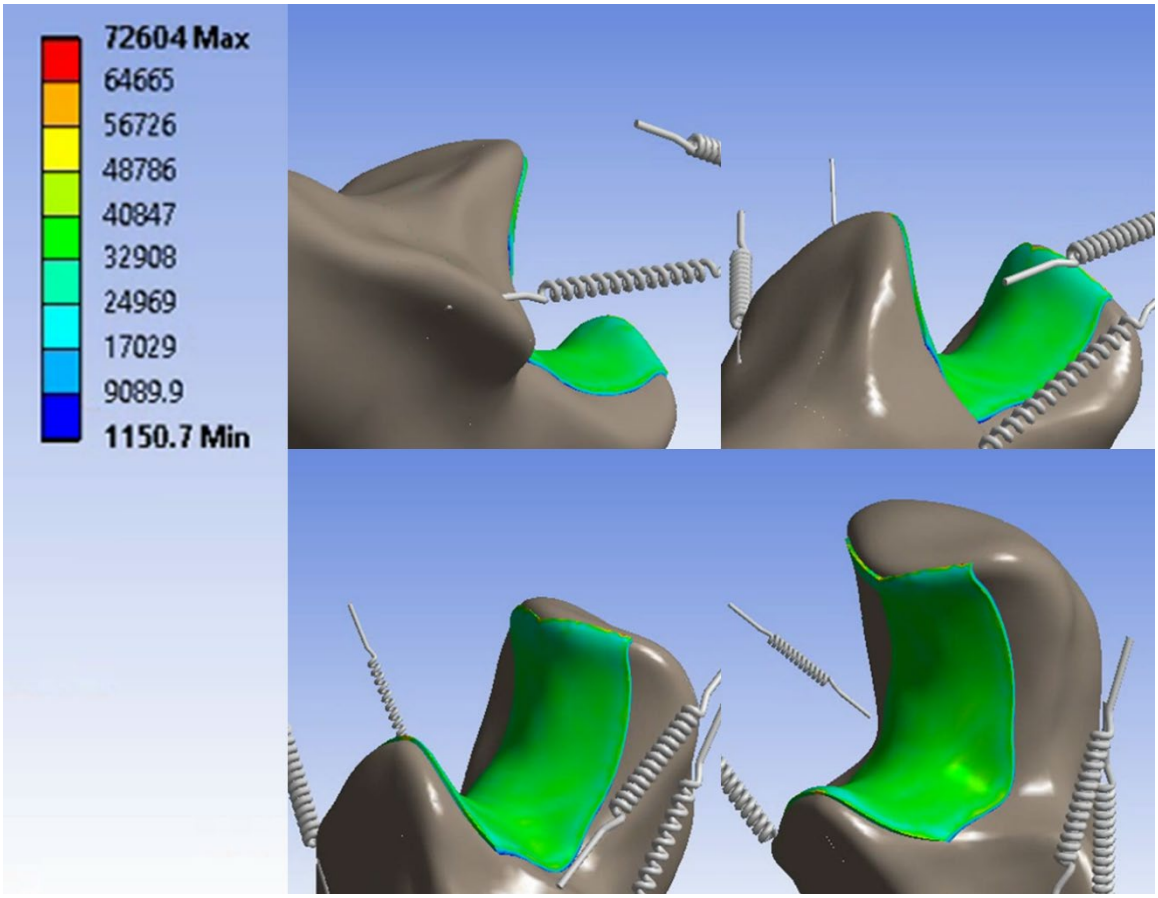

Fig. 81. Contour plot of von Mises stress on proximal ulna articular cartilage—elbow extension at 20º/s. The scale in the figure is represented in Pascals. The motion is starting from the top-left corner in the clockwise-direction and the snapshots were taken at approximately equidistant time intervals.

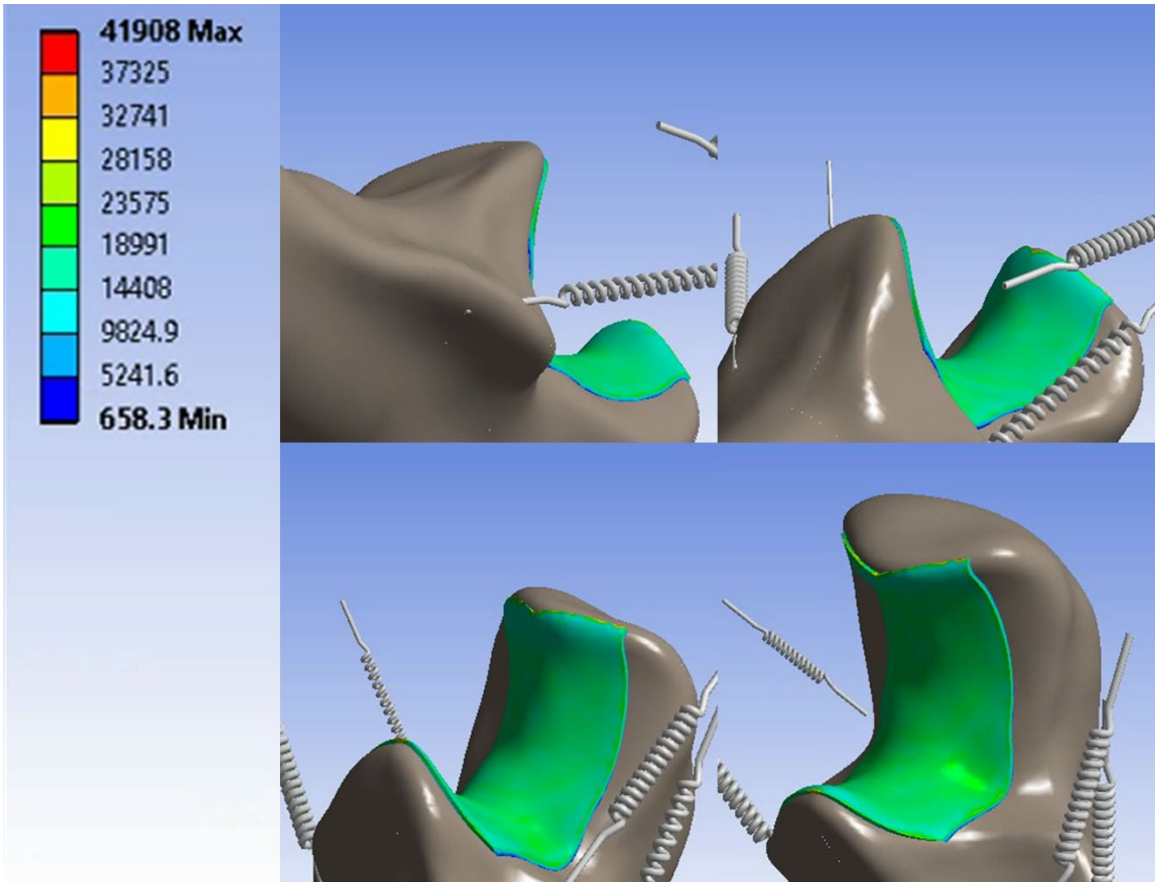

Fig. 82. Contour plot of maximum shear stress on proximal ulna articular cartilage—elbow extension at 20º/s. The scale in the figure is represented in Pascals. The motion is starting from the top-left corner in the clockwise-direction and the snapshots were taken at approximately equidistant time intervals.

Fig. 83 and Fig. 84 show the velocity streamlines of synovial fluid velocity near proximal ulna articular cartilage during elbow extension from 120º to 0º at a joint velocity of 20º/s in isometric and side views, respectively. Maximum synovial fluid velocity of 0.002 m/s was recorded.

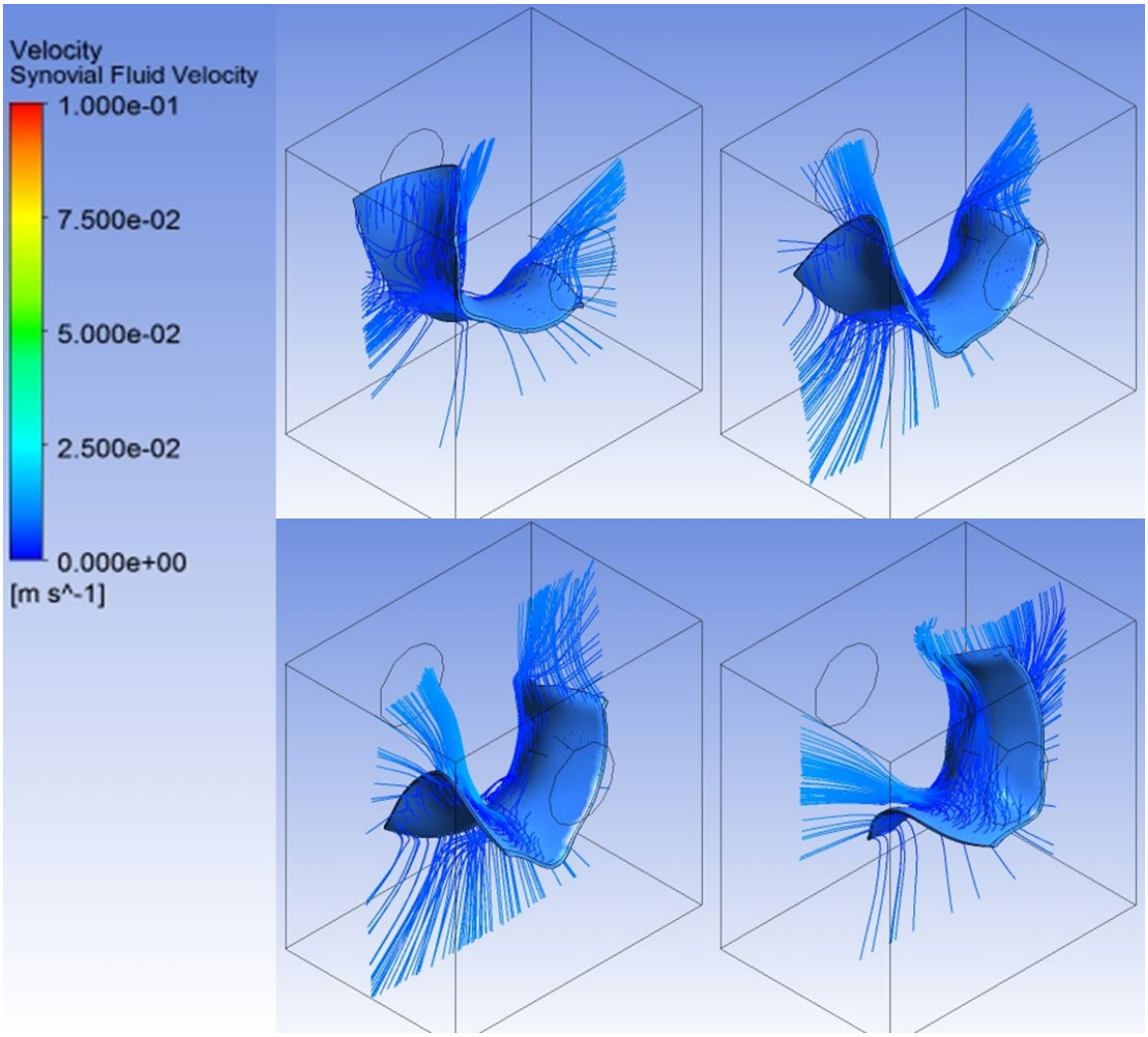

Fig. 83. Velocity streamlines of synovial fluid—elbow extension at 20º/s (isometric view). The motion is starting from the top-left corner in the clockwise-direction and the snapshots were taken at approximately equidistant time intervals.

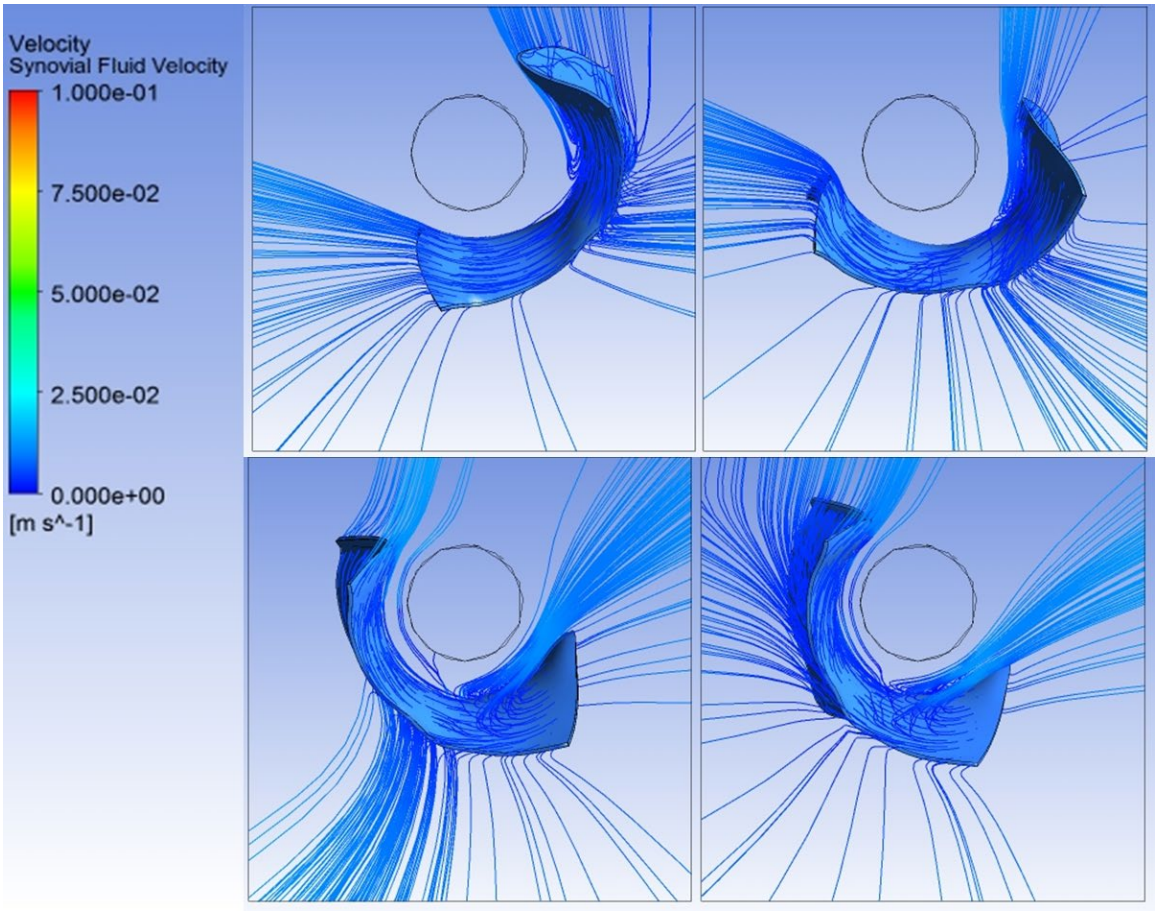

Fig. 84. Velocity streamlines of synovial fluid—elbow extension at 20º/s (side view). The motion is starting from the top-left corner in the clockwise-direction and the snapshots were taken at approximately equidistant time intervals.

Fig. 85 shows that the mass-flow rate of synovial fluid at velocity inlet and pressure outlet is conserved during the full range of elbow extension from 120º to 0º at a joint velocity of 20º/s.

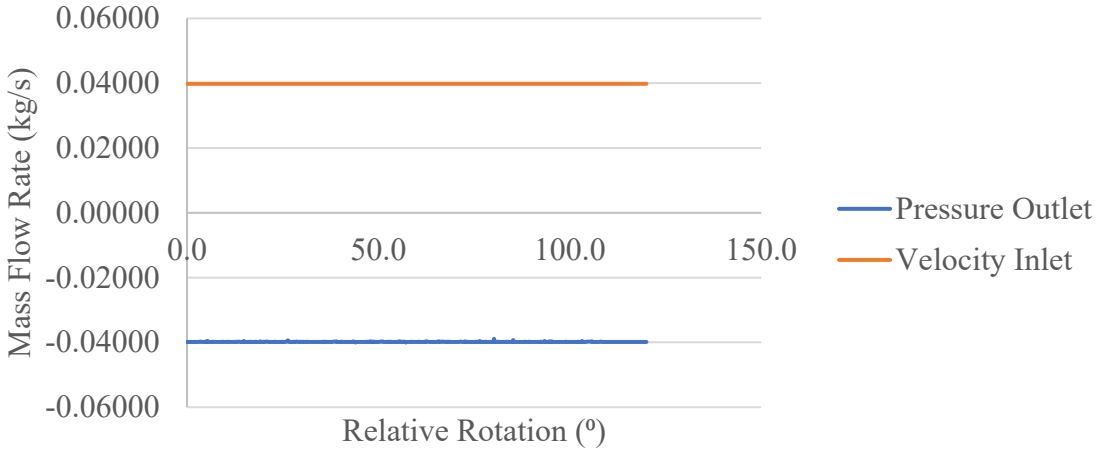

Fig. 85. Synovial fluid mass flow rate data—elbow extension at 20º/s.

Fig. 86 shows the RMS change of data transfer of the structural displacement of proximal ulna articular cartilage between ANSYS Transient Structural and ANSYS Fluent during the FSI simulation of elbow extension from 120º to 0º at a joint velocity of 20º/s.

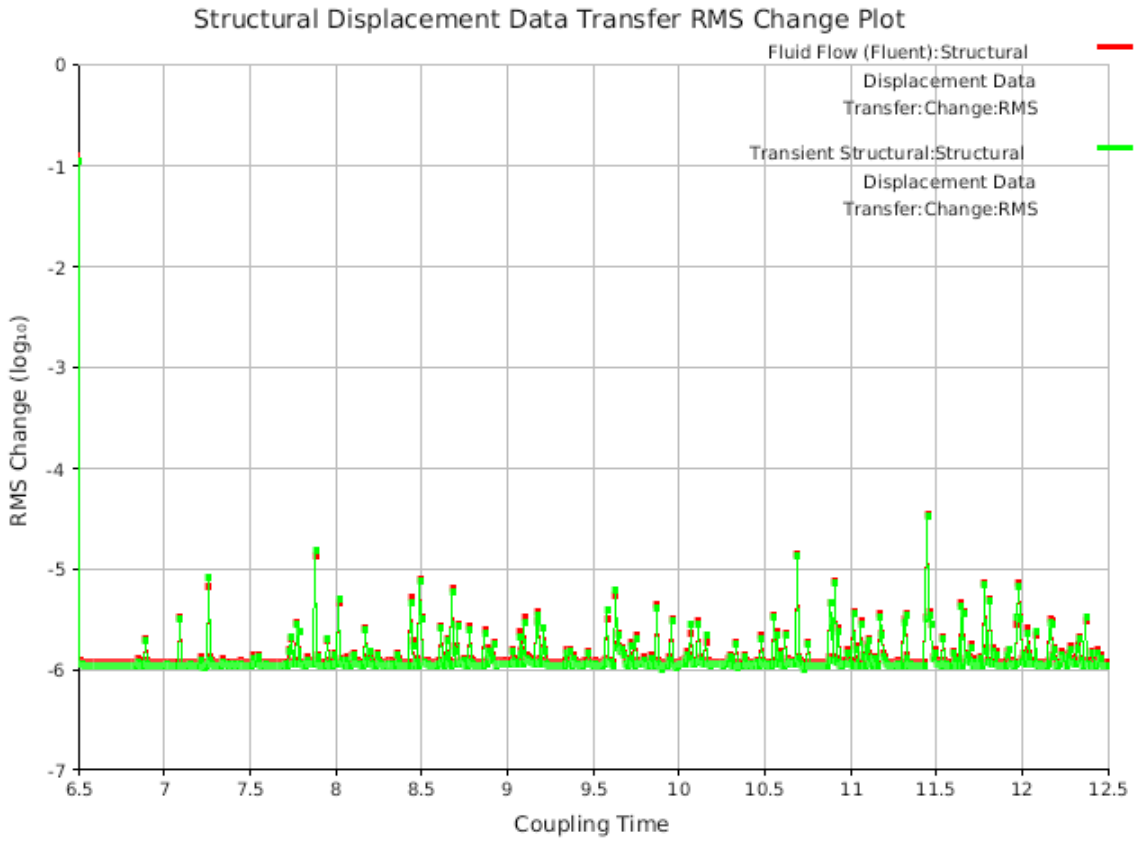

Fig. 86. Structural displacement data transfer RMS change plot—elbow extension at 20º/s.

Fig. 87 shows the RMS change of data transfer of the synovial fluid forces acting on proximal ulna articular cartilage between ANSYS Transient Structural and ANSYS Fluent during the FSI simulation of elbow extension from 120º to 0º at a joint velocity of 20º/s.

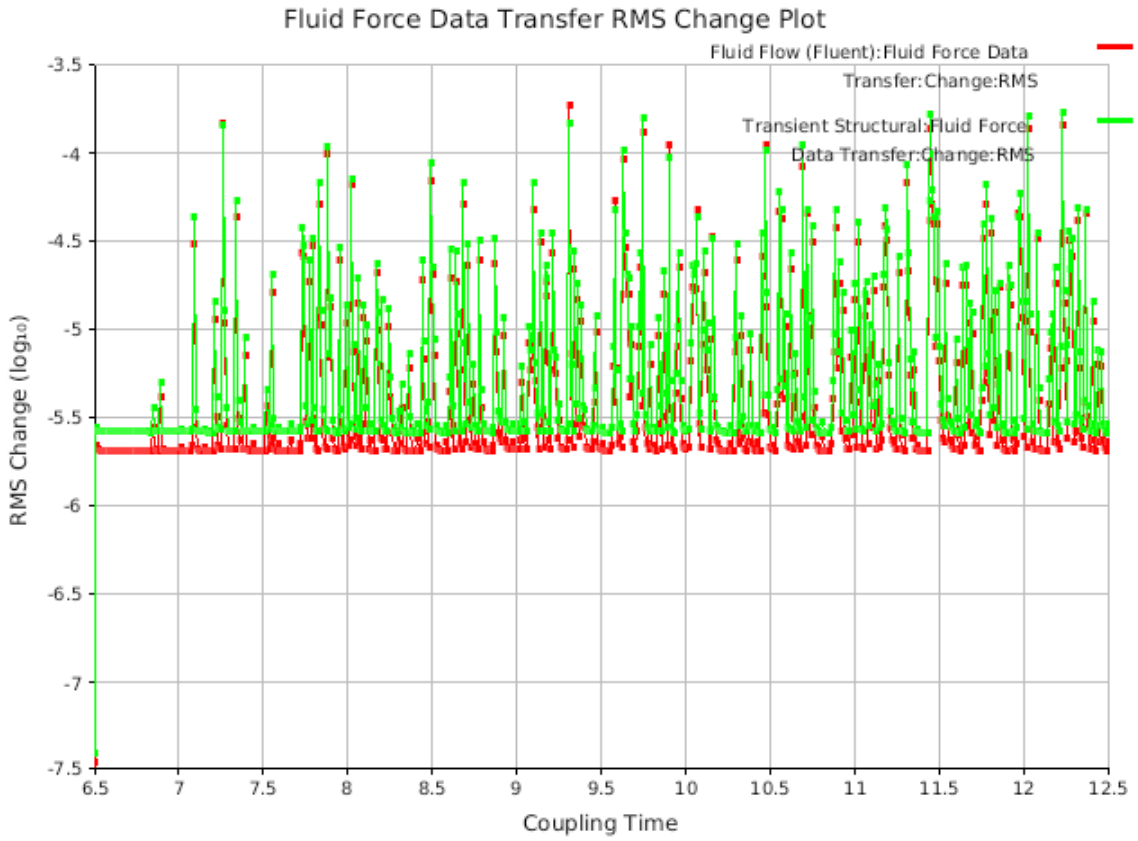

Fig. 87. Fluid force data transfer RMS change plot—elbow extension at 20º/s.

4.5 Extension at 120º/s

Fig. 88 shows the relationship between constraint moment generated by elbow extensors and ligaments, elastic moment generated by elbow extensors stiffness, and total moment generated at the elbow joint during elbow extension from 120º to 0º at a joint velocity of 120º/s. Comparing the constraint moment and elastic moment curves in Fig. 88 with the elbow extensors moment curve (bold, black curve labeled as 'model') in Fig. 15, shows that the elbow joint model developed in this FSI simulation correlates well with the published elbow joint model [29].

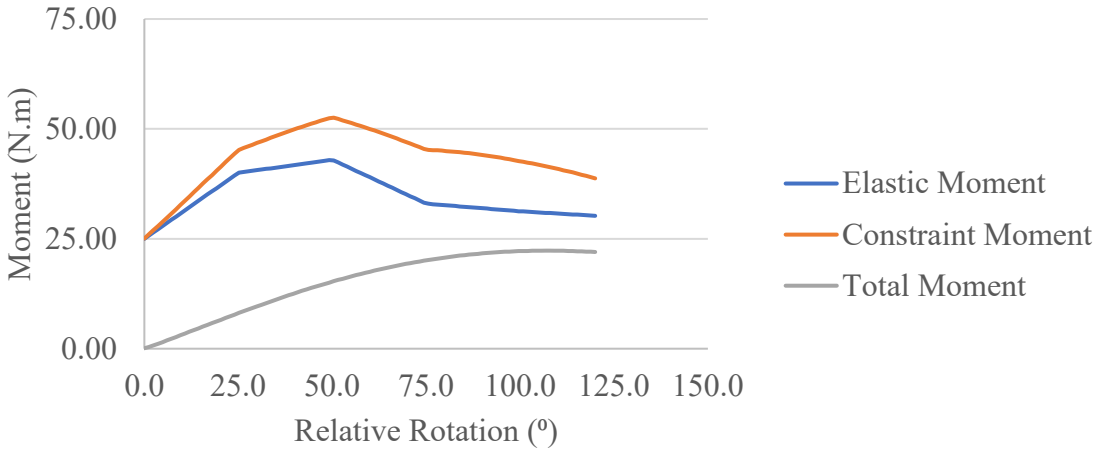

Fig. 88. Joint moment vs. rotation data—elbow extension at 120º/s.

Fig. 89 provides the ligament load data with respect to elbow extension angle during elbow extension from 120º to 0º at a joint velocity of 120º/s. Peak loads of 865.72 N, 115.65 N, 542.15 N, and 527.63 N were observed for LUCL, RCL, MCL-Anterior, and MCL-Posterior, respectively.

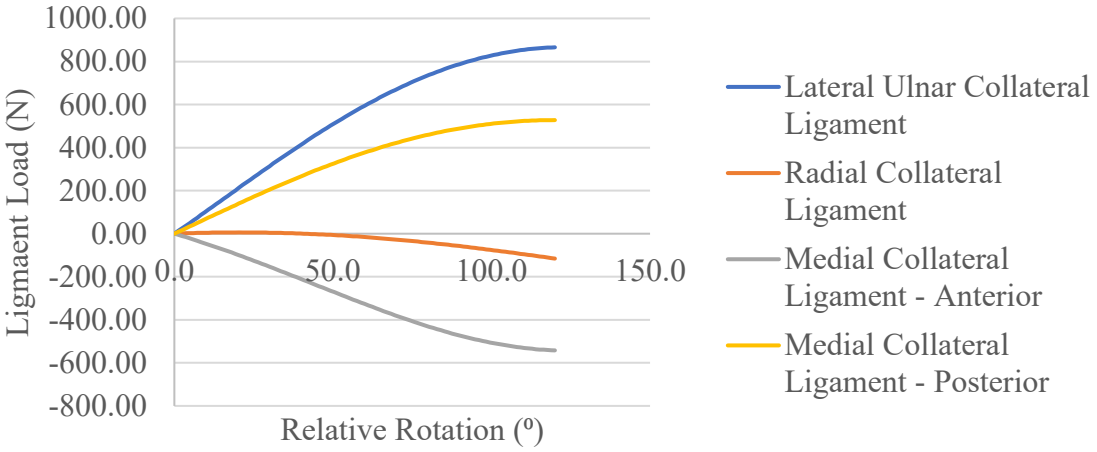

Fig. 89. Ligament load data—elbow extension at 120º/s.

Fig. 90 and Fig. 91 show the relationship between the peak von Mises stress and peak maximum shear stress acting on the proximal ulna articular cartilage due to the forces exerted by synovial fluid with respect to extension angle during elbow extension from 120º to 0º at a joint velocity of 120º/s. Peak von Mises stress of 72,642 Pa or 0.0073 MPa, and peak maximum shear stress of 41,930 Pa or 0.0042 MPa were recorded to be acting on proximal ulna articular cartilage.

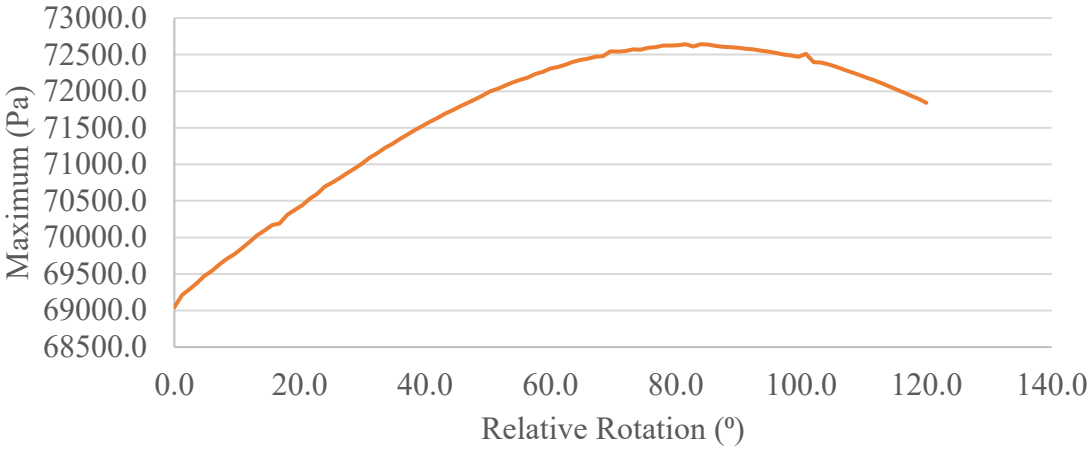

Fig. 90. Peak von Mises stress data on proximal ulna articular cartilage—elbow extension at 120º/s.

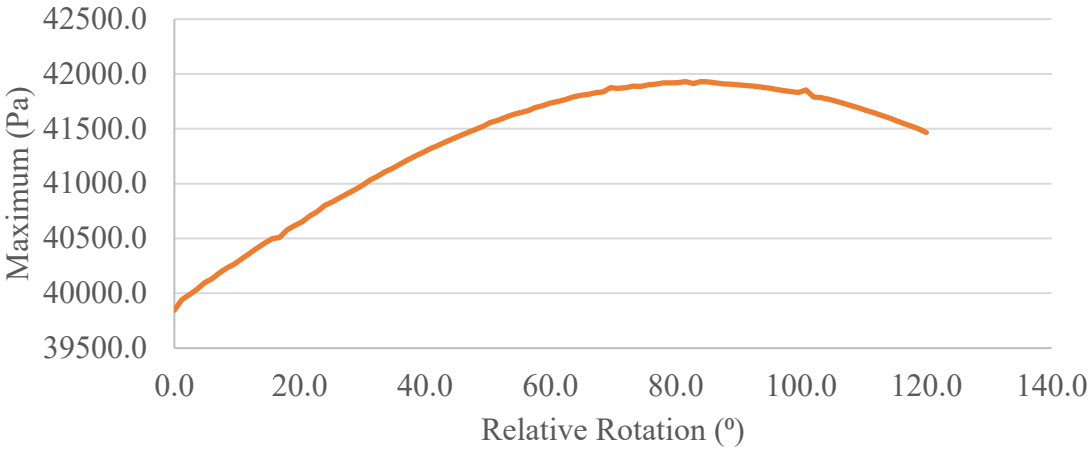

Fig. 91. Peak maximum shear stress data on proximal ulna articular cartilage—elbow extension at 120º/s.

Fig. 92 and Fig. 93 show the contour plots of von Mises stress and maximum shear stress acting on the proximal ulna articular cartilage due to synovial fluid forces during elbow extension from 120º to 0º at a joint velocity of 120º/s.

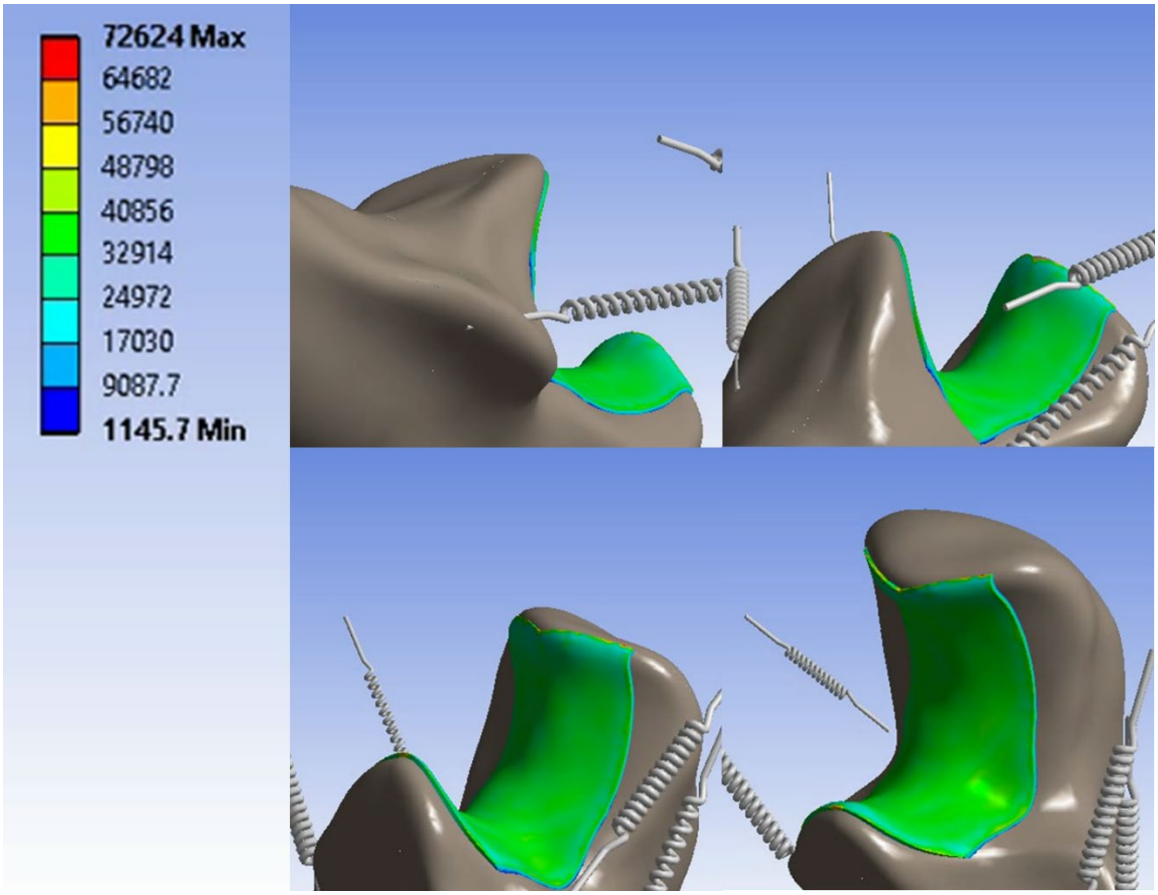

Fig. 92. Contour plot of von Mises stress on proximal ulna articular cartilage—elbow extension at 120º/s. The scale in the figure is represented in Pascals. The motion is starting from the top-left corner in the clockwise-direction and the snapshots were taken at approximately equidistant time intervals.

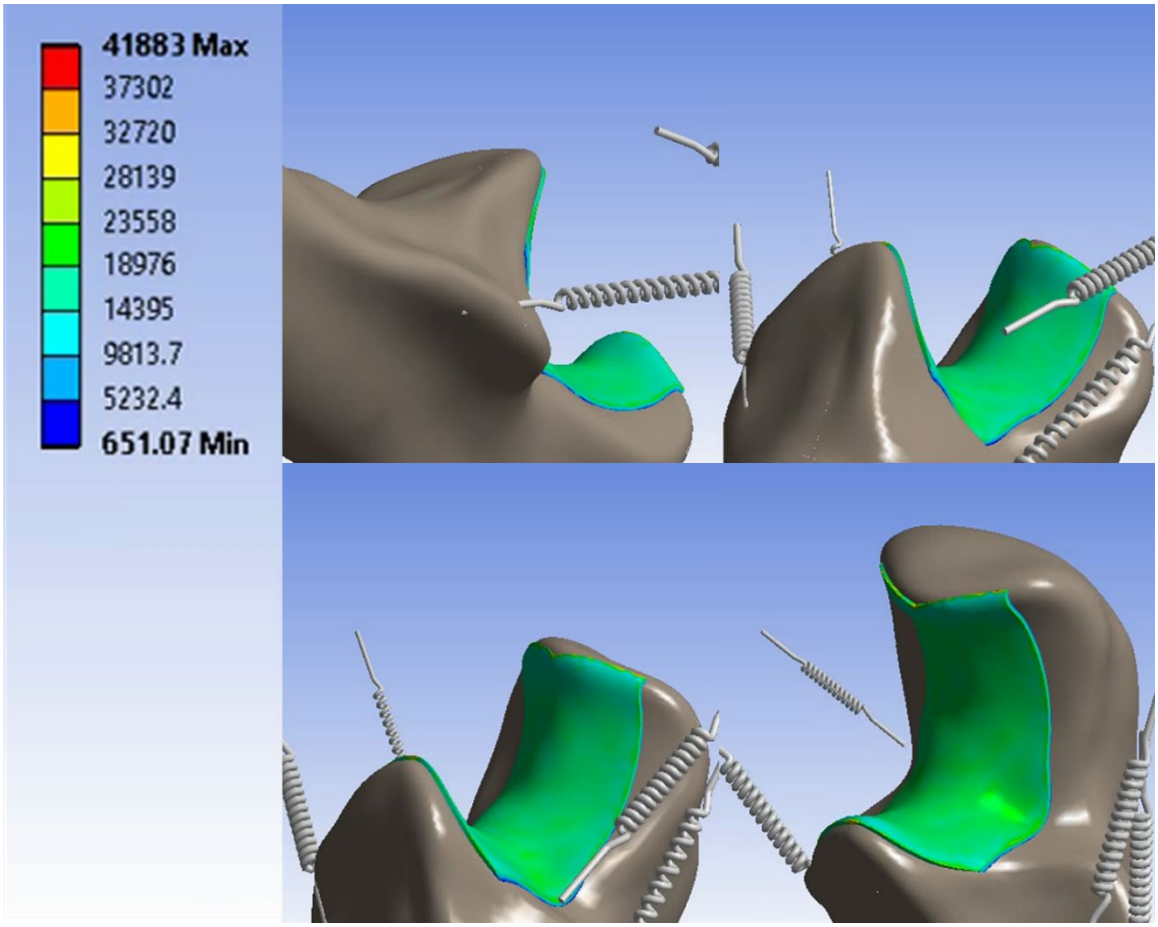

Fig. 93. Contour plot of maximum shear stress on proximal ulna articular cartilage—elbow extension at 120º/s. The scale in the figure is represented in Pascals. The motion is starting from the top-left corner in the clockwise-direction and the snapshots were taken at approximately equidistant time intervals.

Fig. 94 and Fig. 95 show the velocity streamlines of synovial fluid velocity near proximal ulna articular cartilage during elbow extension from 120º to 0º at a joint velocity of 120º/s in isometric and side views, respectively. Maximum synovial fluid velocity of 0.01 m/s was recorded.

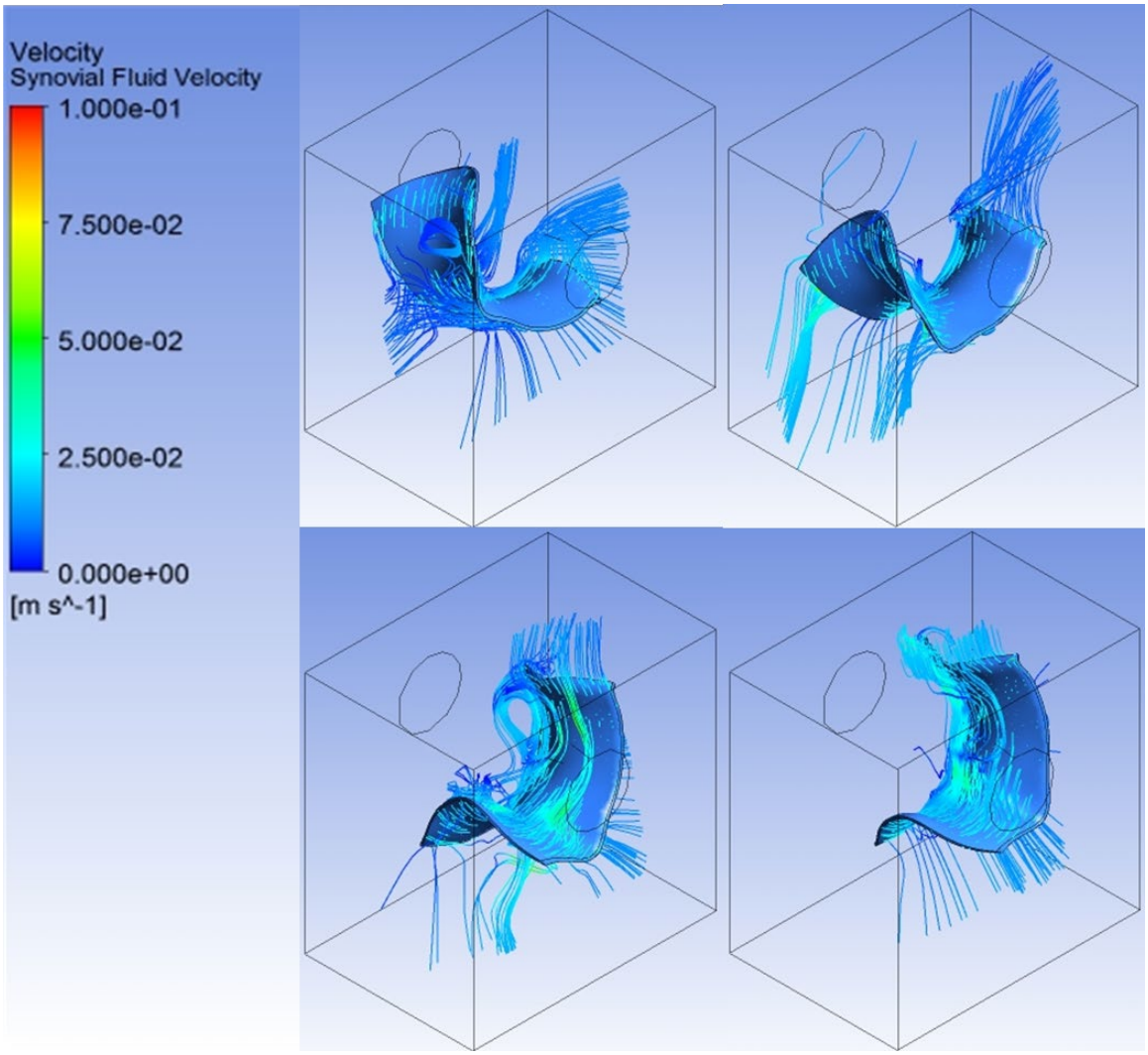

Fig. 94. Velocity streamlines of synovial fluid—elbow extension at 120º/s (isometric view). The motion is starting from the top-left corner in the clockwise-direction and the snapshots were taken at approximately equidistant time intervals.

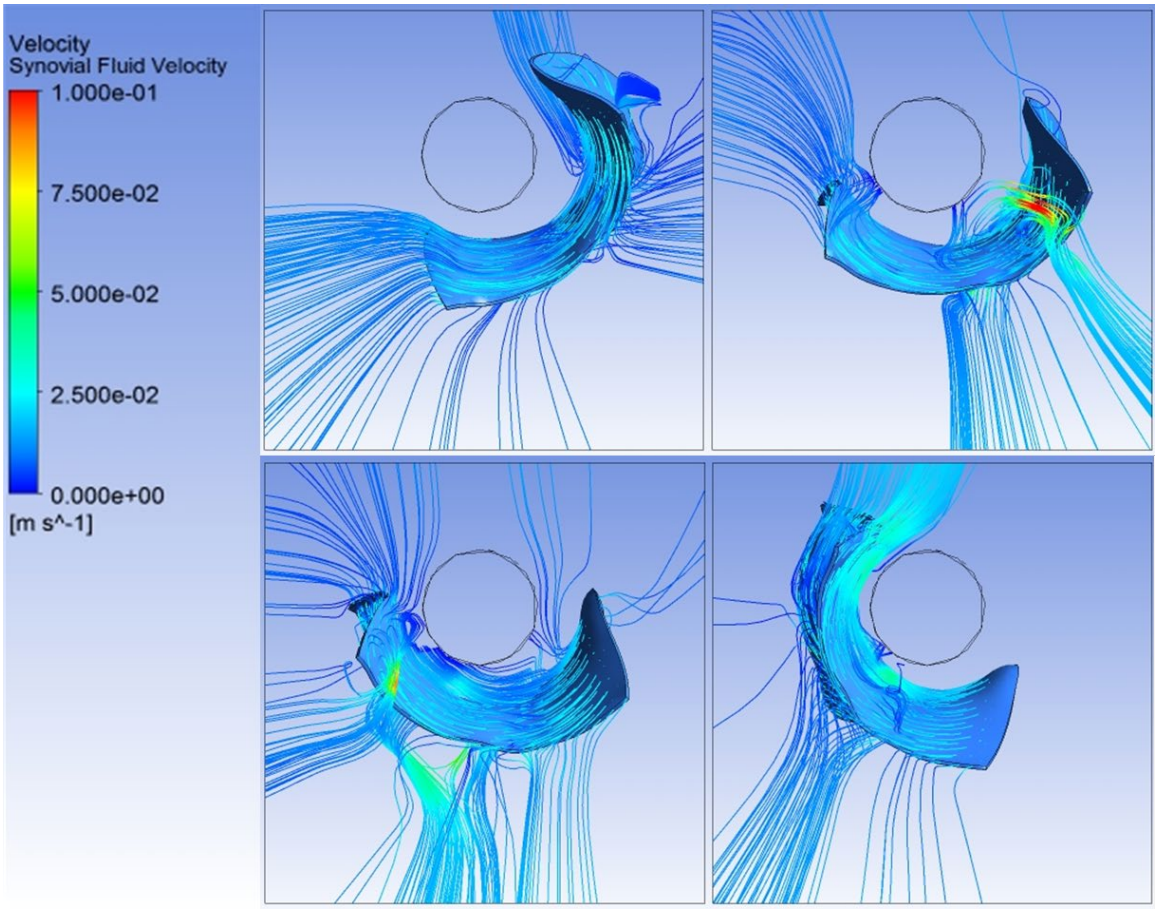

Fig. 95. Velocity streamlines of synovial fluid—elbow extension at 120º/s (side view). The motion is starting from the top-left corner in the clockwise-direction and the snapshots were taken at approximately equidistant time intervals.

Fig. 96 shows that the mass-flow rate of synovial fluid at velocity inlet and pressure outlet is conserved during the full range of elbow extension from 120º to 0º at a joint velocity of 120º/s.

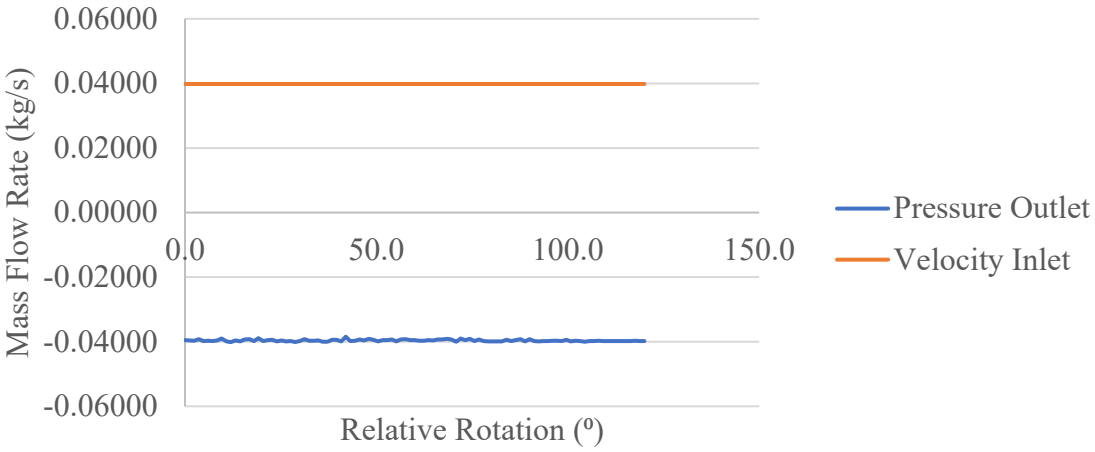

Fig. 96. Synovial fluid mass flow rate data—elbow extension at 120º/s.

Fig. 97 shows the RMS change of data transfer of the structural displacement of proximal ulna articular cartilage between ANSYS Transient Structural and ANSYS Fluent during the FSI simulation of elbow extension from 120º to 0º at a joint velocity of 120º/s.

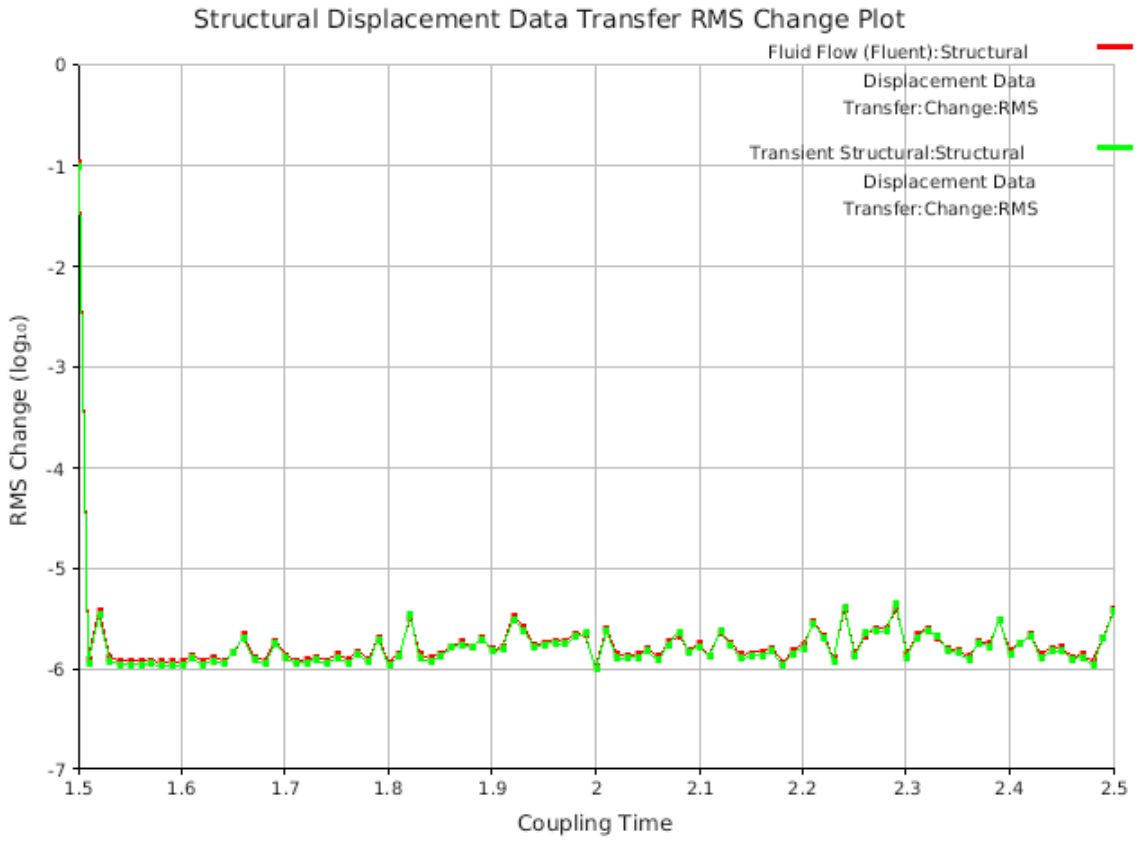

Fig. 97. Structural displacement data transfer RMS change plot—elbow extension at 120º/s.

Fig. 98 shows the RMS change of data transfer of the synovial fluid forces acting on proximal ulna articular cartilage between ANSYS Transient Structural and ANSYS Fluent during the FSI simulation of elbow extension from 120º to 0º at a joint velocity of 120º/s.

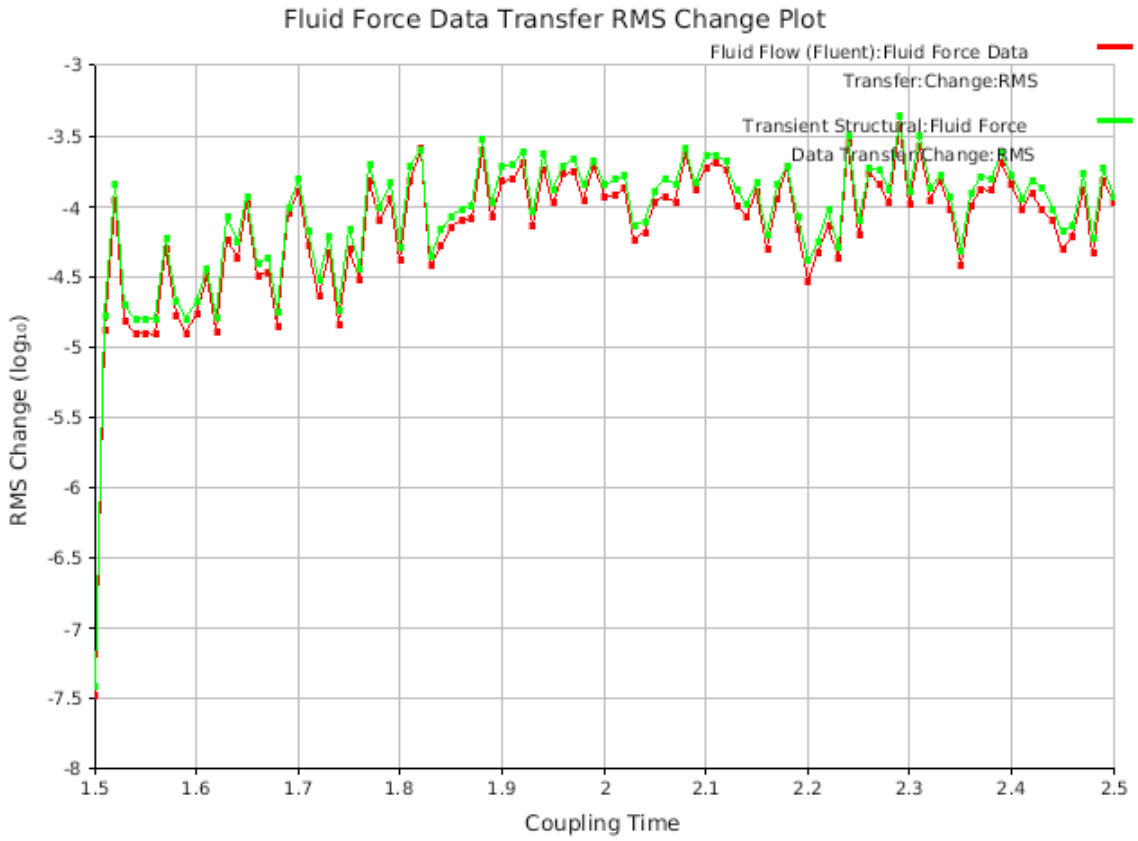

Fig. 98. Fluid force data transfer RMS change plot—elbow extension at 120º/s.

4.6 Summary of Extension Data

The computational elbow joint model for elbow extension correlates well with the published elbow joint model [29] for both 20º/s and 120º/s joint velocity conditions.

For both 20º/s and 120º/s elbow extension conditions, peak loads of 865.72 N, 115.65 N, 542.15 N, and 527.63 N were determined for LUCL, RCL, MCL-Anterior, and MCL-Posterior, respectively.

The peak von Mises stress and peak maximum shear stress acting on the proximal ulna articular cartilage was determined to be 0.0073 MPa and 0.0042 MPa, respectively for both 20º/s and 120º/s elbow extension conditions.

During the slower 20º/s elbow extension, synovial fluid flow was predominantly laminar with a maximum velocity of 0.002 m/s. However, during the faster, 120º/s elbow extension, synovial fluid flow exhibited turbulence with a maximum velocity of 0.01 m/s which is equal to the inlet velocity of the fluid domain.

4.7 Pronation at 40º/s

Fig. 99 shows the relationship between constraint moment generated by elbow pronators and ligaments, elastic moment generated by elbow pronators stiffness, and total moment generated at the elbow joint during elbow pronation from 0º to 120º at a joint velocity of 40º/s. Comparing the constraint moment and elastic moment curves in Fig. 99 with the elbow pronators moment curve (bold, black curve labeled as 'model') in Fig. 15, shows that the elbow joint model developed in this FSI simulation correlates well with the published elbow joint model [29].

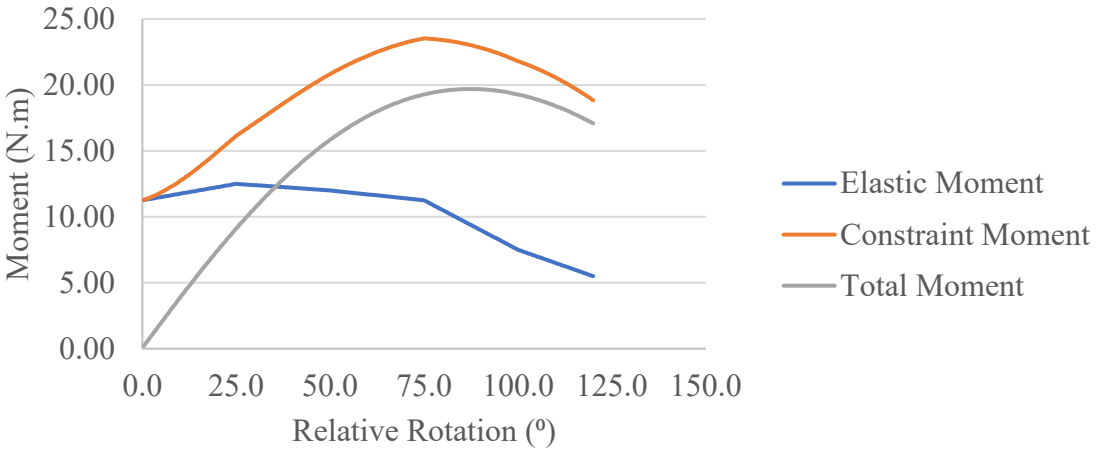

Fig. 99. Joint moment vs. rotation data—elbow pronation at 40º/s.

Fig. 100 and Fig. 101 provides the ligament load data with respect to elbow pronation angle during elbow pronation from 0º to 120º at a joint velocity of 40º/s. Since the interosseous membrane is a sheet-like ligament in the human body, the maximum load generated among the five springs used to define interosseous membrane is considered to be the peak load observed for interosseous membrane. Similarly, the AL exists as a single-body ligament in the human body. Thus, the maximum load generated among the

two springs used to define AL is considered to be the peak load observed for AL. Therefore, peak loads of 447.83 N, and 50.52 N were observed for AL, and interosseous membrane, respectively.

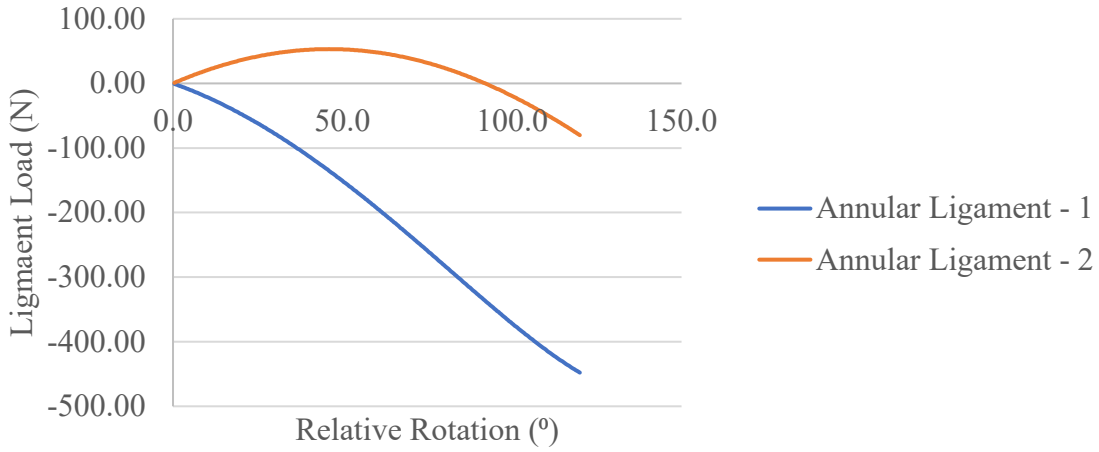

Fig. 100. Ligament (AL) load data—elbow pronation at 40º/s.

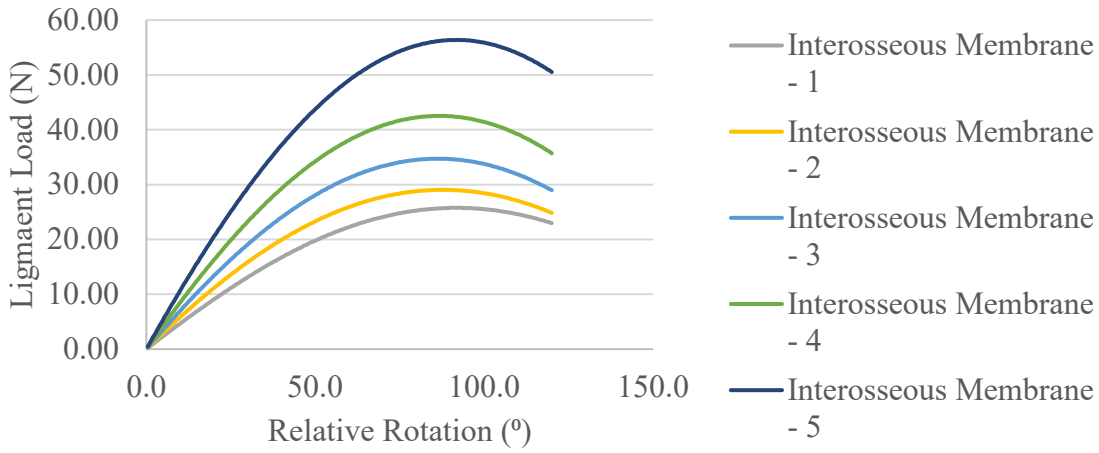

Fig. 101. Ligament (interosseous membrane) load data—elbow pronation at 40º/s.

Fig. 102 and Fig. 103 show the relationship between the peak von Mises stress and peak maximum shear stress acting on the proximal radius articular cartilage due to the forces exerted by synovial fluid with respect to pronation angle during elbow pronation

from 0º to 120º at a joint velocity of 40º/s. Peak von Mises stress of 84,577 Pa or 0.0085 MPa, and peak maximum shear stress of 48,209 Pa or 0.0048 MPa were recorded to be acting on proximal radius articular cartilage.

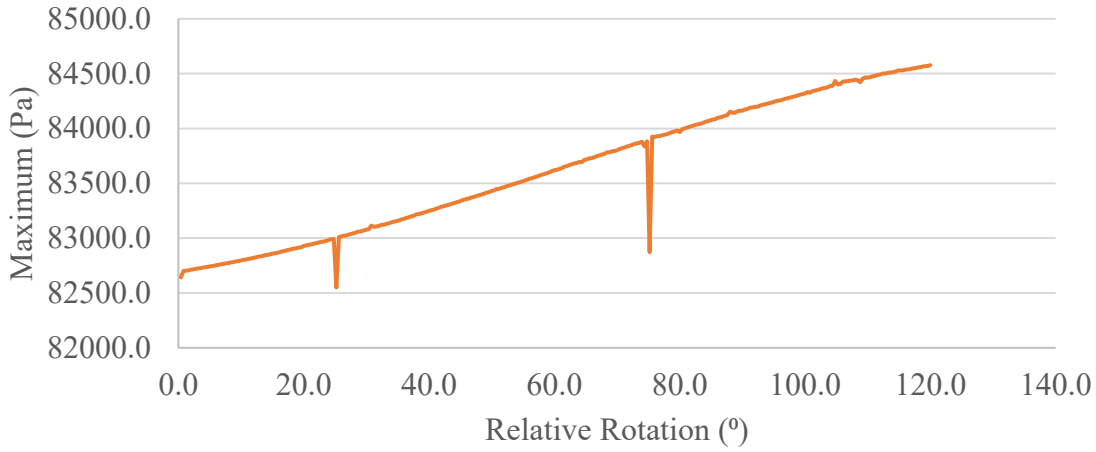

Fig. 102. Peak von Mises stress data on proximal radius articular cartilage—elbow pronation at 40º/s.

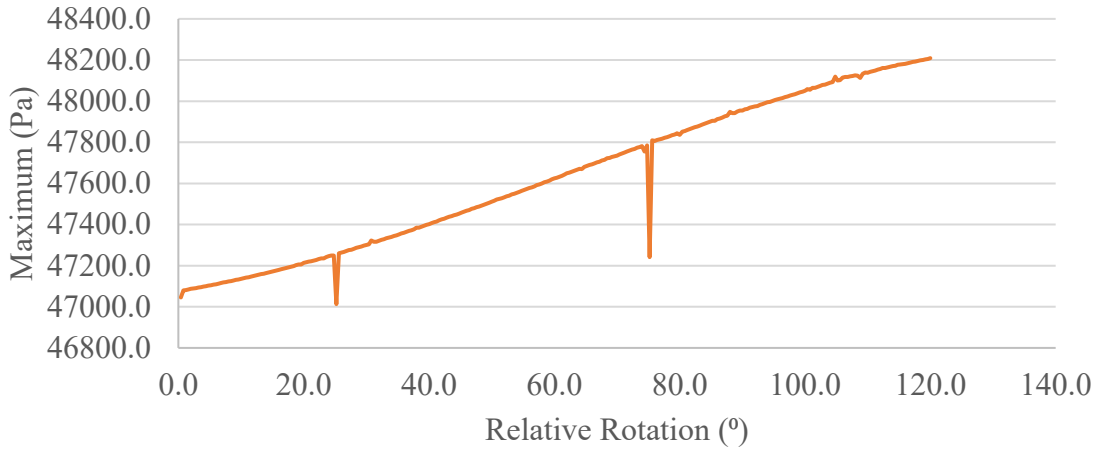

Fig. 103. Peak maximum shear stress data on proximal radius articular cartilage—elbow pronation at 40º/s.

Fig. 104 and Fig. 105 show the contour plots of von Mises stress and maximum shear stress acting on the proximal radius articular cartilage due to the forces exerted by synovial fluid during elbow pronation from 0º to 120º at a joint velocity of 40º/s.

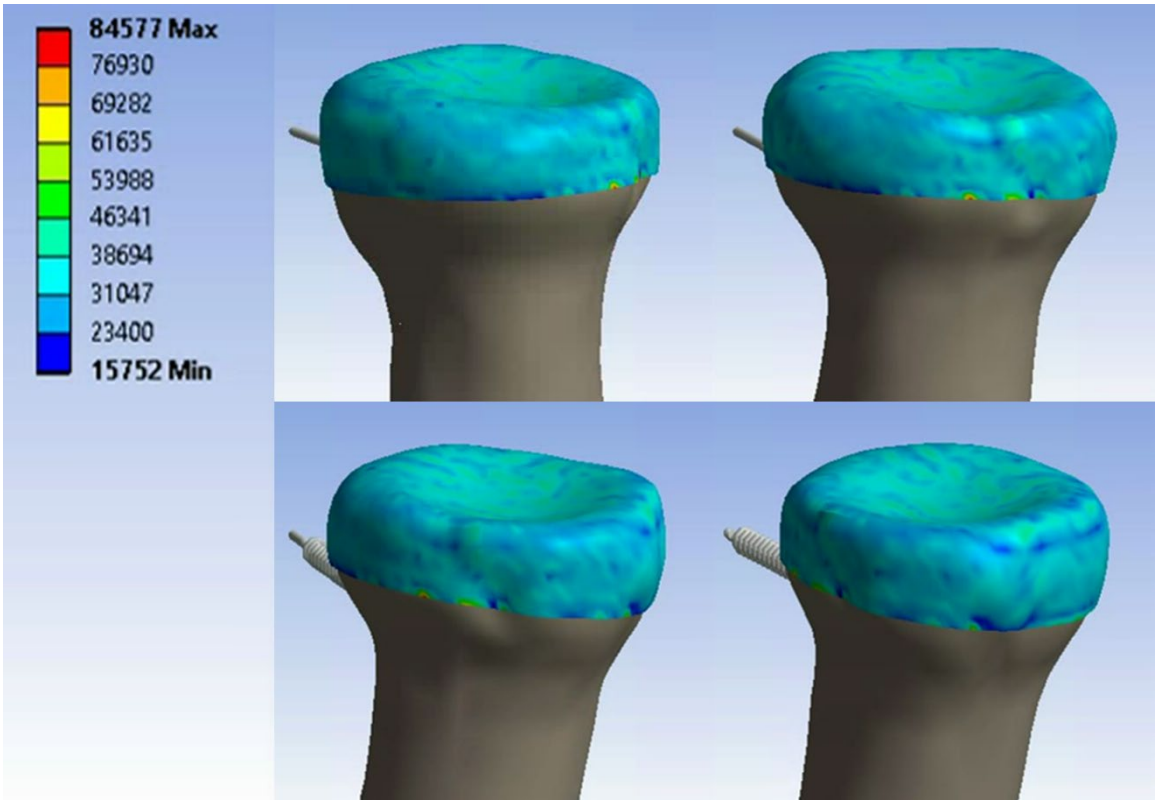

Fig. 104. Contour plot of von Mises stress on proximal radius articular cartilage—elbow pronation at 40º/s. The scale in the figure is represented in Pascals. The motion is starting from the top-left corner in the clockwise-direction and the snapshots were taken at approximately equidistant time intervals.

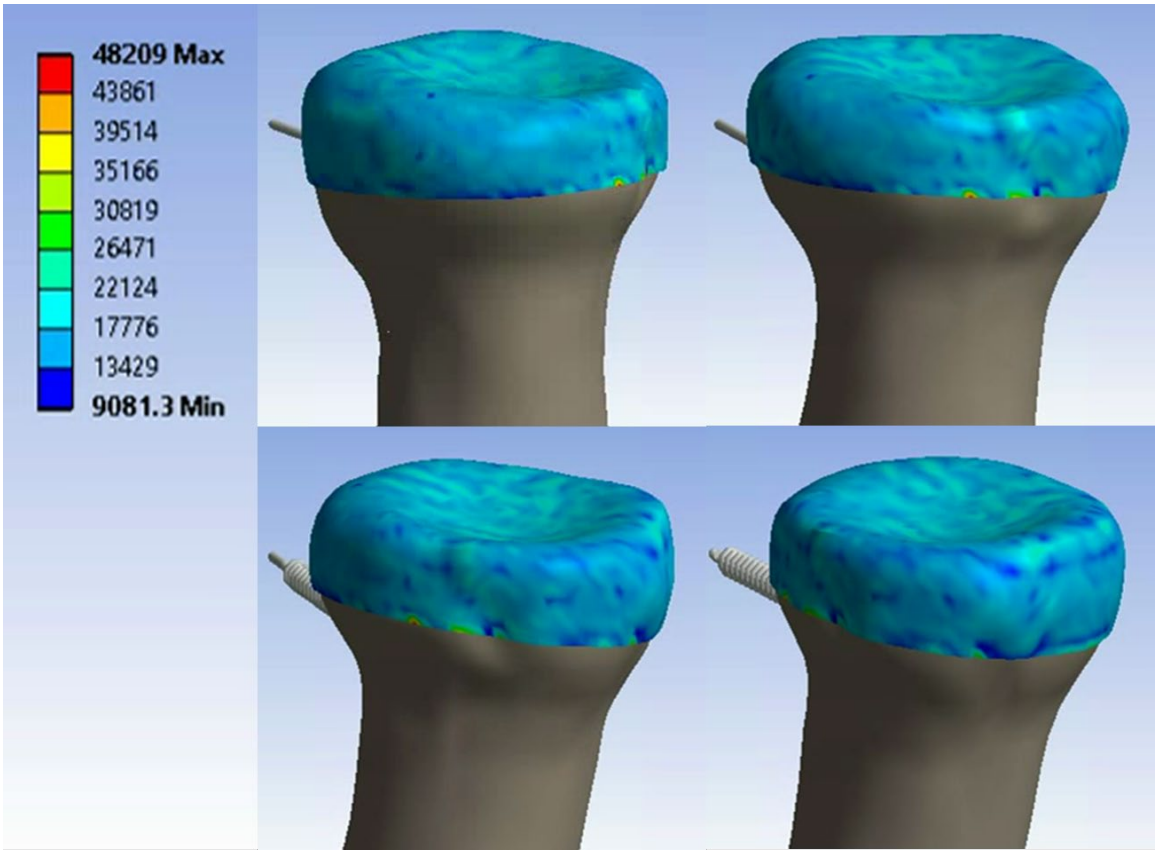

Fig. 105. Contour plot of maximum shear stress on proximal radius articular cartilage—elbow pronation at 40º/s. The scale in the figure is represented in Pascals. The motion is starting from the top-left corner in the clockwise-direction and the snapshots were taken at approximately equidistant time intervals.

Fig. 106 and Fig. 107 show the velocity streamlines of synovial fluid velocity near proximal radius articular cartilage during elbow pronation from 0º to 120º at a joint velocity of 40º/s in isometric and side views, respectively. Maximum synovial fluid velocity of 0.002 m/s was recorded.

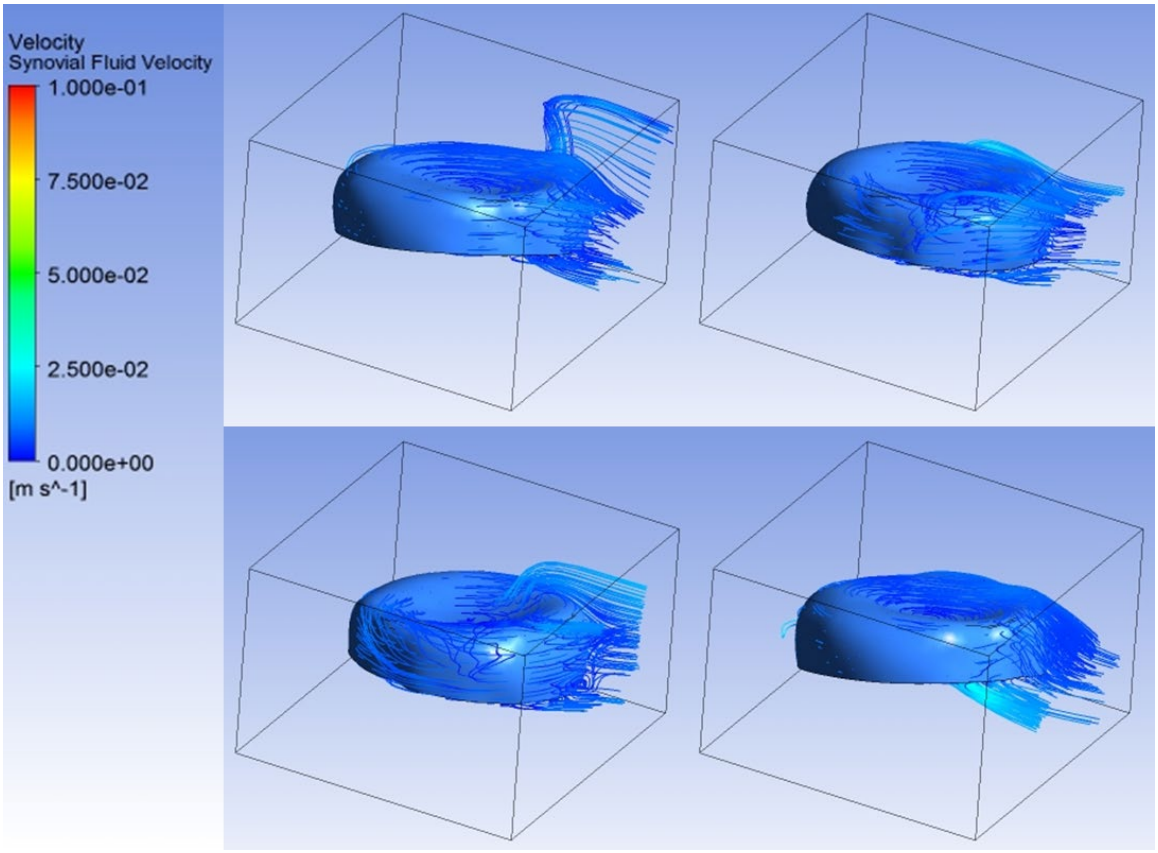

Fig. 106. Velocity streamlines of synovial fluid—elbow pronation at 40º/s (isometric view). The motion is starting from the top-left corner in the clockwise-direction and the snapshots were taken at approximately equidistant time intervals.

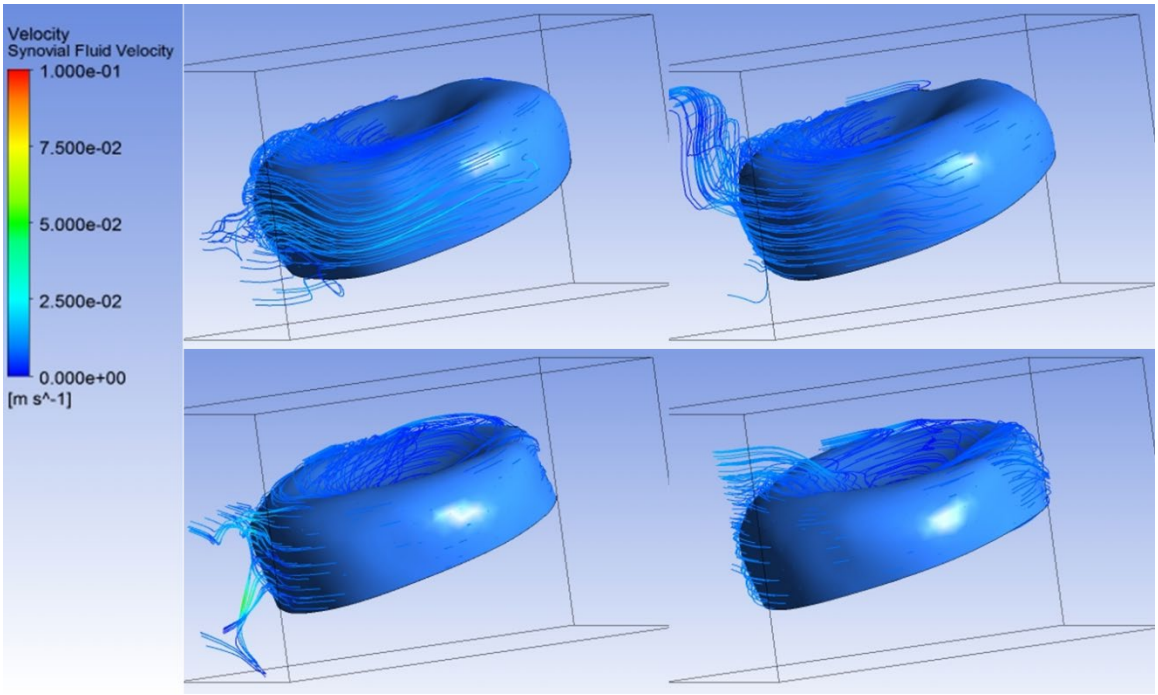

Fig. 107. Velocity streamlines of synovial fluid—elbow pronation at 40º/s (side view). The motion is starting from the top-left corner in the clockwise-direction and the snapshots were taken at approximately equidistant time intervals.

Fig. 108 shows that the mass-flow rate of synovial fluid at velocity inlet and pressure outlet is conserved during the full range of elbow pronation from 0º to 120º at a joint velocity of 40º/s.

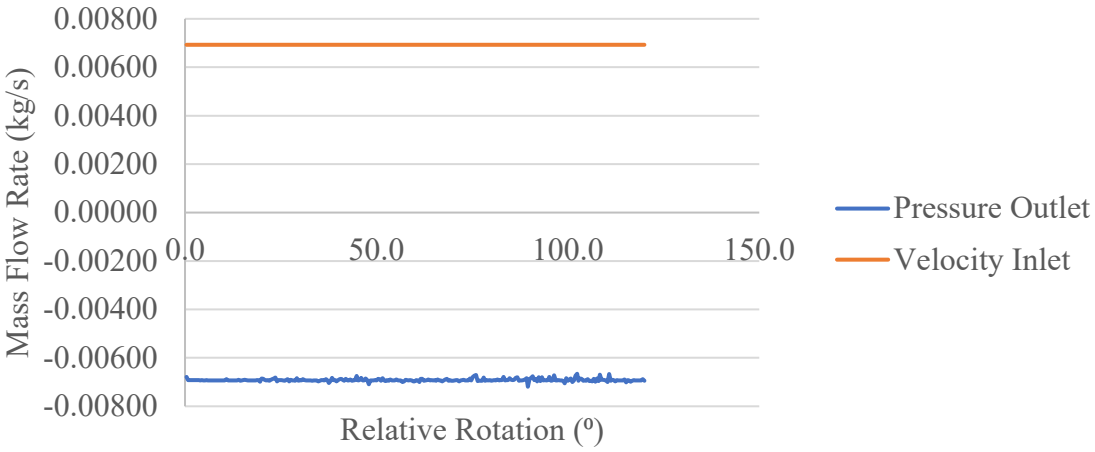

Fig. 108. Synovial fluid mass flow rate data—elbow pronation at 40º/s.

Fig. 109 shows the RMS change of data transfer of the structural displacement of proximal radius articular cartilage between ANSYS Transient Structural and ANSYS Fluent during the FSI simulation of elbow pronation from 0º to 120º at a joint velocity of 40º/s.

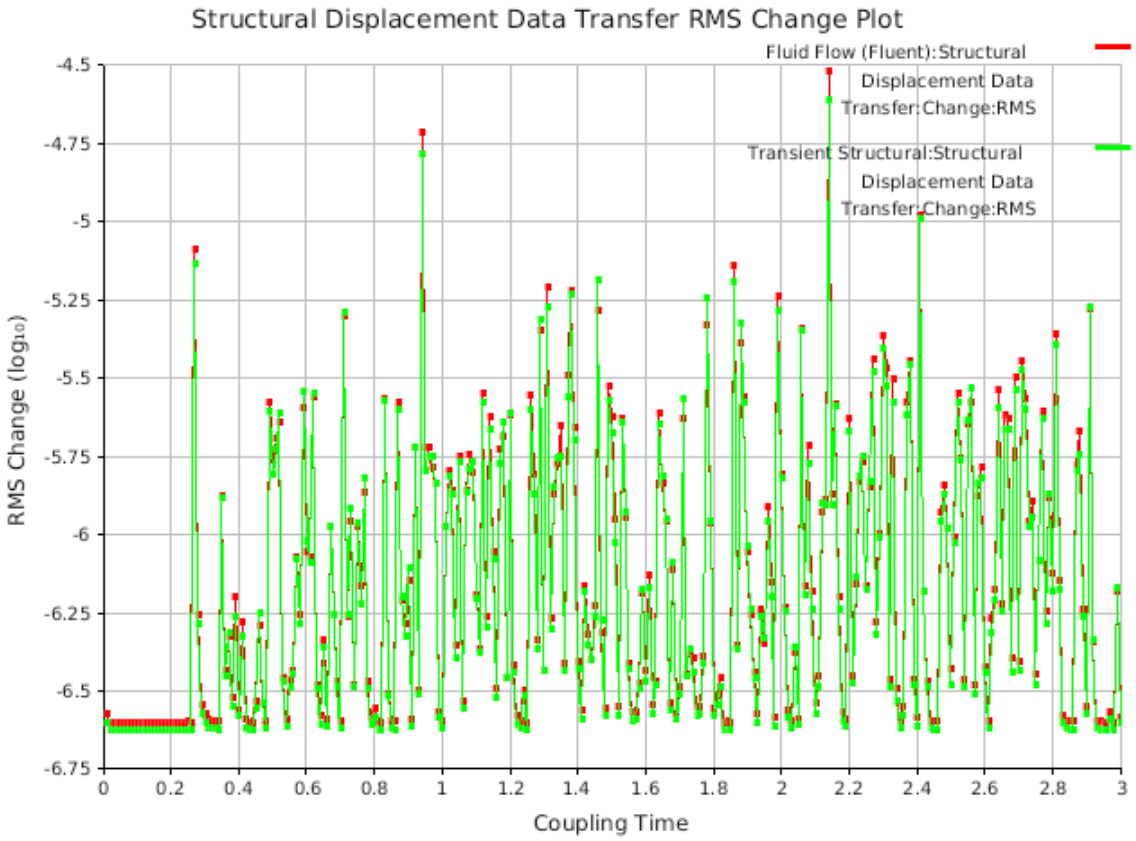

Fig. 109. Structural displacement data transfer RMS change plot—elbow pronation at 40º/s.

Fig. 110 shows the RMS change of data transfer of the synovial fluid forces acting on proximal radius articular cartilage between ANSYS Transient Structural and ANSYS Fluent during the FSI simulation of elbow pronation from 0º to 120º at a joint velocity of 40º/s.

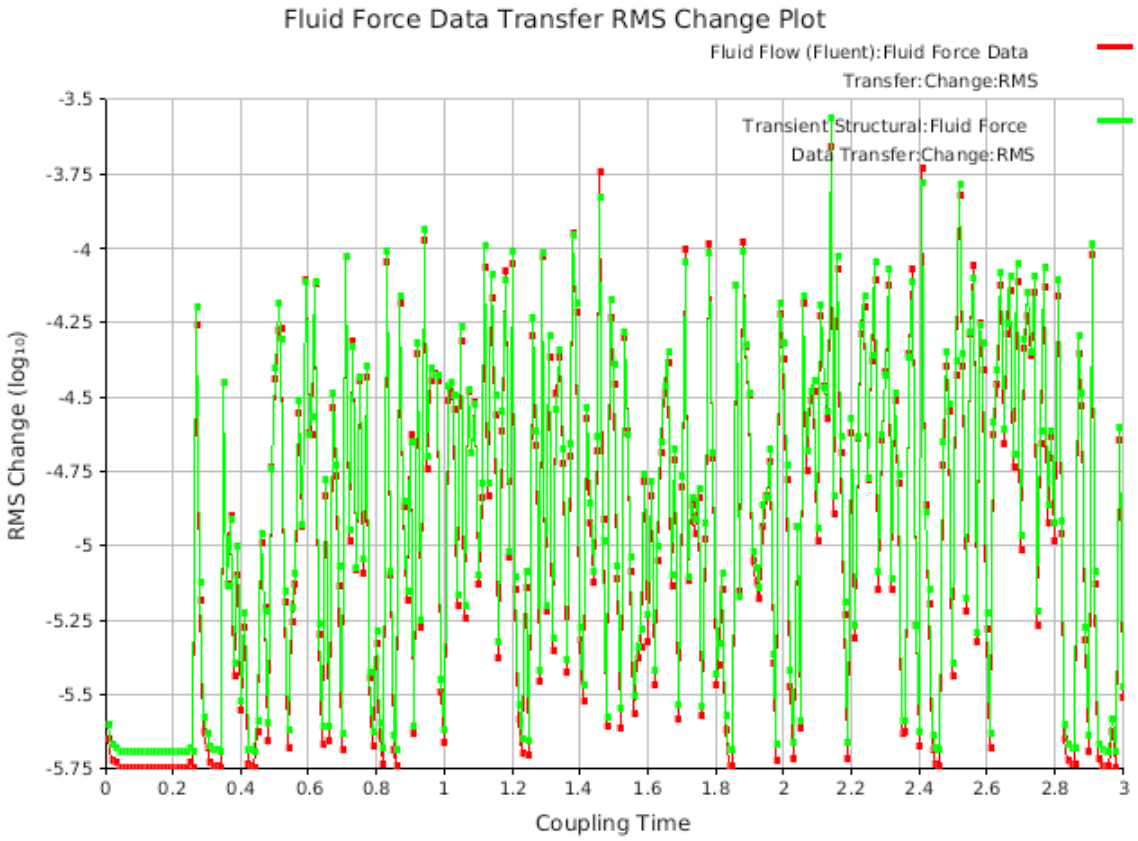

Fig. 110. Fluid force data transfer RMS change plot—elbow pronation at 40º/s.

4.8 Pronation at 120º/s

Fig. 111 shows the relationship between constraint moment generated by elbow pronators and ligaments, elastic moment generated by elbow pronators stiffness, and total moment generated at the elbow joint during elbow pronation from 0º to 120º at a joint velocity of 120º/s. Comparing the constraint moment and elastic moment curves in Fig. 111 with the elbow pronators moment curve (bold, black curve labeled as 'model') in Fig. 15, shows that the elbow joint model developed in this FSI simulation correlates well with the published elbow joint model [29].

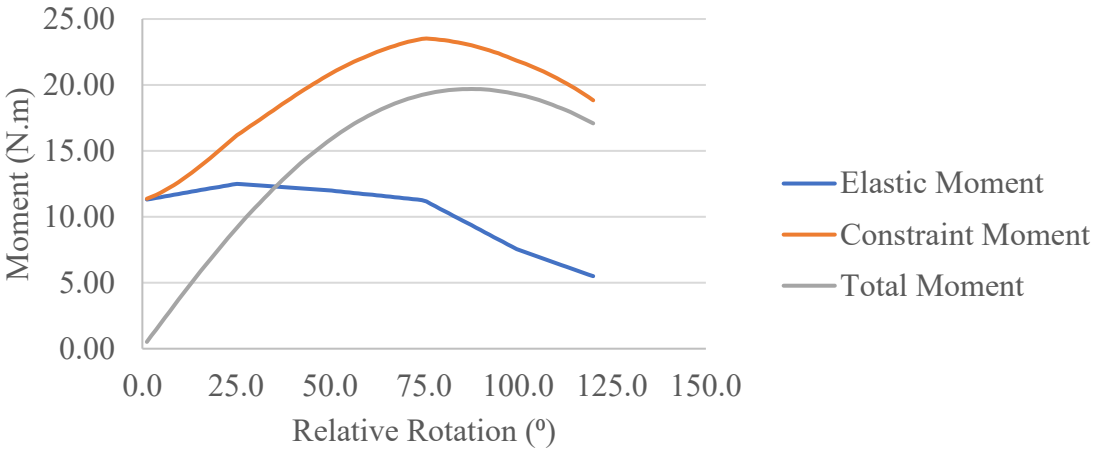

Fig. 111. Joint moment vs. rotation data—elbow pronation at 120º/s.

Fig. 112 and Fig. 113 provides the ligament load data with respect to elbow pronation angle during elbow pronation from 0º to 120º at a joint velocity of 120º/s. Peak loads of 447.83 N, and 50.52 N were observed for AL, and interosseous membrane, respectively.

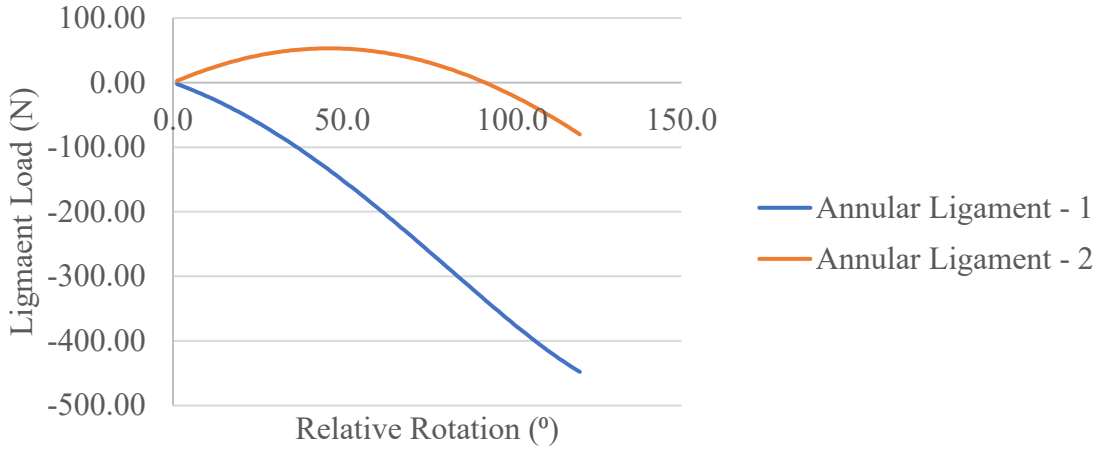

Fig. 112. Ligament (AL) load data—elbow pronation at 120º/s.

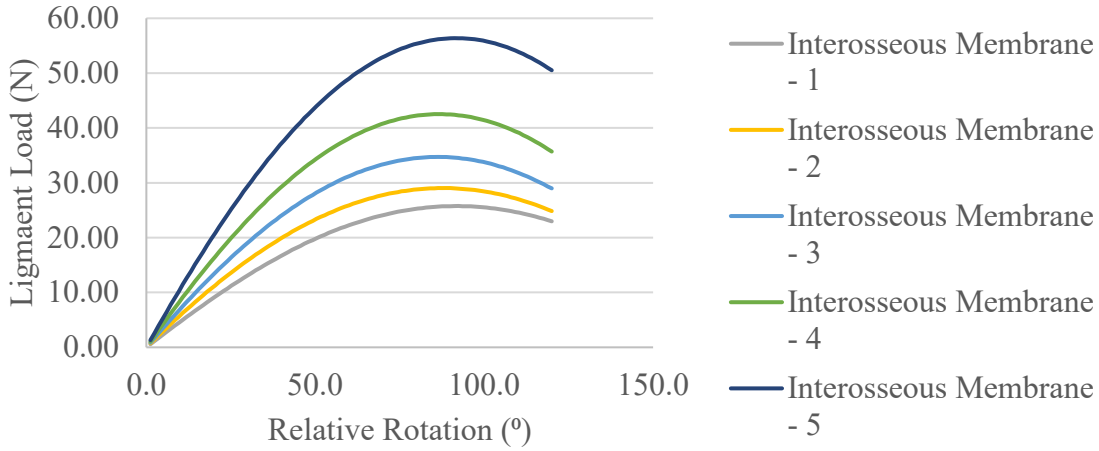

Fig. 113. Ligament (interosseous membrane) load data—elbow pronation at 120º/s.

Fig. 114 and Fig. 115 show the relationship between the peak von Mises stress and peak maximum shear stress acting on the proximal radius articular cartilage due to the forces exerted by synovial fluid with respect to pronation angle during elbow pronation from 0º to 120º at a joint velocity of 120º/s. Peak von Mises stress of 84,576 Pa or 0.0085 MPa, and peak maximum shear stress of 48,196 Pa or 0.0048 MPa were recorded to be acting on proximal radius articular cartilage.

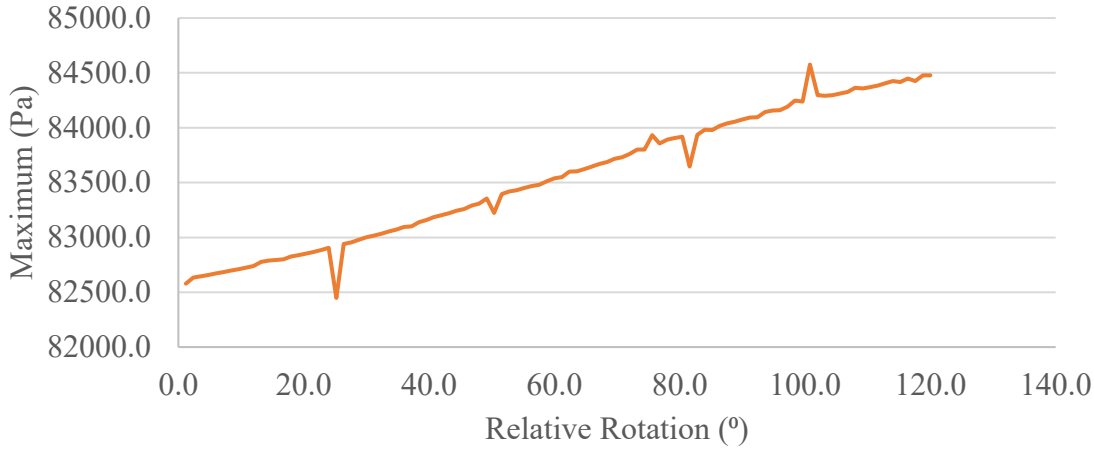

Fig. 114. Peak von Mises stress data on proximal radius articular cartilage—elbow pronation at 120º/s.

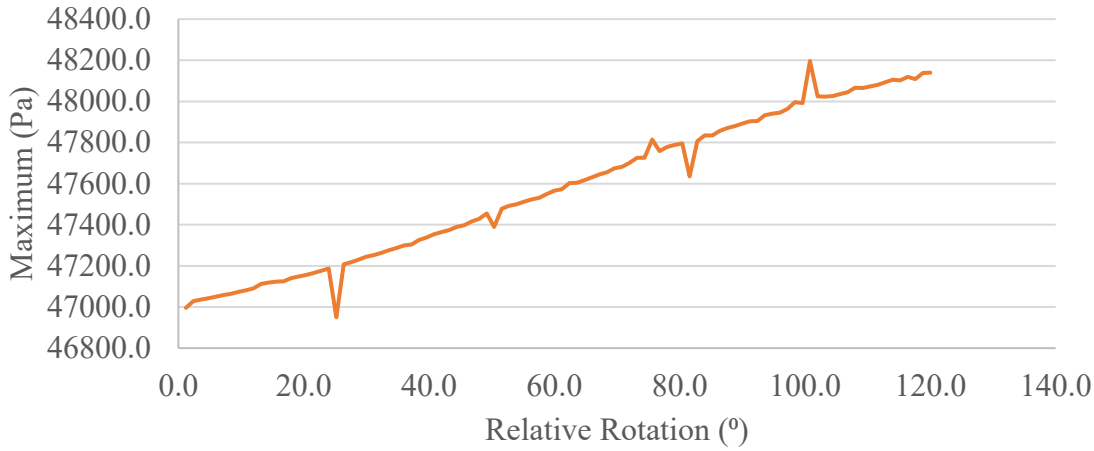

Fig. 115. Peak maximum shear stress data on proximal radius articular cartilage—elbow pronation at 120º/s.

Fig. 116 and Fig. 117 show the contour plots of von Mises stress and maximum shear stress acting on the proximal radius articular cartilage due to the forces exerted by synovial fluid during elbow pronation from 0º to 120º at a joint velocity of 120º/s.

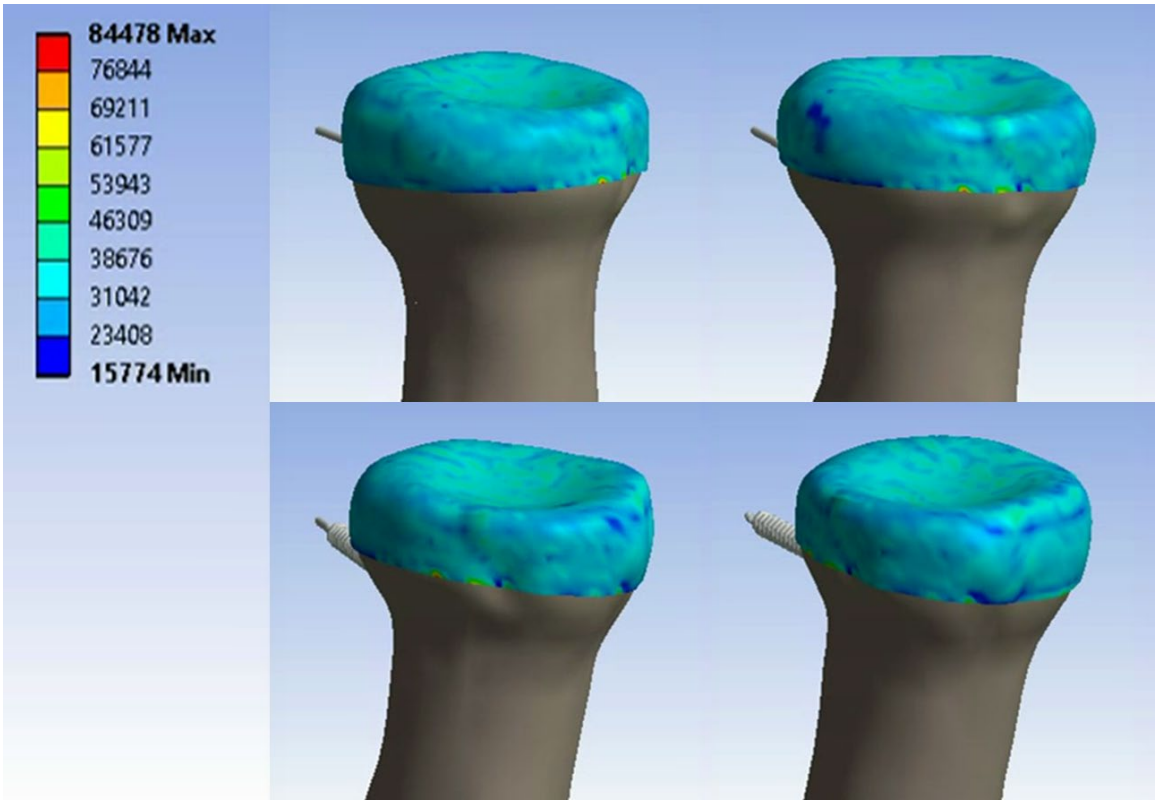

Fig. 116. Contour plot of von Mises stress on proximal radius articular cartilage—elbow pronation at 120º/s. The scale in the figure is represented in Pascals. The motion is starting from the top-left corner in the clockwise-direction and the snapshots were taken at approximately equidistant time intervals.

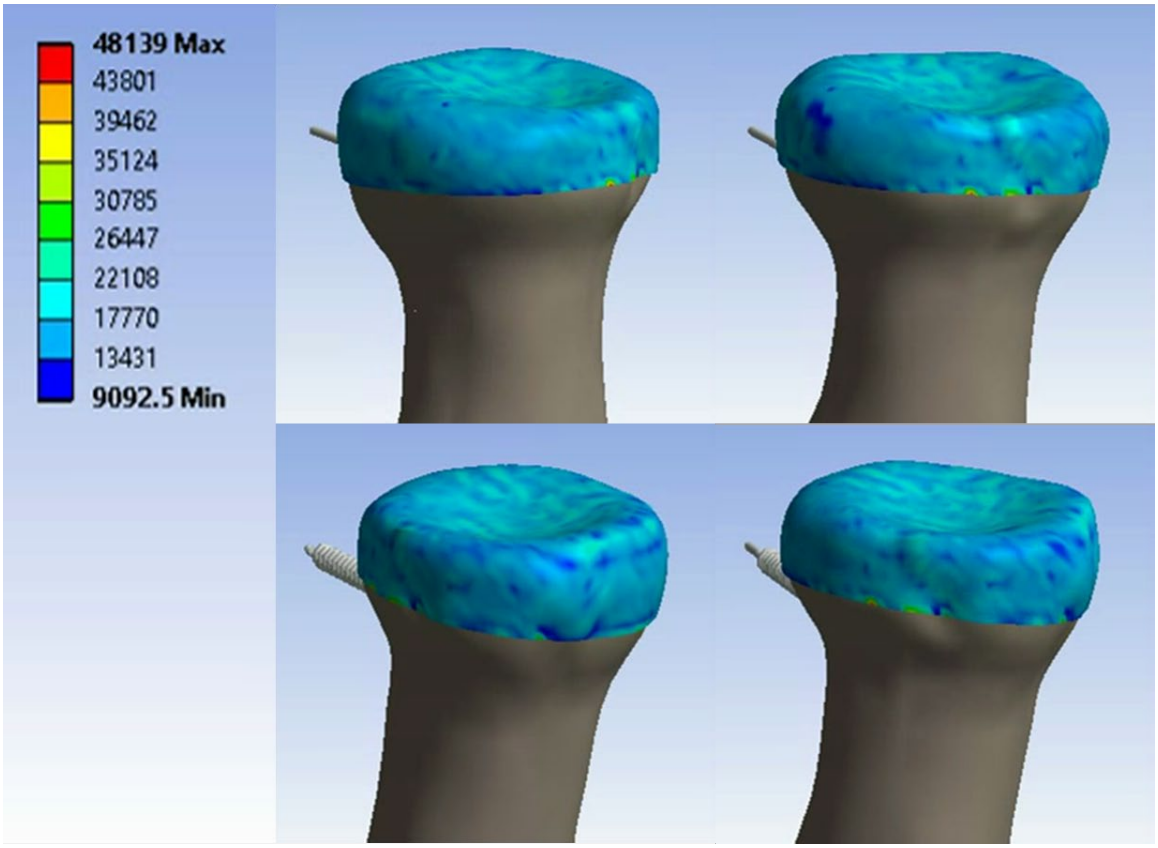

Fig. 117. Contour plot of maximum shear stress on proximal radius articular cartilage—elbow pronation at 120º/s. The scale in the figure is represented in Pascals. The motion is starting from the top-left corner in the clockwise-direction and the snapshots were taken at approximately equidistant time intervals.

Fig. 118 and Fig. 119 show the velocity streamlines of synovial fluid velocity near proximal radius articular cartilage during elbow pronation from 0º to 120º at a joint velocity of 120º/s in isometric and side views, respectively. Maximum synovial fluid velocity of 0.01 m/s was recorded.

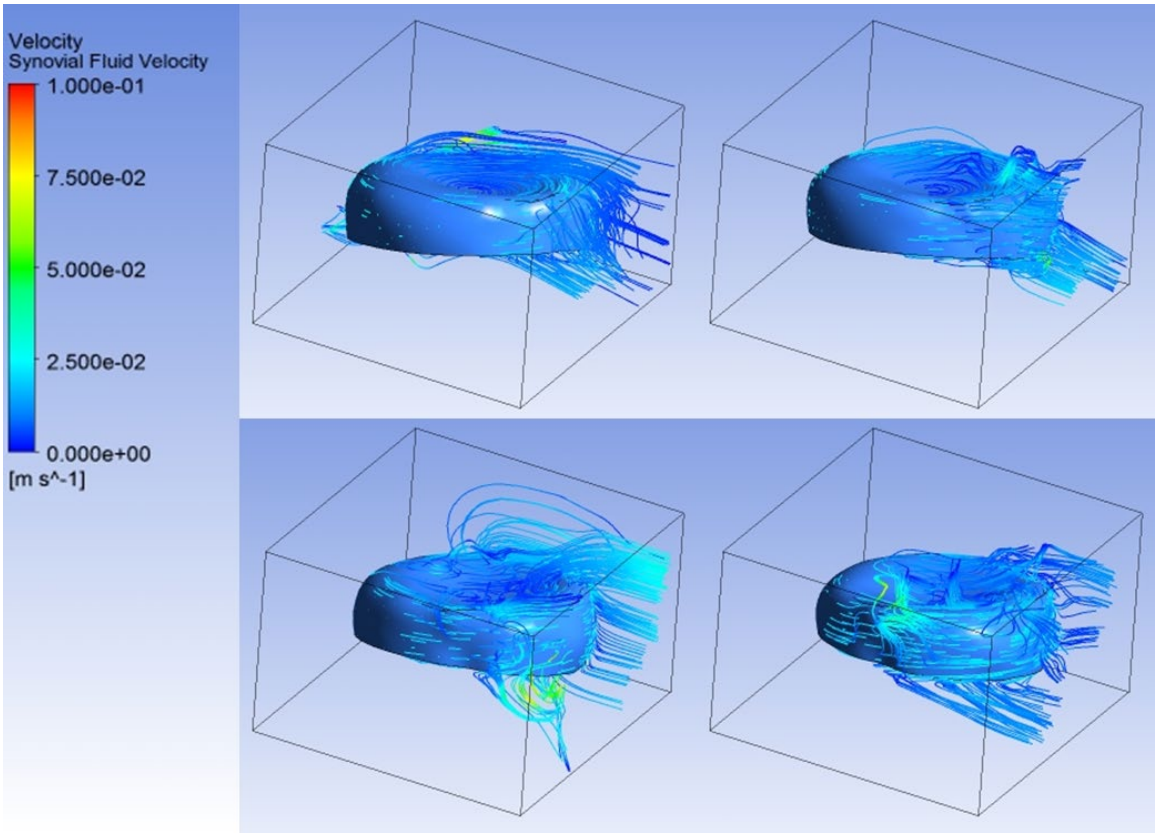

Fig. 118. Velocity streamlines of synovial fluid—elbow pronation at 120º/s (isometric view). The motion is starting from the top-left corner in the clockwise-direction and the snapshots were taken at approximately equidistant time intervals.

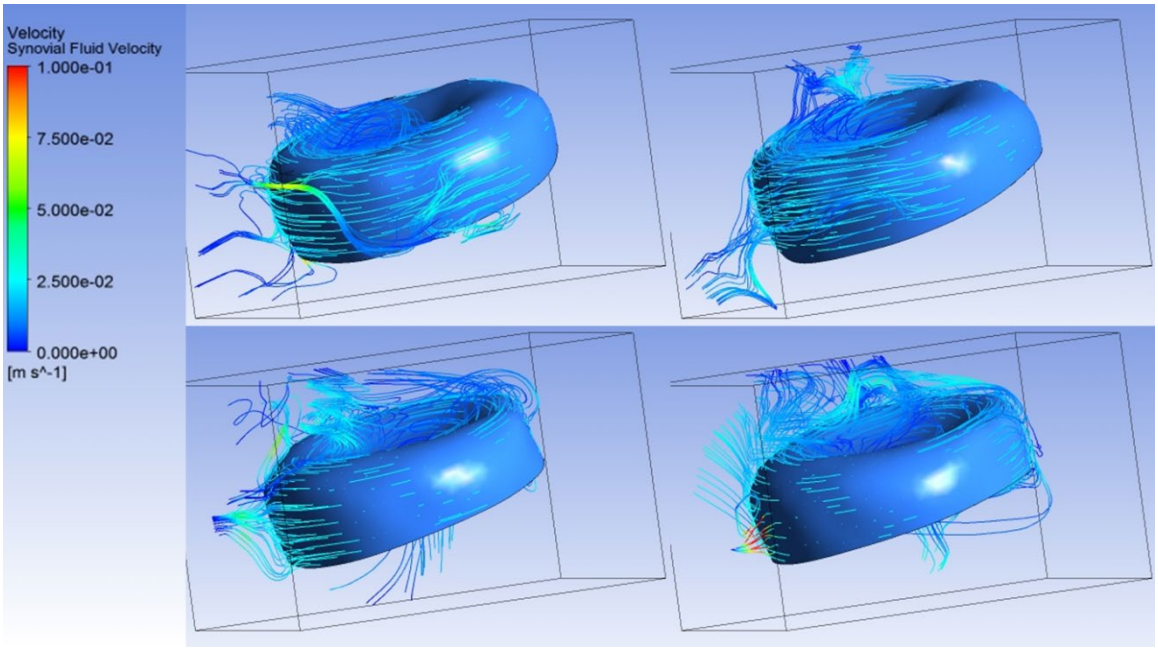

Fig. 119. Velocity streamlines of synovial fluid—elbow pronation at 120º/s (side view). The motion is starting from the top-left corner in the clockwise-direction and the snapshots were taken at approximately equidistant time intervals.

Fig. 120 shows that the mass-flow rate of synovial fluid at velocity inlet and pressure outlet is conserved during the full range of elbow pronation from 0º to 120º at a joint velocity of 120º/s.

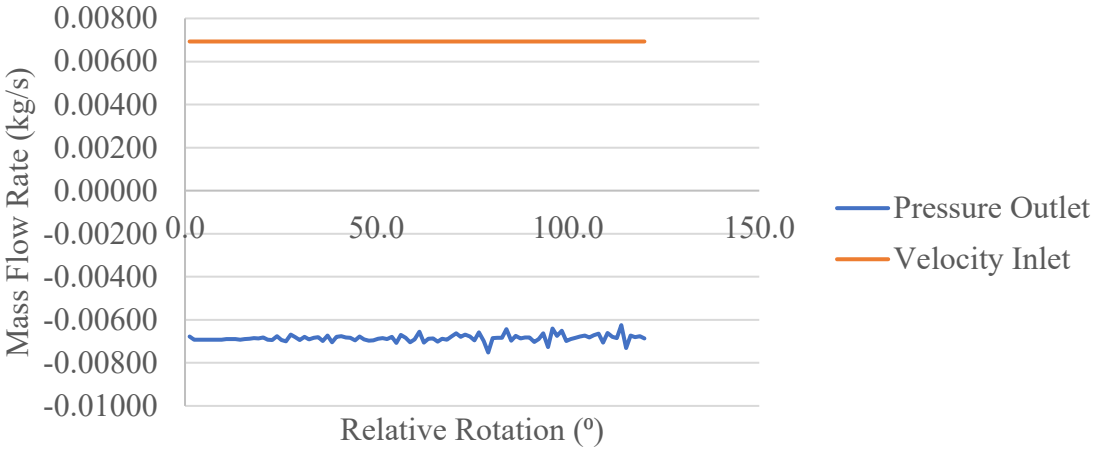

Fig. 120. Synovial fluid mass flow rate data—elbow pronation at 120º/s.

Fig. 121 shows the RMS change of data transfer of the structural displacement of proximal radius articular cartilage between ANSYS Transient Structural and ANSYS Fluent during the FSI simulation of elbow pronation from 0º to 120º at a joint velocity of 120º/s.

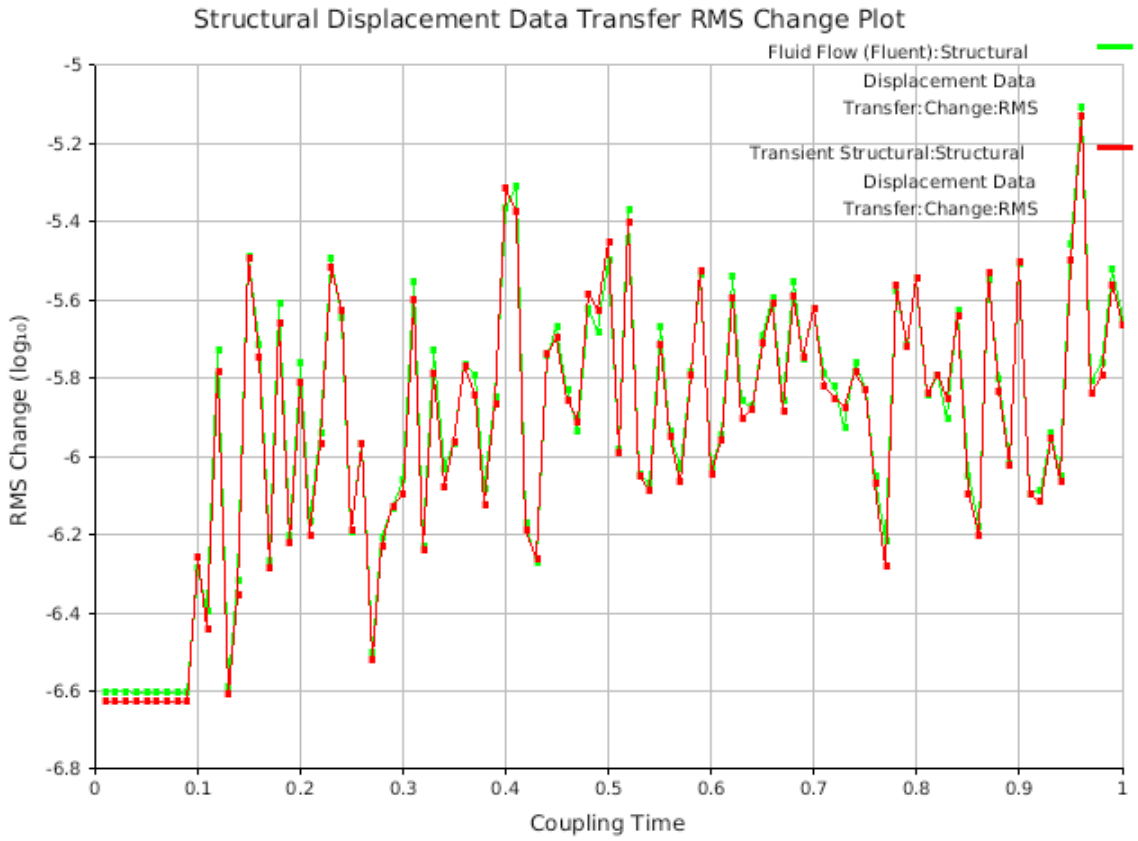

Fig. 121. Structural displacement data transfer RMS change plot—elbow pronation at 120º/s.

Fig. 122 shows the RMS change of data transfer of the synovial fluid forces acting on proximal radius articular cartilage between ANSYS Transient Structural and ANSYS Fluent during the FSI simulation of elbow pronation from 0º to 120º at a joint velocity of 120º/s.

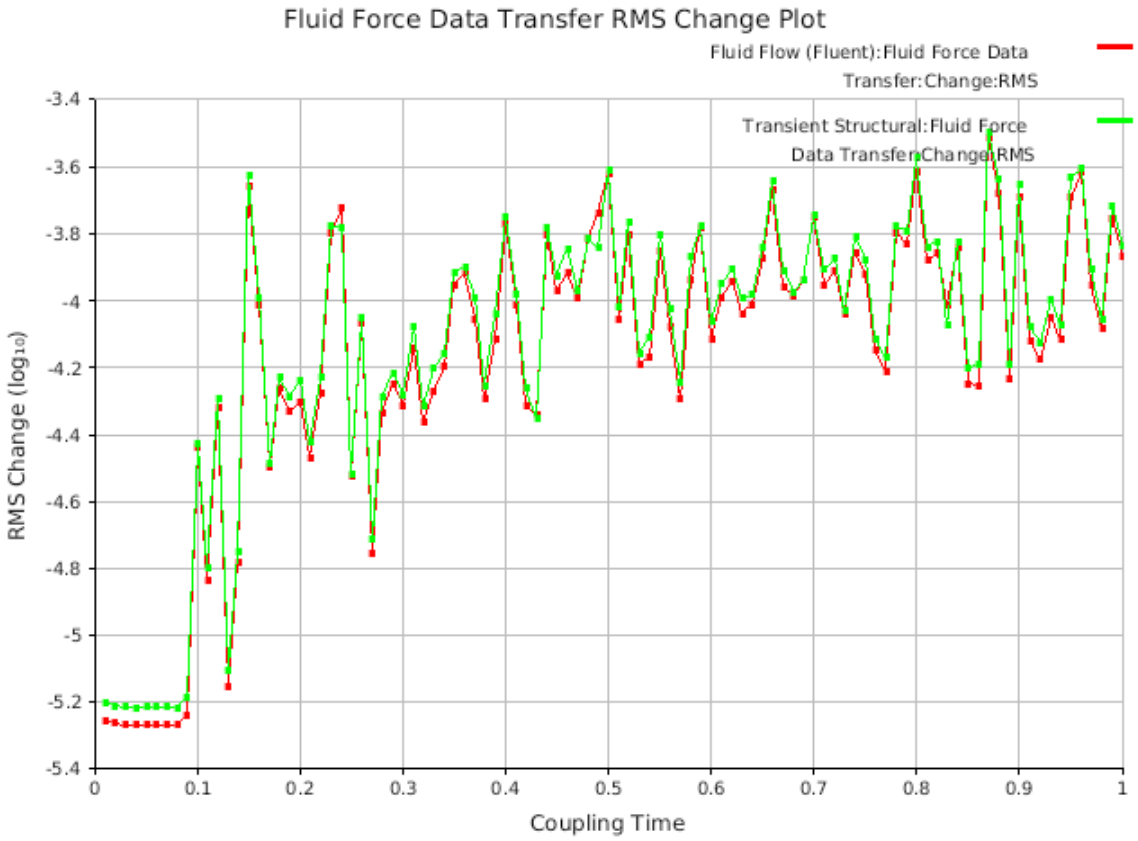

Fig. 122. Fluid force data transfer RMS change plot—elbow pronation at 120º/s.

4.9 Summary of Pronation Data

The computational elbow joint model for elbow pronation correlates well with the published elbow joint model [29] for both 40º/s and 120º/s joint velocity conditions.

For both 40º/s and 120º/s elbow extension conditions, peak loads of 447.83 N, and 50.52 N were observed for AL, and interosseous membrane, respectively.

The peak von Mises stress and peak maximum shear stress acting on the proximal radius articular cartilage was determined to be 0.0085 MPa and 0.0048 MPa, respectively for both 40º/s and 120º/s elbow pronation conditions.

During the slower 40º/s elbow pronation, synovial fluid flow was predominantly laminar with a maximum velocity of 0.002 m/s. However, during the faster, 120º/s elbow pronation, synovial fluid flow exhibited turbulence with a maximum velocity of 0.01 m/s which is equal to the inlet velocity of the fluid domain.

4.10 Supination at 40º/s

Fig. 123 shows the relationship between constraint moment generated by elbow supinators and ligaments, elastic moment generated by elbow supinators stiffness, and total moment generated at the elbow joint during elbow supination from 120º to 0º at a joint velocity of 40º/s. Comparing the constraint moment and elastic moment curves in Fig. 123 with the elbow supinators moment curve (bold, black curve labeled as 'model') in Fig. 15, shows that the elbow joint model developed in this FSI simulation correlates well with the published elbow joint model [29].

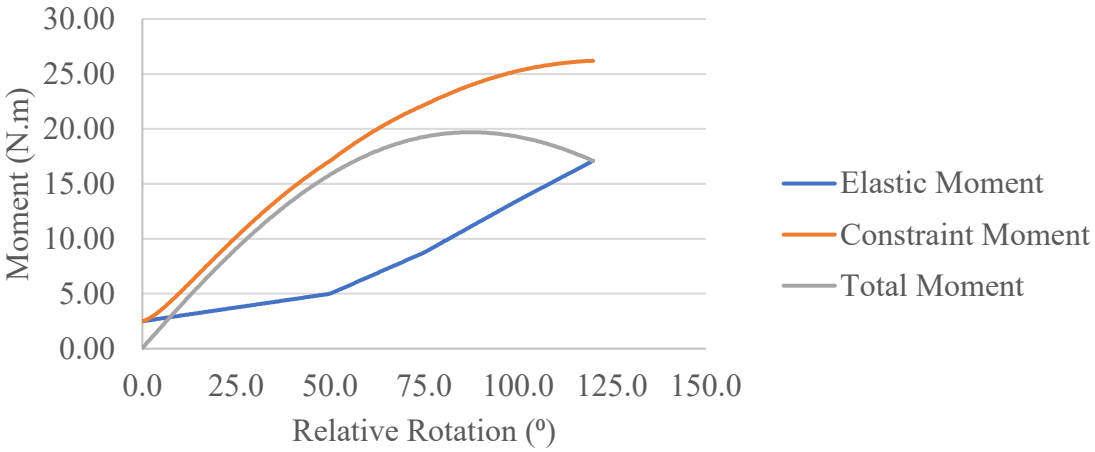

Fig. 123. Joint moment vs. rotation data—elbow supination at 40º/s.

Fig. 124 and Fig. 125 provides the ligament load data with respect to elbow supination angle during elbow supination from 120º to 0º at a joint velocity of 40º/s. Peak loads of 447.83 N, and 50.52 N were observed for AL, and interosseous membrane, respectively.

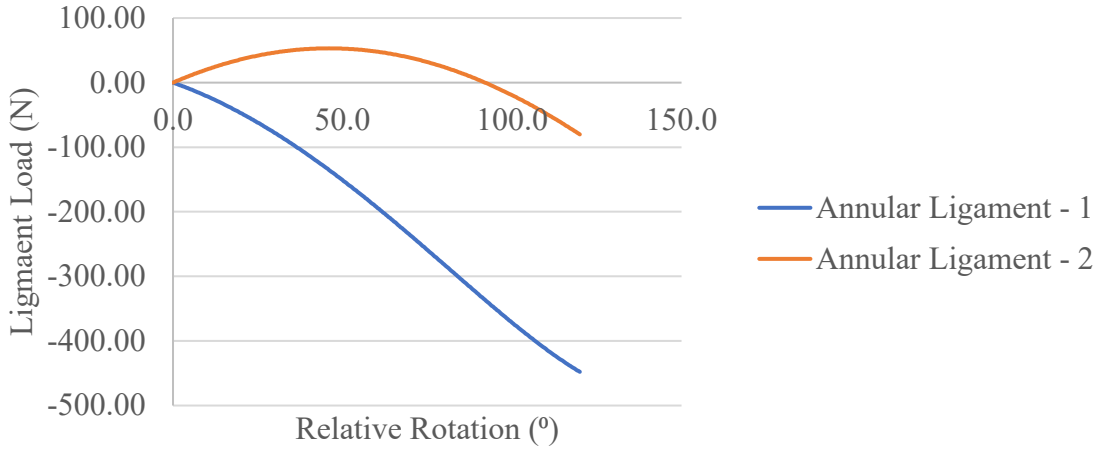

Fig. 124. Ligament (AL) load data—elbow supination at 40º/s.

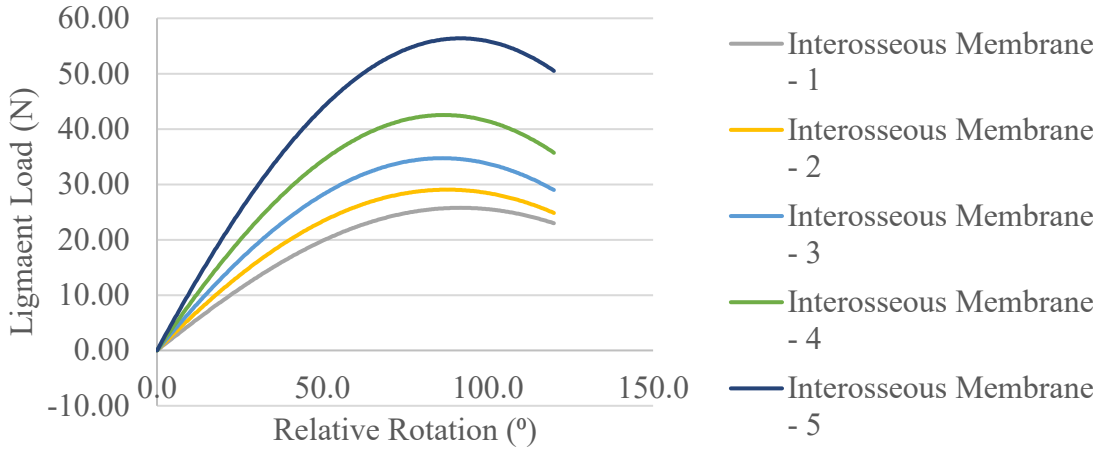

Fig. 125. Ligament (interosseous membrane) load data—elbow supination at 40º/s.

Fig. 126 and Fig. 127 show the relationship between the peak von Mises stress and peak maximum shear stress acting on the proximal radius articular cartilage due to the forces exerted by synovial fluid with respect to supination angle during elbow supination from 120º to 0º at a joint velocity of 40º/s. Peak von Mises stress of 64,729 Pa or 0.0065 MPa, and peak maximum shear stress of 36,087 Pa or 0.0036 MPa were recorded to be acting on proximal radius articular cartilage at maximum elbow supination of 120º.

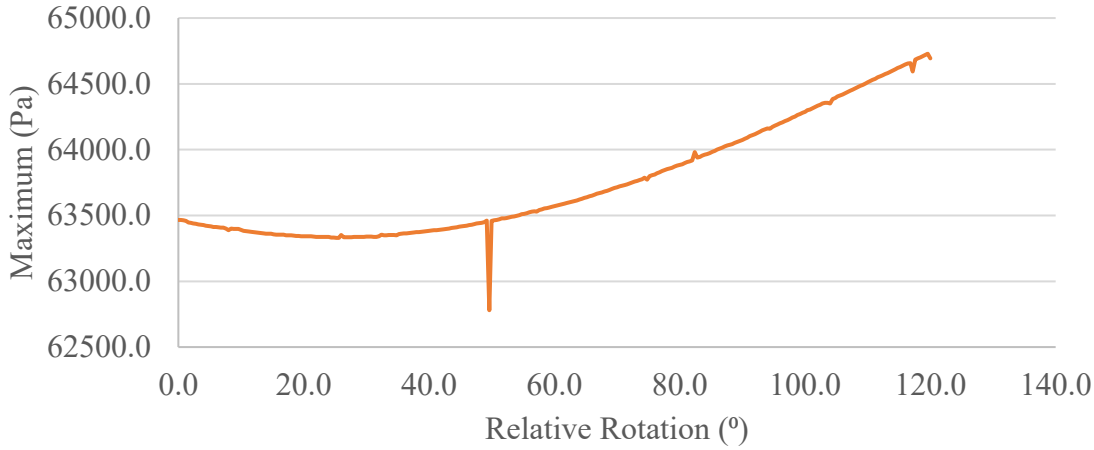

Fig. 126. Peak von Mises stress data on proximal radius articular cartilage—elbow supination at 40º/s.

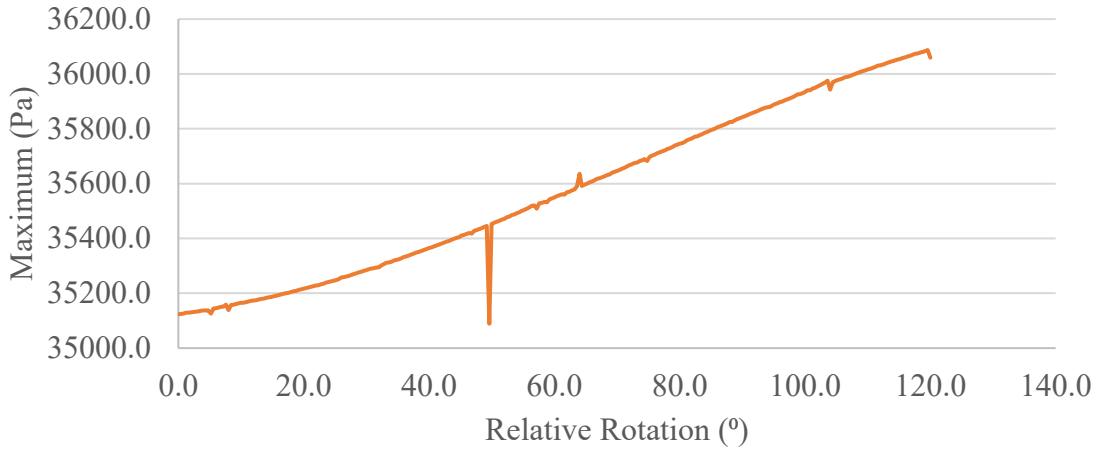

Fig. 127. Peak maximum shear stress data on proximal radius articular cartilage—elbow supination at 40º/s.

Fig. 128 and Fig. 129 show the contour plots of von Mises stress and maximum shear stress acting on the proximal radius articular cartilage due to the forces exerted by synovial fluid during elbow supination from 120º to 0º at a joint velocity of 40º/s.

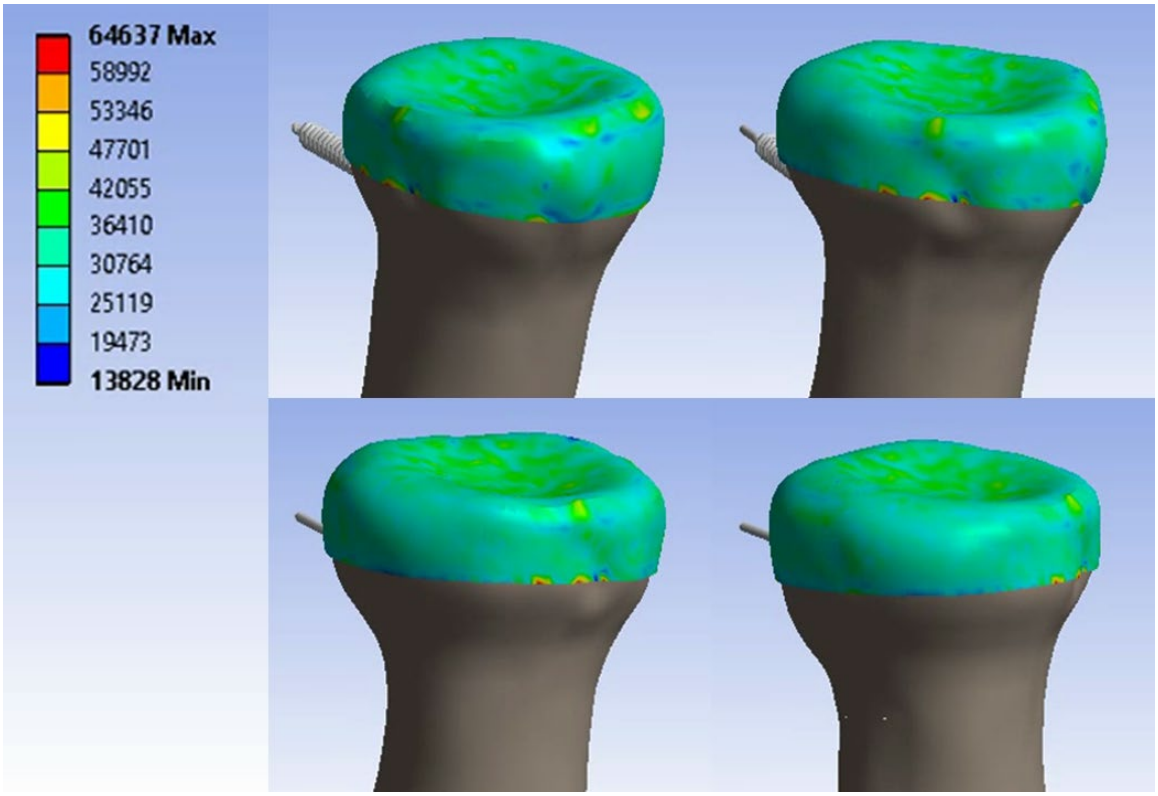

Fig. 128. Contour plot of von Mises stress on proximal radius articular cartilage—elbow supination at 40º/s. The scale in the figure is represented in Pascals. The motion is starting from the top-left corner in the clockwise-direction and the snapshots were taken at approximately equidistant time intervals.

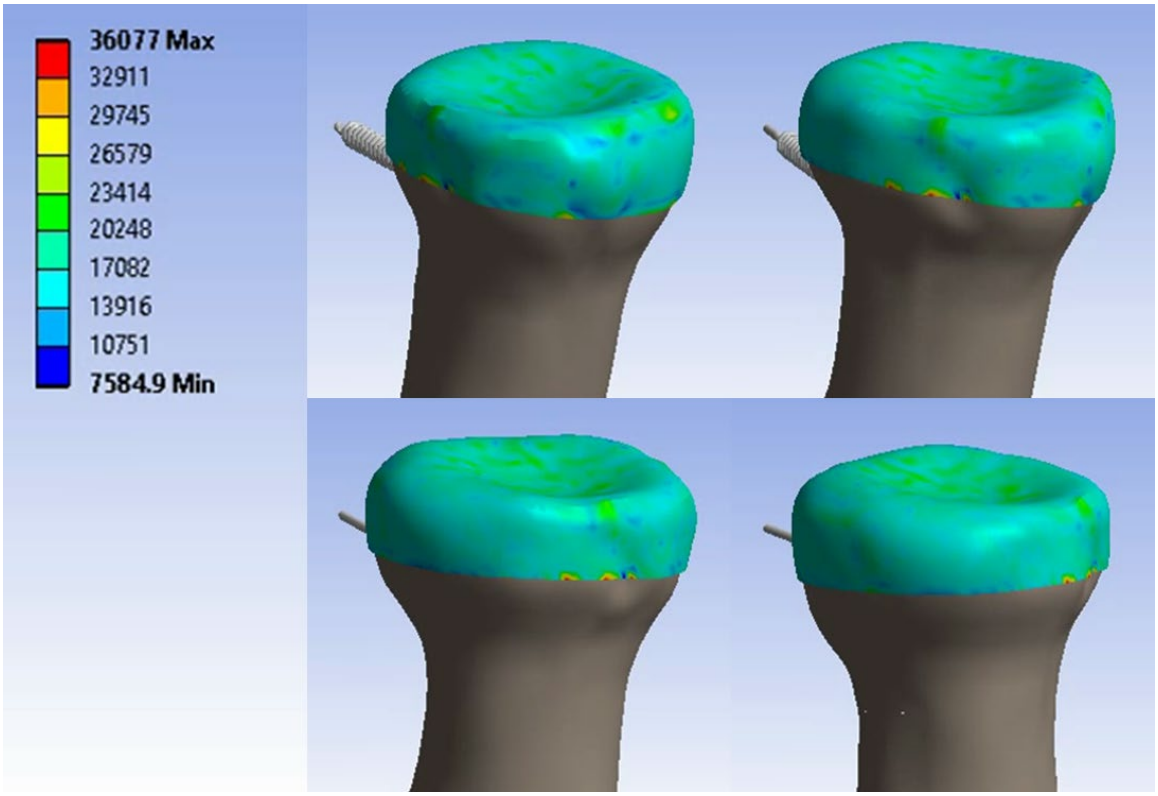

Fig. 129. Contour plot of maximum shear stress on proximal radius articular cartilage—elbow supination at 40º/s. The scale in the figure is represented in Pascals. The motion is starting from the top-left corner in the clockwise-direction and the snapshots were taken at approximately equidistant time intervals.

Fig. 130 and Fig. 131 show the velocity streamlines of synovial fluid velocity near proximal radius articular cartilage during elbow supination from 120º to 0º at a joint velocity of 40º/s in isometric and side views, respectively. Maximum synovial fluid velocity of 0.002 m/s was recorded.

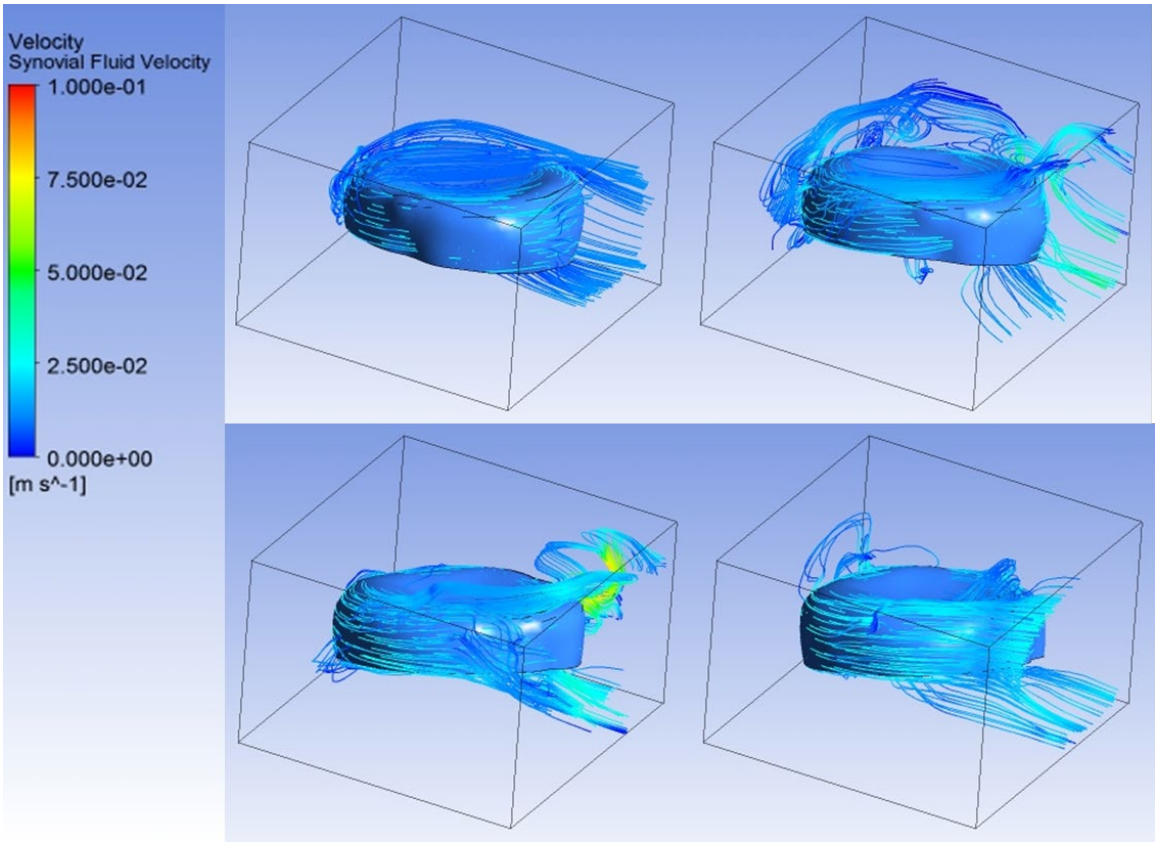

Fig. 130. Velocity streamlines of synovial fluid—elbow supination at 40º/s (isometric view). The motion is starting from the top-left corner in the clockwise-direction and the snapshots were taken at approximately equidistant time intervals.

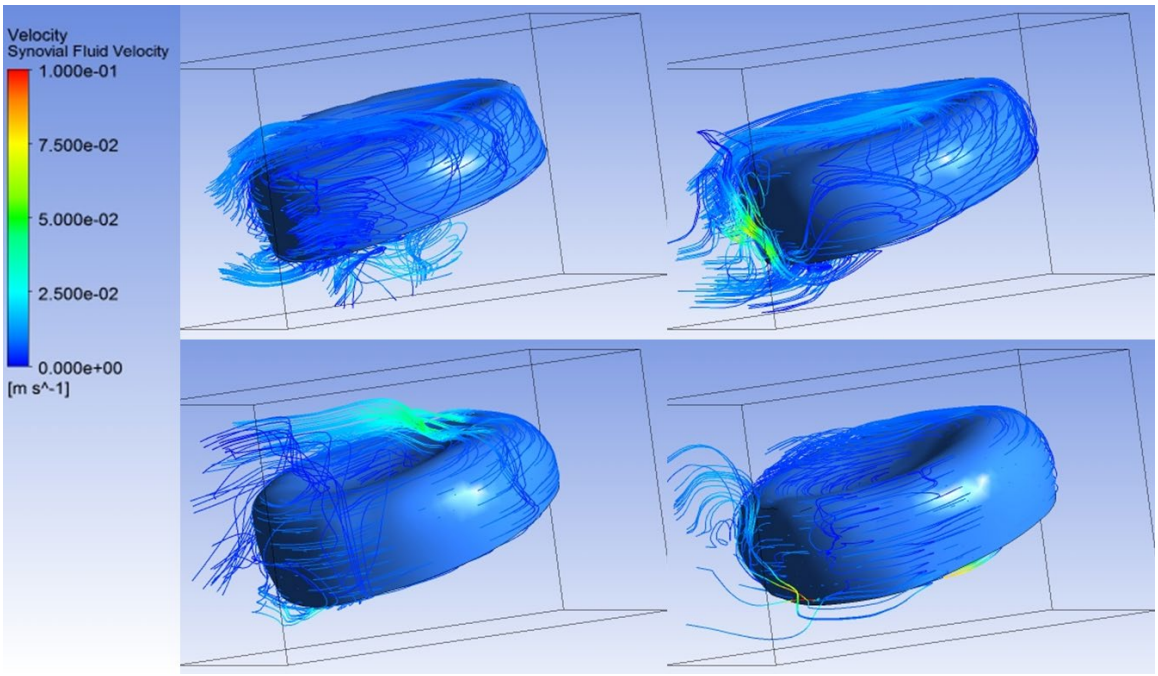

Fig. 131. Velocity streamlines of synovial fluid—elbow supination at 40º/s (side view). The motion is starting from the top-left corner in the clockwise-direction and the snapshots were taken at approximately equidistant time intervals.

Fig. 132 shows that the mass-flow rate of synovial fluid at velocity inlet and pressure outlet is conserved during the full range of elbow supination from 120º to 0º at a joint velocity of 40º/s.

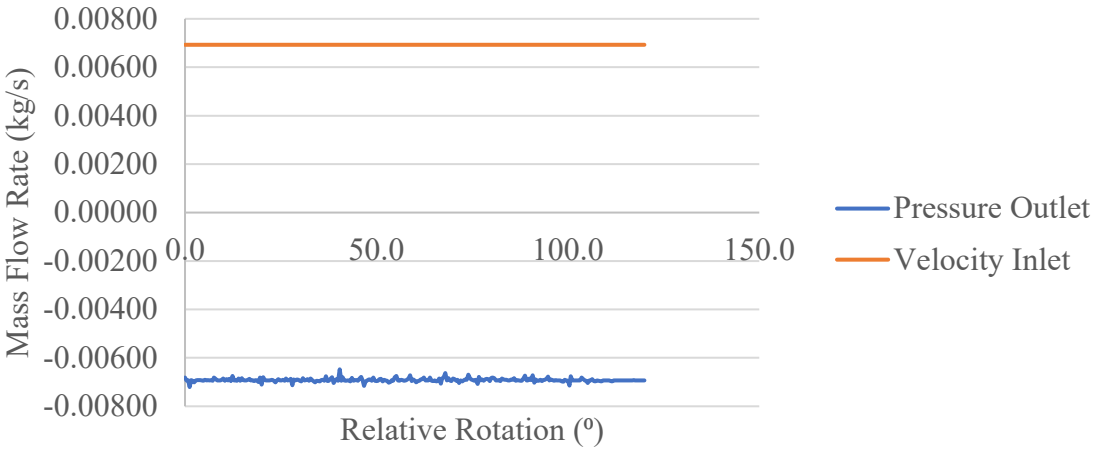

Fig. 132. Synovial fluid mass flow rate data—elbow supination at 40º/s.

Fig. 133 shows the RMS change of data transfer of the structural displacement of proximal radius articular cartilage between ANSYS Transient Structural and ANSYS Fluent during the FSI simulation of elbow supination from 120º to 0º at a joint velocity of 40º/s.

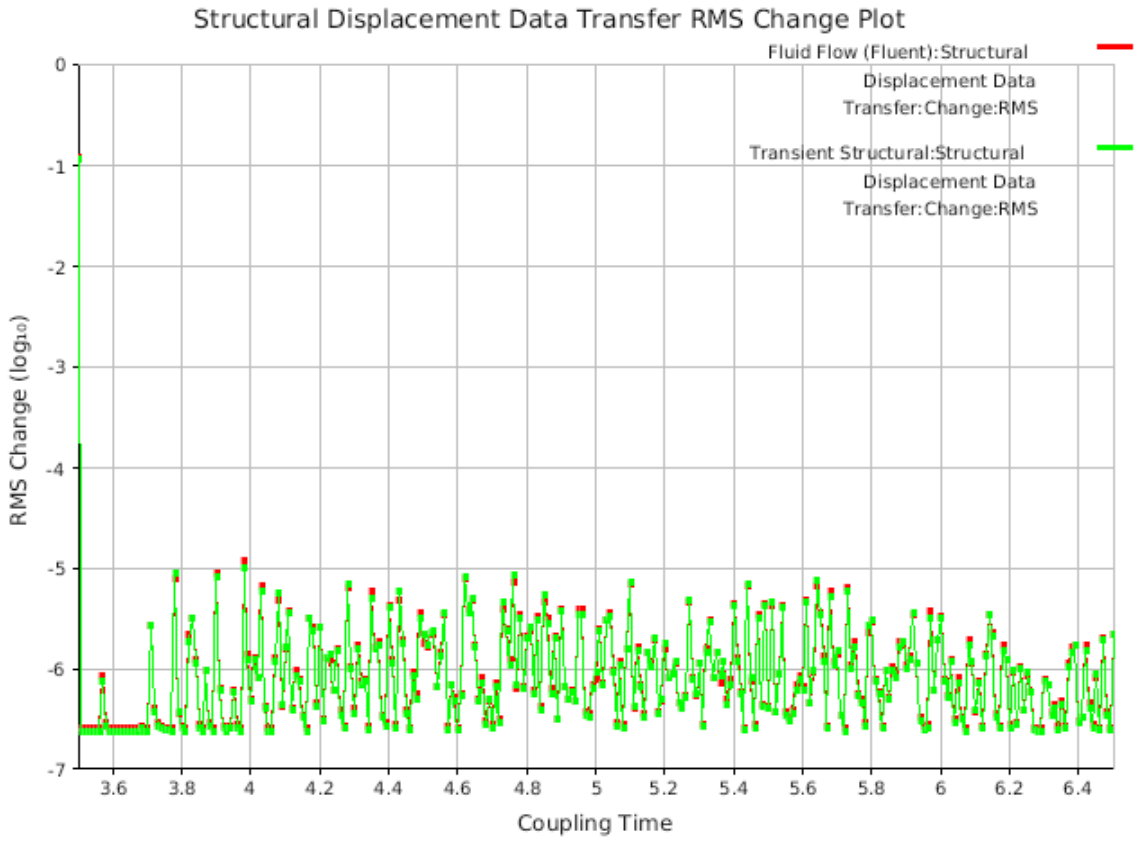

Fig. 133. Structural displacement data transfer RMS change plot—elbow supination at 40º/s.

Fig. 134 shows the RMS change of data transfer of the synovial fluid forces acting on proximal radius articular cartilage between ANSYS Transient Structural and ANSYS Fluent during the FSI simulation of elbow supination from 120º to 0º at a joint velocity of 40º/s.

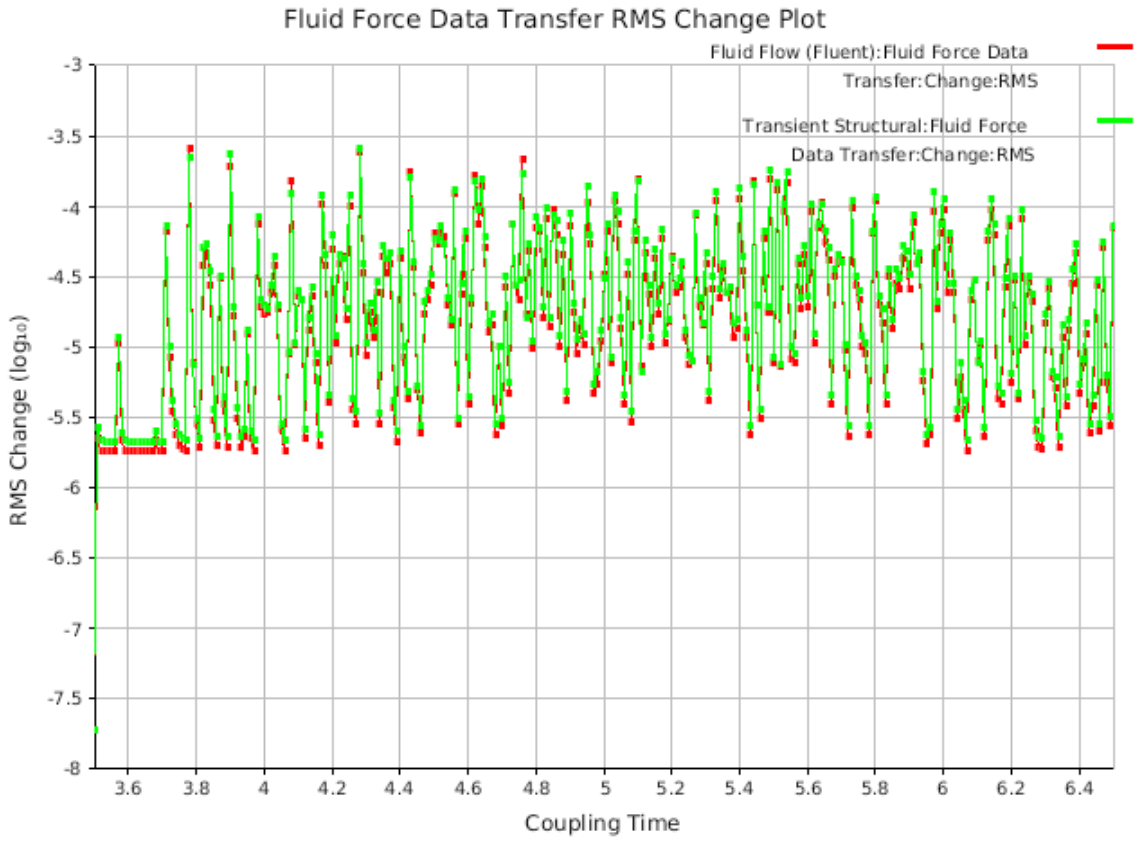

Fig. 134. Fluid force data transfer RMS change plot—elbow supination at 40º/s.

4.11 Supination at 120º/s

Fig. 135 shows the relationship between constraint moment generated by elbow supinators and ligaments, elastic moment generated by elbow supinators stiffness, and total moment generated at the elbow joint during elbow supination from 120º to 0º at a joint velocity of 120º/s. Comparing the constraint moment and elastic moment curves in Fig. 135 with the elbow supinators moment curve (bold, black curve labeled as 'model') in Fig. 15, shows that the elbow joint model developed in this FSI simulation correlates well with the published elbow joint model [29].

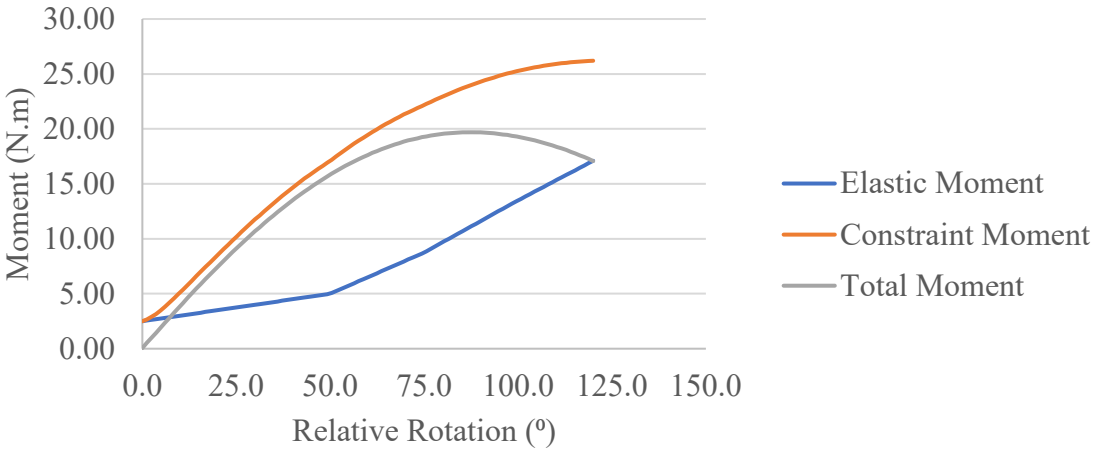

Fig. 135. Joint moment vs. rotation data—elbow supination at 120º/s.

Fig. 136 and Fig. 137 provides the ligament load data with respect to elbow supination angle during elbow supination from 120º to 0º at a joint velocity of 120º/s. Peak loads of 447.83 N, and 50.52 N were observed for AL, and interosseous membrane, respectively.

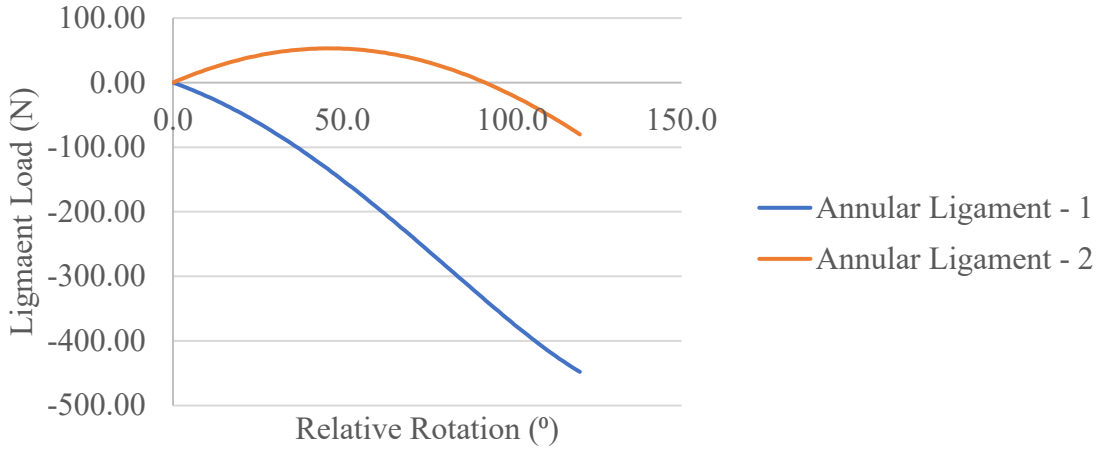

Fig. 136. Ligament (AL) load data—elbow supination at 120º/s.

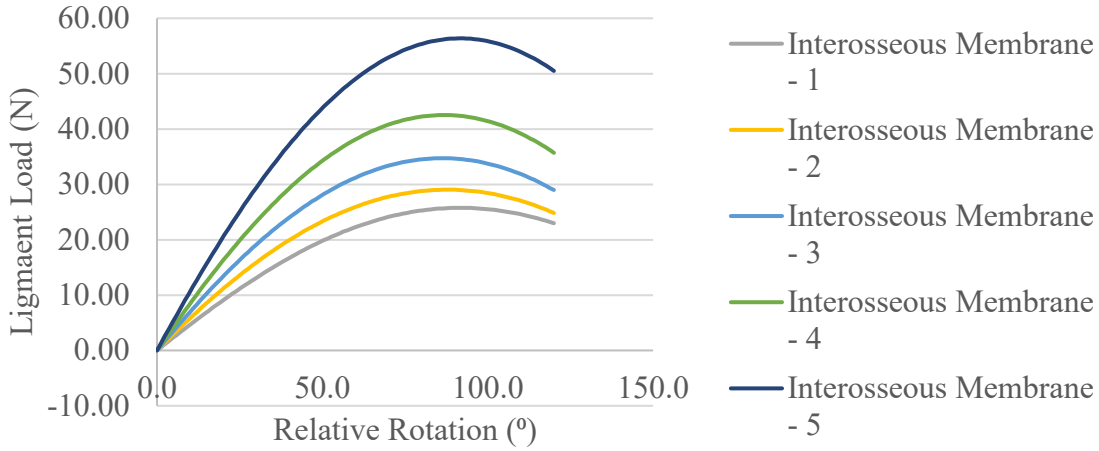

Fig. 137. Ligament (interosseous membrane) load data—elbow supination at 120º/s.

Fig. 138 and Fig. 139 show the relationship between the peak von Mises stress and peak maximum shear stress acting on the proximal radius articular cartilage due to the forces exerted by synovial fluid with respect to supination angle during elbow supination from 120º to 0º at a joint velocity of 120º/s. Peak von Mises stress of 64,700 Pa or 0.0065 MPa, and peak maximum shear stress of 36,067 Pa or 0.0036 MPa were recorded to be acting on proximal radius articular cartilage.

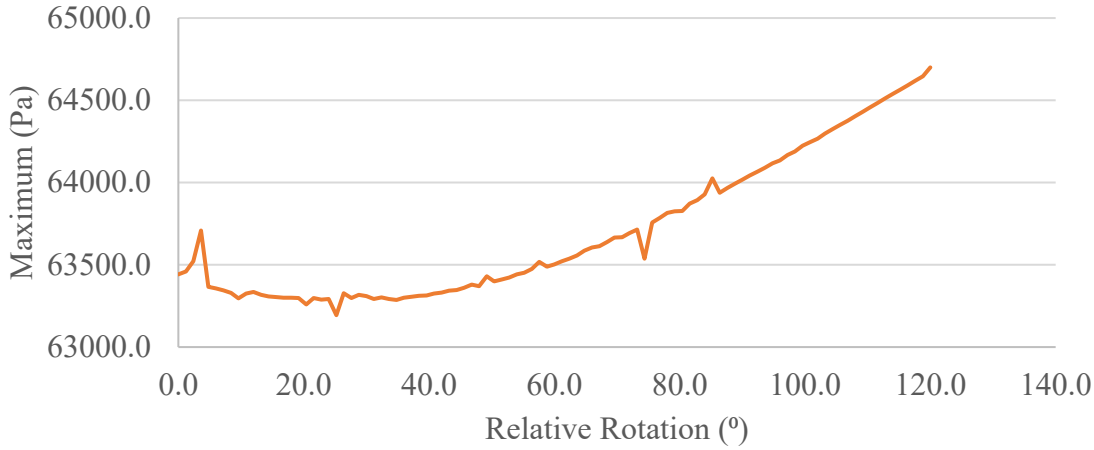

Fig. 138. Peak von Mises stress data on proximal radius articular cartilage—elbow supination at 120º/s.

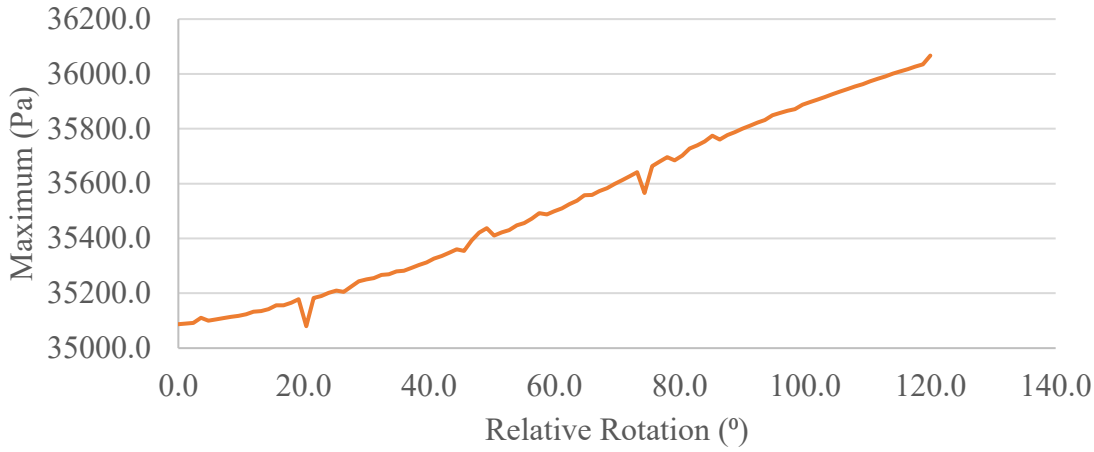

Fig. 139. Peak maximum shear stress data on proximal radius articular cartilage—elbow supination at 120º/s.

Fig. 140 and Fig. 141 show the contour plots of von Mises stress and maximum shear stress acting on the proximal radius articular cartilage due to the forces exerted by synovial fluid during elbow supination from 120º to 0º at a joint velocity of 120º/s.

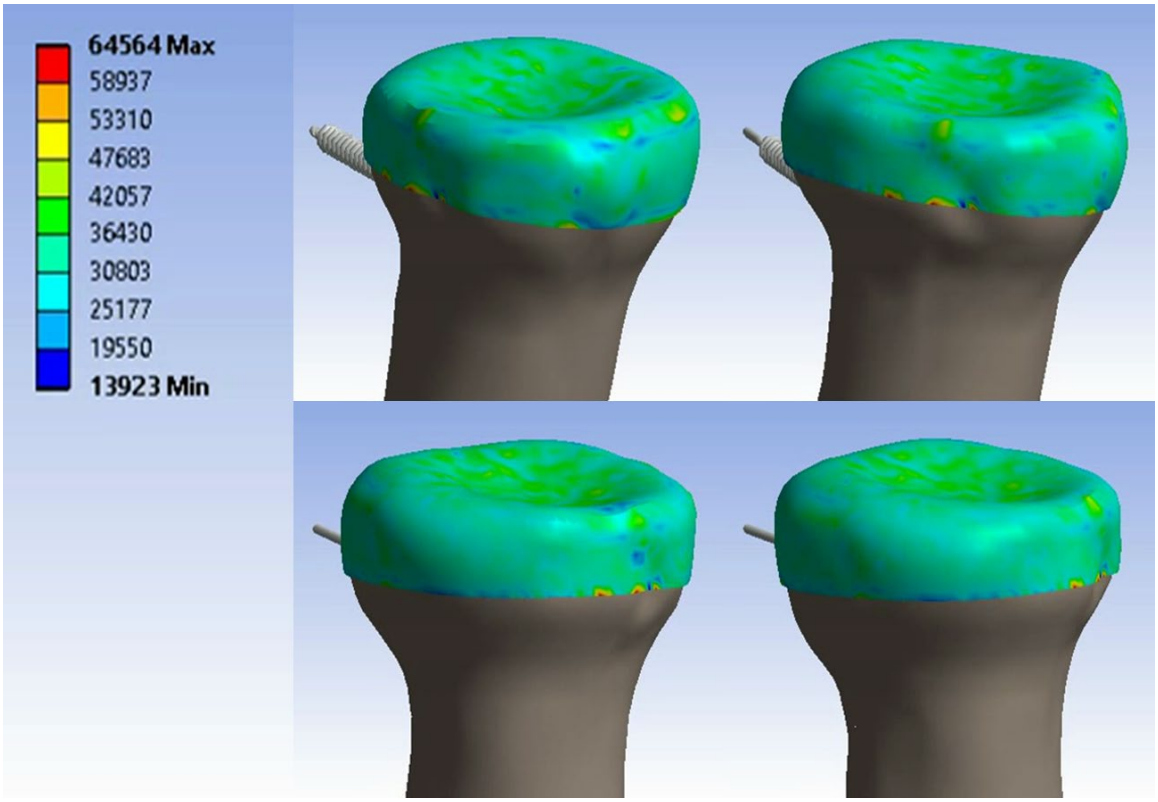

Fig. 140. Contour plot of von Mises stress on proximal radius articular cartilage—elbow supination at 120º/s. The scale in the figure is represented in Pascals. The motion is starting from the top-left corner in the clockwise-direction and the snapshots were taken at approximately equidistant time intervals.

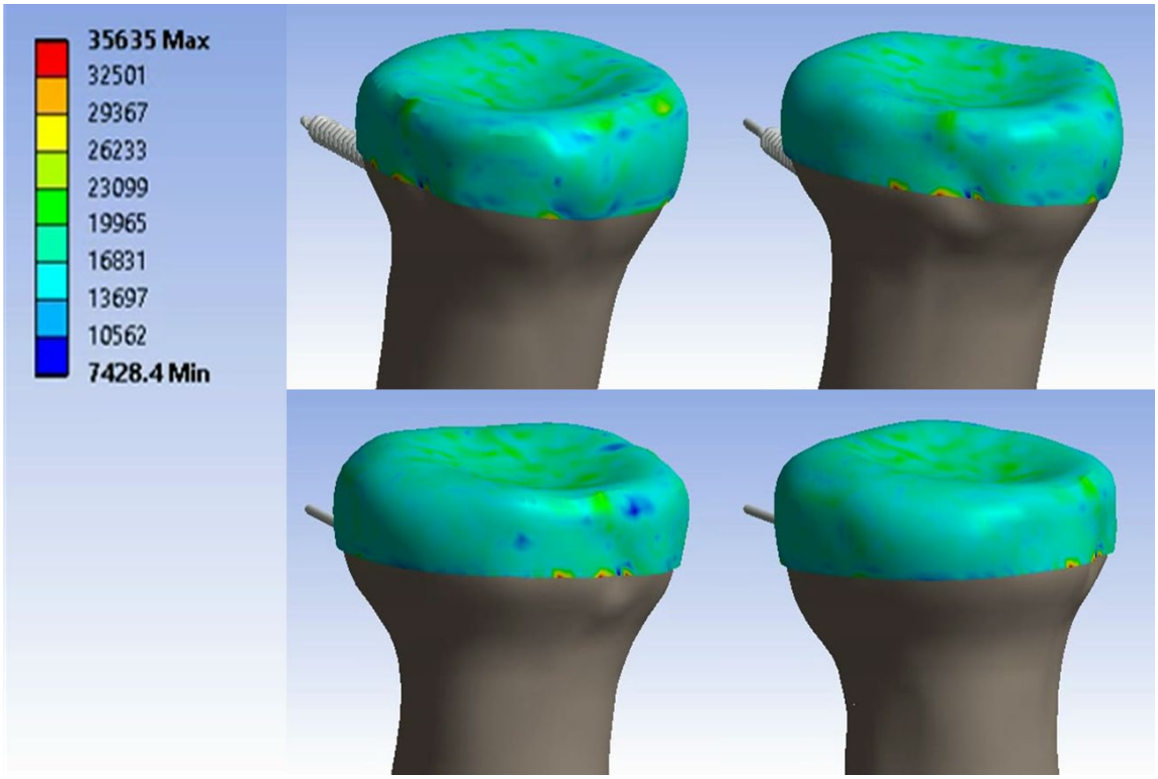

Fig. 141. Contour plot of maximum shear stress on proximal radius articular cartilage—elbow supination at 120º/s. The scale in the figure is represented in Pascals. The motion is starting from the top-left corner in the clockwise-direction and the snapshots were taken at approximately equidistant time intervals.

Fig. 142 and Fig. 143 show the velocity streamlines of synovial fluid velocity near proximal radius articular cartilage during elbow supination from 120º to 0º at a joint velocity of 120º/s in isometric and side views, respectively. Maximum synovial fluid velocity of 0.01 m/s was recorded.

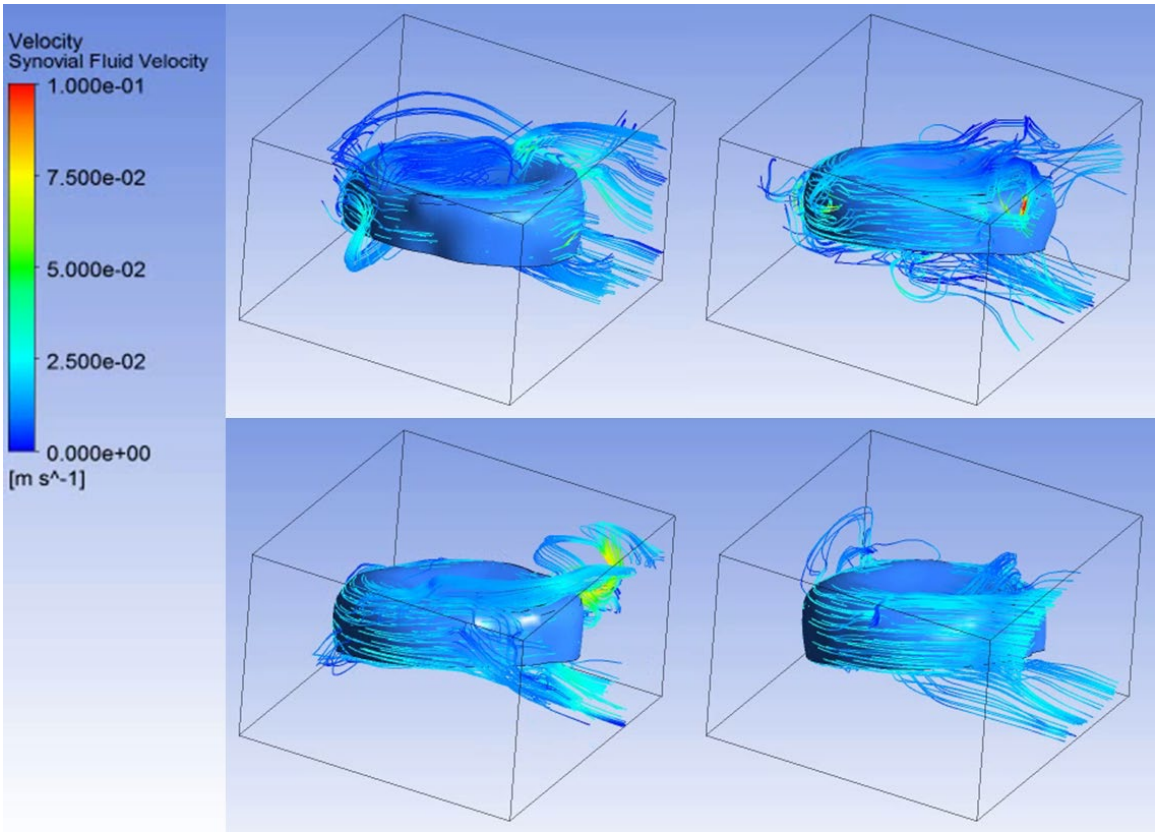

Fig. 142. Velocity streamlines of synovial fluid—elbow supination at 120º/s (isometric view). The motion is starting from the top-left corner in the clockwise-direction and the snapshots were taken at approximately equidistant time intervals.

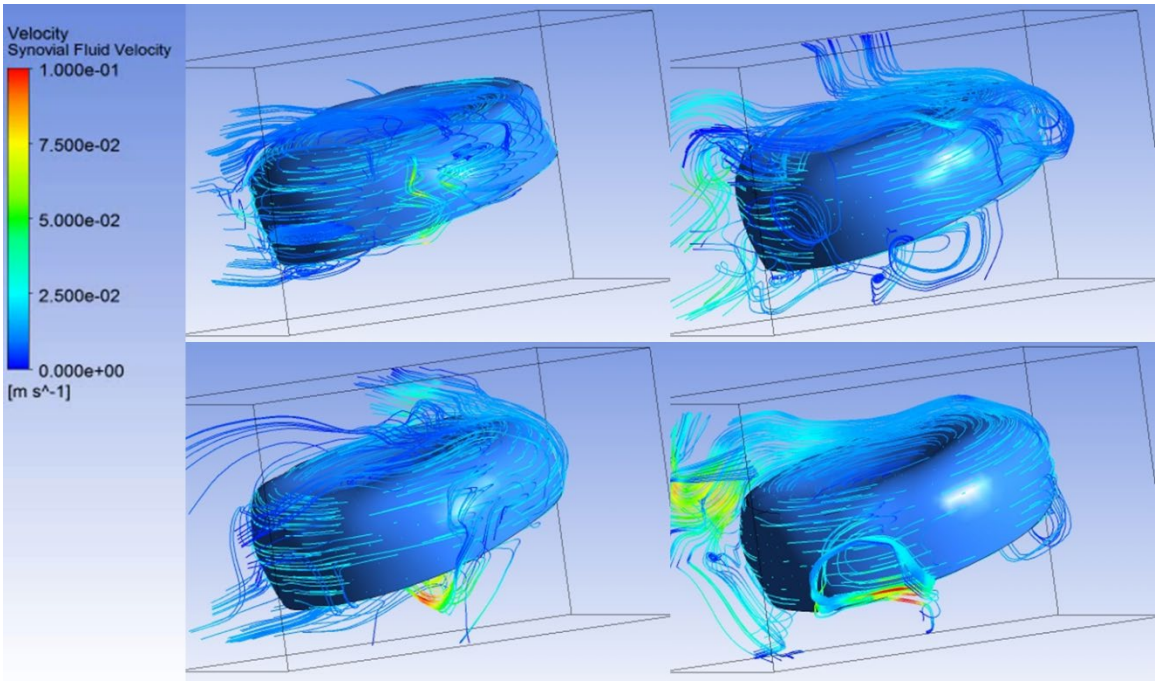

Fig. 143. Velocity streamlines of synovial fluid—elbow supination at 120º/s (side view). The motion is starting from the top-left corner in the clockwise-direction and the snapshots were taken at approximately equidistant time intervals.

Fig. 144 shows that the mass-flow rate of synovial fluid at velocity inlet and pressure outlet is conserved during the full range of elbow supination from 120º to 0º at a joint velocity of 120º/s.

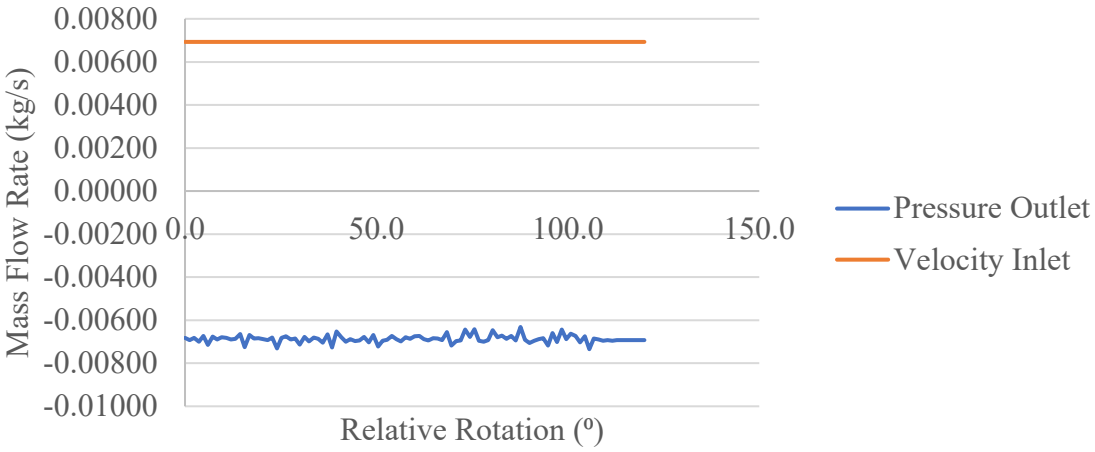

Fig. 144. Synovial fluid mass flow rate data—elbow supination at 120º/s.

Fig. 145 shows the RMS change of data transfer of the structural displacement of proximal radius articular cartilage between ANSYS Transient Structural and ANSYS Fluent during the FSI simulation of elbow supination from 120º to 0º at a joint velocity of 120º/s.

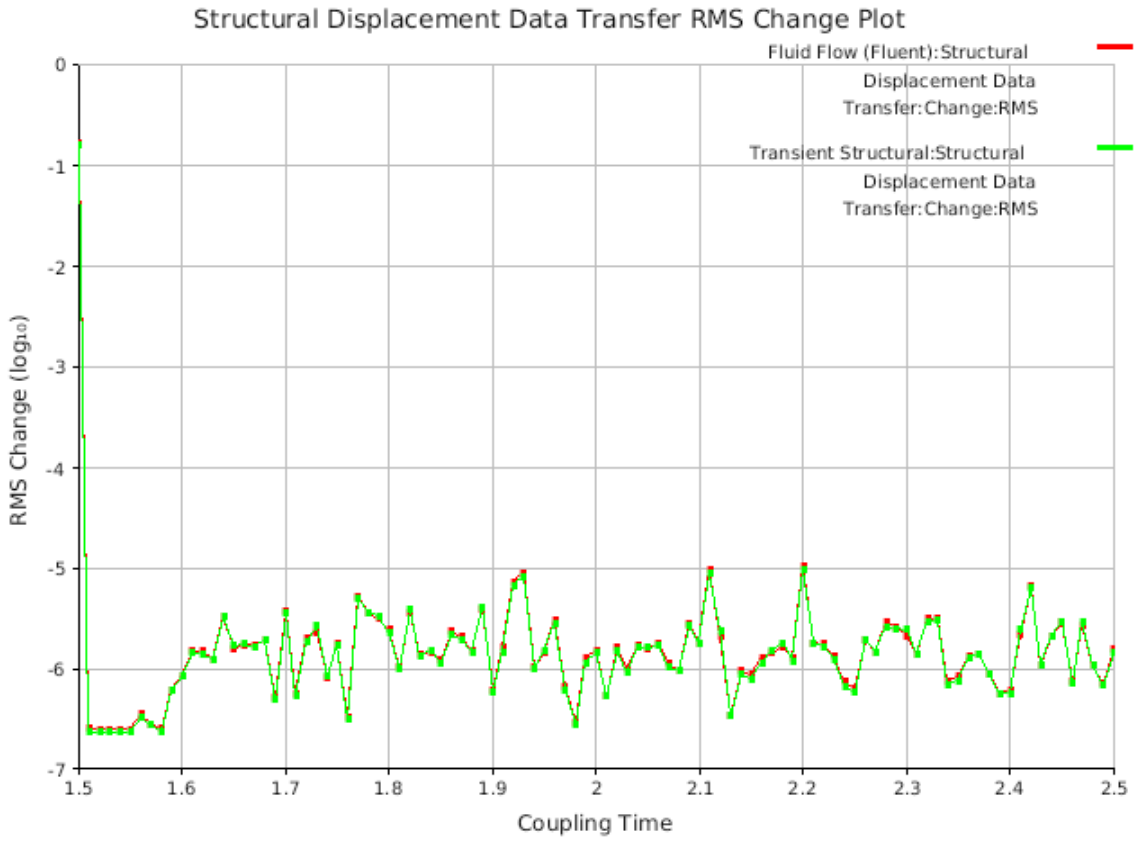

Fig. 145. Structural displacement data transfer RMS change plot—elbow supination at 120º/s.

Fig. 146 shows the RMS change of data transfer of the synovial fluid forces acting on proximal radius articular cartilage between ANSYS Transient Structural and ANSYS Fluent during the FSI simulation of elbow supination from 120º to 0º at a joint velocity of 120º/s.

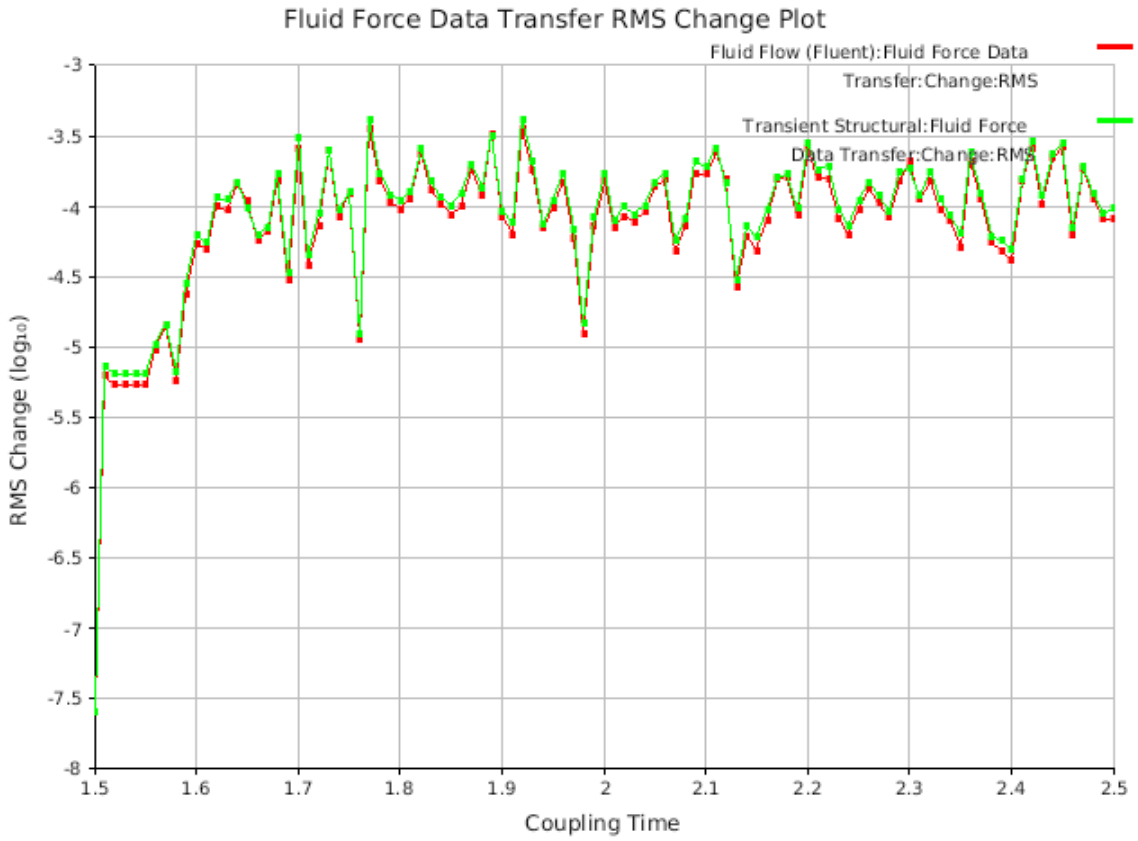

Fig. 146. Fluid force data transfer RMS change plot—elbow supination at 120º/s.

4.12 Summary of Supination Data

The computational elbow joint model for elbow supination correlates well with the published elbow joint model [29] for both 40º/s and 120º/s joint velocity conditions.

For both 40º/s and 120º/s elbow extension conditions, peak loads of 447.83 N, and 50.52 N were observed for AL, and interosseous membrane, respectively.

The peak von Mises stress and peak maximum shear stress acting on the proximal radius articular cartilage was determined to be 0.0085 MPa and 0.0048 MPa, respectively for both 40º/s and 120º/s elbow supination conditions.

During the slower 40º/s elbow supination, synovial fluid flow was predominantly laminar with a maximum velocity of 0.002 m/s. However, during the faster, 120º/s elbow supination, synovial fluid flow exhibited turbulence with a maximum velocity of 0.01 m/s which is equal to the inlet velocity of the fluid domain.

5 DISCUSSION

The peak von Mises stresses found using the computational elbow joint model developed in this study are 0.0073 MPa on proximal ulna articular cartilage during flexion-extension, and 0.0085 MPa on proximal radius articular cartilage during pronation-supination. M Rahman et al. reported a peak contact pressure of 3.7 MPa for 10º/s joint motion, 4.2 MPa for 60º/s joint motion, and 5.5 MPa for free velocity joint motion, on medial cartilage during elbow flexion [6]. Data for peak contact pressures during elbow extension, pronation, and supination was not published. This significant difference in articular cartilage stresses can be attributed to the presence of synovial fluid between articular cartilages in this elbow joint model compared to the assumption of solid-solid contact between articular cartilages in the model developed by M Rahman et al. [6]. Nevertheless, any comparison of cartilage stresses found in this study to those available in published literature is invalid as the computational elbow joint model developed in this study is completely different from the computational elbow joint models presented in literature thus far due to the inclusion of synovial fluid in between articular cartilages. Therefore, the articular cartilage stresses presented by this model will be significantly lower than those reported in literature due to the sheer presence of a fluid domain between articular cartilages.

Another potential reason for low articular cartilage stresses could be the omission of surrounding articular cartilages in the FSI simulations. Hindered by the lack of adequate computing power, for all the FSI simulations, only the moving articular cartilage bodies were included in the fluid domain while the stationary articular cartilage bodies were

excluded from the fluid domain. To account for this exclusion, wall boundary conditions were used to simulate the presence of the surrounding articular cartilages. However, such an approximation resulted in a larger than nominal gap between the articular cartilage geometries, which may have affected synovial fluid flow during joint motion, thereby impacting the forces exerted by synovial fluid on articular cartilages during joint motion. Thus, this could be a potential cause for low articular cartilage stresses reported in this model.

For the four joint motion categories—flexion, extension, pronation, and supination—the synovial fluid flow pattern exhibited different characteristics for the slower and faster joint motion conditions. For the slower joint motion conditions, synovial fluid flow was predominantly laminar, while the flow was turbulent for the faster joint motion conditions. However, for the four joint motion categories, von Mises stresses and maximum shear stresses were similar for both the slower and faster joint motion conditions. This may be due to the simplification of synovial fluid as a Newtonian fluid as opposed to a non-Newtonian, viscoelastic fluid. If synovial fluid were modeled as a shear-thinning, non-Newtonian fluid, differences in articular cartilage stresses may have been evident for the slower versus faster joint motion conditions.

6 CONCLUSIONS

During this study, a computational model of the left human elbow joint was developed to analyze the effects of synovial fluid on articular cartilage during joint motion. The elbow joint model comprised of anatomically accurate 3D bone geometries; articular cartilage geometries derived from the 3D bone geometries; ligaments that were defined as linear tension-compression springs; muscles that were embedded as non-linear stiffness in the flexion-extension and pronation-supination joints; and a fluid domain, filled with a homogenous, incompressible, Newtonian synovial fluid, that encompassed the elbow joint articulations. Eight FSI simulations were conducted in ANSYS 19.1 to simulate the interaction of synovial fluid with articular cartilage during flexion, extension, pronation, and supination of the elbow joint. Specifically, two FSI simulations with different joint loading conditions each were conducted for elbow flexion, extension, pronation, and supination. Important *in vivo* parameters such as elbow joint moment, ligament loads, articular cartilage stresses (von Mises and maximum shear), and synovial fluid flow patterns were determined through the FSI simulations. To the best of my knowledge, a computational model of the human elbow joint capable of simulating the interaction between synovial fluid and articular cartilage has not been developed before.

While this model demonstrates the effects of synovial fluid on articular cartilage during joint motion and provides the ability to determine crucial *in vivo* parameters, such as elbow joint moments, ligament loads, articular cartilage stresses, and synovial fluid flow patterns, there is more work to be done. Future work could include the viscoelastic, non-Newtonian nature of synovial fluid in the fluid domain model. Furthermore,

including anatomically accurate articular cartilage geometries and a synovial cavity, along with the non-linear modeling of ligaments and viscoelastic modeling of muscles, would increase the accuracy of the FSI simulations. Most importantly, subsequent iterations of this work must include all three articular cartilage geometries pertaining to the distal humerus, proximal radius, and proximal ulna in the FSI simulations to ensure that the effect of small gaps between articular cartilages on synovial fluid pressure is successfully captured. With high performance computing power i.e. 128 cores in parallel processing, these improvements can easily be incorporated into this elbow joint model.

REFERENCES

[1] T. M. Hunter, N. N. Boystov, X. Zhang, K. Schroeder, K. Michaud and A. B. Araujo, "Prevalence of rheumatoid arthritis in the United States adult population in healthcare claims databases, 2004–2014," *Rheumatology International,* vol. 37, no. 9, pp. 1551-1557, 2017.

[2] I. Rudan, S. Sidhu, A. Papana, S.-J. Meng, Y. Xin-Wei, W. Wang, R. M. Campbell-Page, A. R. Demaio, H. Nair, D. Sridhar, E. Theodoratou, B. Dowman, D. Adeloye, A. Majeed, J. Car, H. Campbell, W. Wang, K. Y. Chan and G. H. E. R. G. (. , "Prevalence of rheumatoid arthritis in low– and middle–income countries: A systematic review and analysis," *Journal of Global Health,* 2015.

[3] H. Zhou, N. D. Orvets, G. Merlin, J. Shaw, J. S. Dines, M. D. Price, J. K. Eichinger and X. Li, "Total Elbow Arthroplasty in the United States: Evaluation of Cost, Patient Demographics, and Complication Rates," *Orthopedic Reviews,* vol. 8, no. 1, pp. 43-46, 2016.

[4] A. Prkić, C. J. van Bergen, B. The and D. Eygendaal, "Total elbow arthroplasty is moving forward: Review on past, present and future," *World Journal of Orthopedics,* vol. 7, no. 1, pp. 44-49, 2016.

[5] J. P. Fisk and J. S. Wayne, "Development and Validation of a Computational Musculoskeletal Model of the Elbow and Forearm," *Annals of Biomedical Engineering,* vol. 37, no. 4, pp. 803-812, 2009.

[6] M. Rahman, M. S. Renani, A. Cil and A. P. Stylianou, "Musculoskeletal Model Development of the Elbow Joint with an Experimental Evaluation," *Bioengineering,* vol. 5, no. 2, p. 31, 2018.

[7] M. G. Carmichael and D. Liu, "Upper limb strength estimation of physically impaired persons using a musculoskeletal model: A sensitivity analysis," in *2015 37th Annual International Conference of the IEEE Engineering in Medicine and Biology Society (EMBC)*, Milan, 2015.

[8] R. V. Gonzalez, L. D. Abraham, R. E. Barr and T. S. Buchanan, "Muscle activity in rapid multi-ºree-of-freedom elbow movements: solutions from a musculoskeletal model," *Biological Cybernetics,* vol. 80, no. 5, pp. 357-367, 1999.

[9] S. W. O'Driscoll, K.-N. An, S. Korinek and B. F. Morrey, "Kinematics of semi-constrained total elbow arthroplasty," *The Journal of Bone and Joint Surgery,* vol. 74, no. 2, pp. 297-299, 1992.

[10] R. V. Gonzalez, "A Computational Musculoskeletal Model of the Human Elbow and Forearm in the Analysis of Ballistic Movements." Order No. 9519294, The University of Texas at Austin, Ann Arbor, 1994.

[11] J. R. Kusins, R. WIlling, G. J. King and L. M. Ferreira, "Development of a Computational Elbow Model with Experimental Validation of Kinematics and Muscle Forces," *Journal of Applied Biomechanics,* vol. 32, no. 4, pp. 407-414, 2016.

[12] M. A. Lemay and P. E. Crago, "A dynamic model for simulating movements of the elbow, forearm, and wrist," *Journal of Biomechanics,* vol. 29, no. 10, pp. 1319-1330, 1996.

[13] Y. Xu, J.-M. Zhan, Y.-H. Zheng, Y. Han, Z.-G. Zhang and C. Xi, "Computational synovial dynamics of a normal temporomandibular joint during jaw opening," *Journal of the Formosan Medical Association,* vol. 112, no. 6, pp. 346-351, 2013.

[14] S. Fornalski, R. Gupta and T. Q. Lee, "Anatomy and Biomechanics of the Elbow Joint," *Techniques in Hand and Upper Extremity Surgery,* vol. 7, no. 4, pp. 168-178, 2003.

[15] T. Barclay and S. Curreli, *Pronation/Supination*, July 3, 2018. Accessed on: June 26, 2019. [Online]. Available: https://www.innerbody.com/image/musc03.html#continued

[16] L. M. Ferreira, "Development of an Active Elbow Motion Simulator and Coordinate Systems to Evaluate Kinematics in Multiple Positions," Electronic Thesis and Dissertation Repository. 84, The University of Western Ontario, Ontario, 2011.

[17] Rice University, *8.2 Bones of the Upper Limb*, Accessed on: June 26, 2019. [Online]. Available: https://opentextbc.ca/anatomyandphysiology/chapter/8-2-bones-of-the-upper-limb/

[18] Rice University, *9.6 Anatomy of Selected Synovial Joints*, Accessed on: June 26, 2019. [Online]. Available: https://opentextbc.ca/anatomyandphysiology/chapter/9-6-anatomy-of-selected-synovial-joints/

[19] T. M. Tamer, "Hyaluronan and synovial joint: function, distribution and healing," *Interdisciplinary Toxicology,* vol. 6, no. 3, pp. 111-125, 2013.

[20] OrthopaedicsOne - The Orthopaedic Knowledge Network, *Synovial fluid*, March 22, 2012. Accessed on: June 26, 2019. [Online]. Available: https://www.orthopaedicsone.com/x/5wHbB

[21] M. Petrtyl, J. Lisal and J. Danesova, "Biomechanical Properties of Synovial Fluid in/Between Peripheral Zones of Articular Cartilage," in *Biomaterials - Physics and Chemistry,* Rosario Pignatello, IntechOpen, 2011.

[22] C. Barnett, "Measurement and Interpretation of Synovial Fluid Viscosities," *Annals of the Rheumatic Diseases,* vol. 17, no. 2, pp. 229-233, 1958.

[23] E. H. Jebens and M. E. Monk-Jones, "ON THE VISCOSITY AND pH OF SYNOVIAL FLUID AND THE pH OF BLOOD," *The Journal of Bone and Joint Surgery,* Vols. 41-B, no. 2, pp. 388-400, 1959.

[24] F. H. Netter, *Atlas of Human Anatomy*, 7th ed. Philadelphia: Elsevier, 2019. Accessed on: Jan. 12, 2019. [Online]. Available: https://studentconsult.inkling.com

[25] J. Hron, J. Málek, P. Pustějovská and K. R. Rajagopal, "On the Modeling of the Synovial Fluid," *Advances in Tribology,* vol. 2010, 2010.

[26] Zygote Media Group, "Solid (CAD) 3D Male Model," 2015. [Online]. Available: https://www.zygote.com/cad-models/collections-products/solid-3d-male-collection.

[27] S. Kim, M. E. Baratz and M. C. Miller, "Contact Stress Analysis of the Elbow Joint; Design of Radial Head Replacements," in *ORS 2011 Annual Meeting*, 2011.

[28] G. Giannicola, P. Spinello, M. Scacchi and S. Gumina, "Cartilage thickness of distal humerus and its relationships with bone dimensions: magnetic resonance imaging bilateral study in healthy elbows," *Journal of Shoulder and Elbow Surgery,* vol. 26, no. 5, pp. e128-e136, 2017.

[29] K. R. S. Holzbaur and W. M. Murray, "A Model of the Upper Extremity for Simulating Musculoskeletal Surgery and Analyzing Neuromuscular Control," *Annals of Biomedical Engineering,* vol. 33, no. 6, pp. 829-840, 2005.

[30] M. Van Den Broek and R. Van Riet, "Intra-articular capacity of the elbow joint," *Clinical Anatomy,* vol. 30, no. 6, pp. 795-798, 2017.

[31] L. Khezzar, A. C. Seibi and A. Goharzadeh, "Water Sloshing in Rectangular Tanks - An Experimental Investigation & Numerical Simulation," *International Journal of Engineering (IJE),* vol. 3, no. 2, pp. 174-184, 2009.

APPENDIX A

A.1 ANSYS FSI Simulation Benchmark

To evaluate the reliability of ANSYS for conducting FSI simulations, a review of published literature of ANSYS FSI simulations was conducted. Of specific interest to this thesis study is the paper, 'Water Sloshing in Rectangular Tanks - An Experimental Investigation and Numerical Simulation', presented by L. Khezzar et al. [31]. They focused on visualizing the flow pattern of water sloshing in rectangular tanks due to a sudden impact. They established that their numerical simulation results developed using ANSYS Fluent correlated well with their experimental results.

Specifically, they conducted four experiments with varying water levels in the tank subject to different initial impulse conditions. These experiments were also simulated in ANSYS Fluent. Primarily, flow visualization of water sloshing during various stages of tank motion was recorded using a video camera and then compared to the flow pattern generated by ANSYS Fluent. Khezzar et al. concluded that flow visualization and water levels from both experimental and numerical simulations correlated well except for a minor discrepancy at the instant immediately after the tank was subject to an impact. They attributed this minor discrepancy to the bouncing motion of the tank.

Based on this data, it was concluded that ANSYS Fluent is a reliable FSI simulation tool, and therefore, suitable for use in this thesis study.